UNIVERSIDAD DE GUANAJUATO

CAMPUS IRAPUATO-SALAMANCA
DIVISIÓN DE INGENIERÍAS

"Novel geometry in low-voltage circuit breakers"

Professional thesis work

To obtain the degree of:

Master's in Mechanical Engineering

A Thesis work by:

Miguel Serafín Núñez Aguayo

Advisors:

Abel Hernández Guerrero, Ph. D.

José Luis Luviano Ortiz, Dr.

SALAMANCA, GUANAJUATO. October 2022

Novel geometry in low-voltage circuit breakers

University of Guanajuato

Miguel Serafín Núñez Aguayo

October 19, 2022

Abstract

The simulation and analysis of the complex phenomenon of an electric arc propagation in low voltage chambers was investigated. The objective was to compare the effect of different geometries in the time required to achieve the extinction of the electric arc. The analysis is performed by electromagnetic field phenomena numerical simulations coupled with computational fluid dynamics and energy transfer. The aim is to propose a novel geometry that will improve the functioning of the electric arc propagation and extinction. The chamber consists of two electrodes of materials iron (cathode) and aluminium (anode), splitter plates of iron, and a fluid domain of air. The electric arc is modelled as a plasma column of 100 A of DC (Direct Current) flowing through air initially at 1×10^4 K, and atmospheric conditions for the fluid domain. Temperature-dependent properties are considered in the model. The simulations are performed by changing the configuration of geometric parameters in the proposed model and comparing the surface force along the plasma column. Once the geometries that exert a higher force were selected, a multiphysics transient simulation of the movement of the arc was performed and the extinction time was noted. A 13% of improvement in the extinction time was obtained in a geometry with lower displaced splitter plates occupying the same space, without the need to add any extra materials or extra costs to the original design.

Contents

List of Figures

List of Tables

Chapter 1

Introduction

The industrial revolution that began in the second half of the XVIII century brought a time of great growth in technology development and inventions. With this, societies were transformed into industrialized, urban settlements. This also brought a dependency in energy and material non-renewables resources. This had a big negative impact in the ecosystem that accelerated drastically over the last century. When the link between fossil fuel use and the increasing effects of climate change was accepted as a reality by most countries in the world, a collective effort in switching to clean energies, ban of damaging substances, and the promotion of social awareness was adopted by most countries.

The growth of the world's capacity to generate electricity from renewable technologies is on course to accelerate over the coming years. By 2026, global renewable electricity capacity is forecast to rise more than 60% from 2020 levels to over 4 800 GW – equivalent to the current total global power capacity of fossil fuels and nuclear combined [1]. Renewables are set to account for almost 95% of the increase in global power capacity through 2026, with solar photovoltaic (PV) energy providing more than half [1][2].

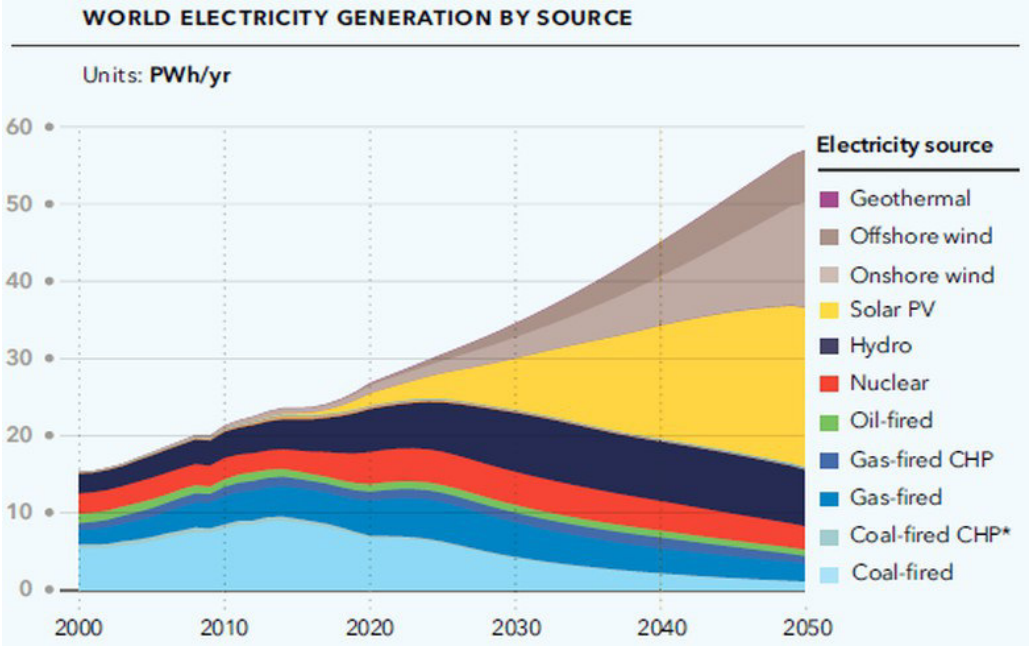

Figure 1.1: World electricity generation by source [2].

In the Figure 1.1, it can be observed that wind power and solar PV will drive the strong growth in renewable energy, and hydro will remain a key source.

It is important for the widespread implementation of these alternative technologies, that they become a competitive investment that is able to challenge the current fossil fuel technologies.
The levelized cost of electricity (LCOE), or levelized cost of energy, is a measure of the average net present cost of electricity generation for a generator over its lifetime. It is used for investment planning and to compare different methods of electricity generation on a consistent basis. The LCOE "represents the average revenue per unit of electricity generated that would be required to recover the costs of building and operating a generating plant during an assumed financial life and duty cycle" [5]. The Figure 1.2 shows an estimate of the LCOE for the most used energy generation technologies in the last decade.

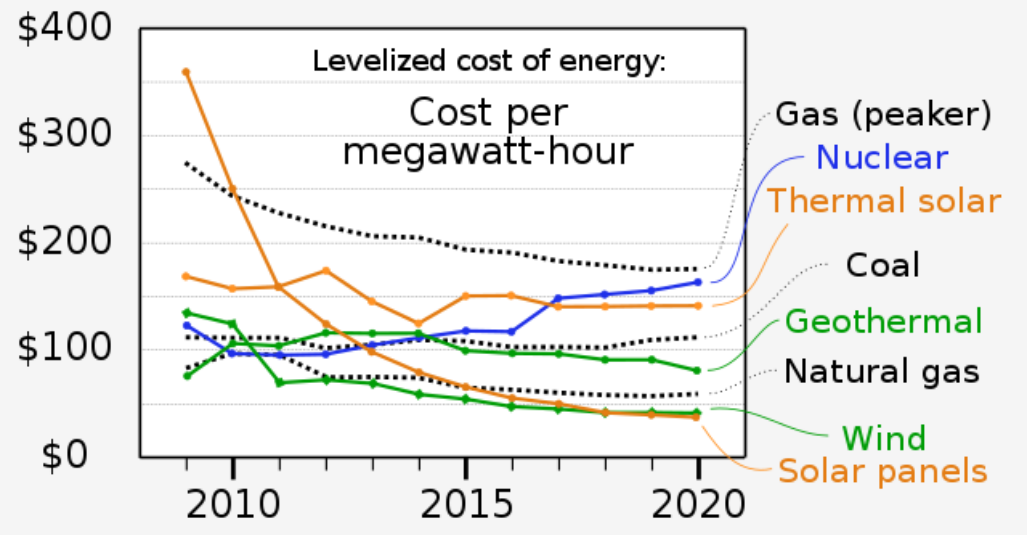

Figure 1.2: Levelized cost of energy [5].

Figure 1.2 shows that the LCOE of the energy generation technologies of solar PV and wind power is now the lowest when compared to other technologies. The viability of these energy sources was greatly improved over the last 10 years thanks to technological improvements, which increases the efficiency of these technologies, and the growth in market use, which lowers the costs.

More specifically, costs for technologies such as solar PV and wind power, are expected to go down by 18% and 16%, respectively, per the doubling of capacity. Renewables will improve cost performance at a much faster rate than oil and gas, benefitting from the 'learning curve' effect [2] [4].

The Figure 1.3 shows the percentage of renewable energy sources used as primary energy by country in the year 2021.

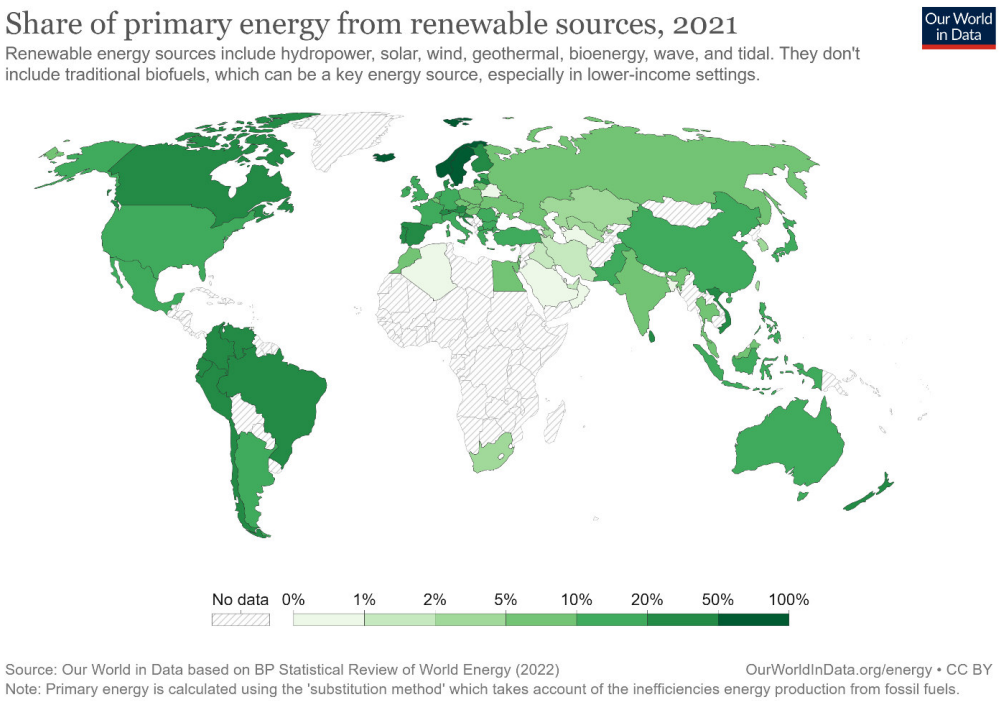

Figure 1.3: Share of primary energy from renewable sources (hydropower, solar, wind, geothermal, bioenergy, wave, and tidal), 2021 [6].

Approximately 30 countries are already producing 20% or more of their energy from renewable sources. This growth is increasing every year and Mexico is not an exception, with an 11% share of its energy production coming from renewable sources as of 2021 [6].
Mexico has a large and diverse renewable energy resource base. With the right policies, Mexico has the potential to attract large-scale investment in renewables that can help diversify its energy supply. Increased renewable energy use would also set Mexico on a pathway toward significantly reducing its greenhouse gas emissions. However, development has been limited so far [3].

1.1 Electricity distribution networks

In the XIX century, electrical networks were built to distribute DC electricity with the developments of Edison. However, the lack of standards and technologies for DC networks became the main reasons for the electrical distribution systems of alternating current (AC) to be the ones that dominated the market, thus becoming the standard for electricity distribution to individual consumers and the industry in the world.

The Figure 1.4 shows a diagram of a typical AC electric system network from the power station. This shows how electricity is generated in a power plant and distributed to the consumers.

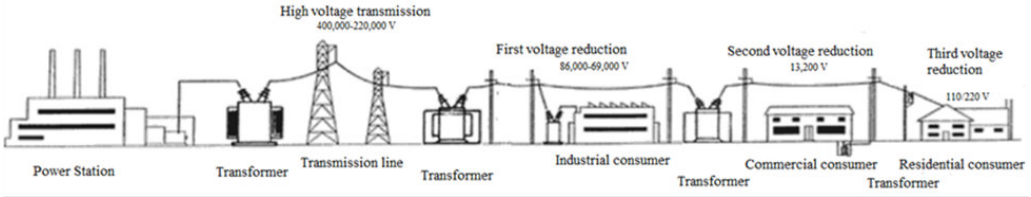

Figure 1.4: Electric system network, from generation to final user [7].

The AC supply model shown above is the standard in most countries, with small differences in voltage and frequency, ranging from 100-240 V, and 50 or 60 Hz. As an example, for residential consumers, the base AC voltage and frequency is 120 V and 60 Hz in Mexico, and 230 V and 50 Hz in Spain and other countries in Europe. Figure 1.5 shows a map with the nominal frequency and voltage for all countries.

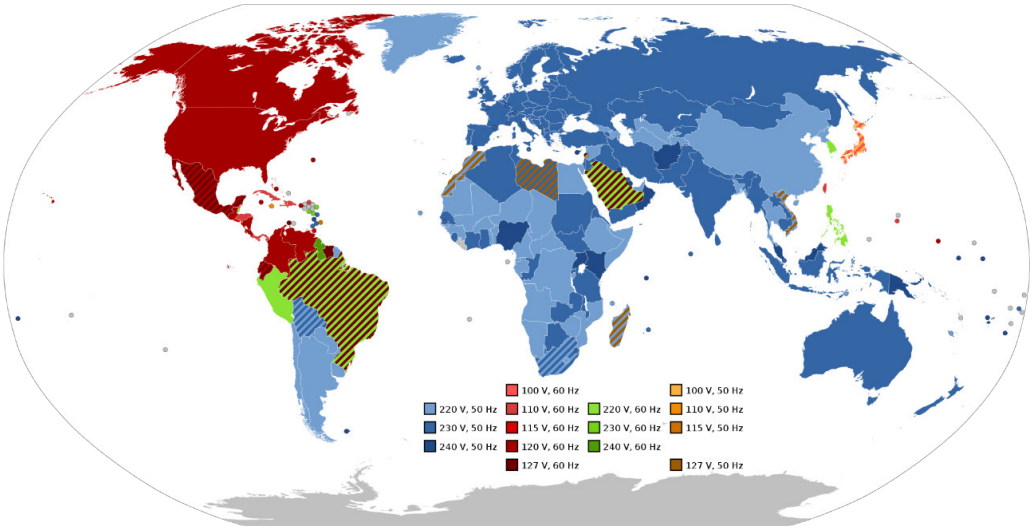

Figure 1.5: Nominal frequency and voltage by country [9].

In Mexico, the Federal Commission of Electricity (or CFE for its acronym in Spanish) is the state-owned electric utility of Mexico. It is the country's dominant electric company in charge of delivering energy to the general population and the industry. The Interconnected National System, or SIN for its acronym in Spanish, is divided into seven regions and three isolated systems in Baja California, Baja California Sur, and the Mullege region. In 2017, the SNI generated 309,777 GWh. The electricity production from 2007 to 2017 grew an average of 2.6 % yearly. Meanwhile, the final consumption increased up to 3.4 %.

The National Transmission Network, or RTN for its acronym in Spanish, is composed of 53 transmission regions. These transmission lines deliver a capacity of 400,000 to 220,000 V, and they only deliver electricity from the SIN power systems to the lines from the General Distribution Network (or RGD for its acronym in Spanish). Commonly, a sub-station adapts the voltage to a medium value, between 69,000 to 86,000 V. This system delivers electricity to the final consumer, from industrial to residential users. Commonly, it is divided into medium voltage and low voltage at 13,200 V. Transformers are used to adapt the voltage to the final user's needs. A house commonly uses 110 V, or 220 V in some cases.

1.2 DC to AC interconnection

Many of the current renewable energy technologies for electrical power generation produce direct current (DC) electricity. This is because some technologies, like solar PV panels, generate electricity in this form, or because the energy is generated irregularly (wind turbines) and needs to be stored in DC batteries. If the energy revolution to renewable sources is to be deemed successful, the implementation of direct energy networks or the adaptation of DC to AC inverter systems is unavoidable.

In Figure 1.6, a typical renewable energy system with a DC to AC power inverter is shown. This kind of installation is the recommended implementation of electrical generation from renewable sources in most cases. This also is the mandatory installation for private consumers in Mexico [8].

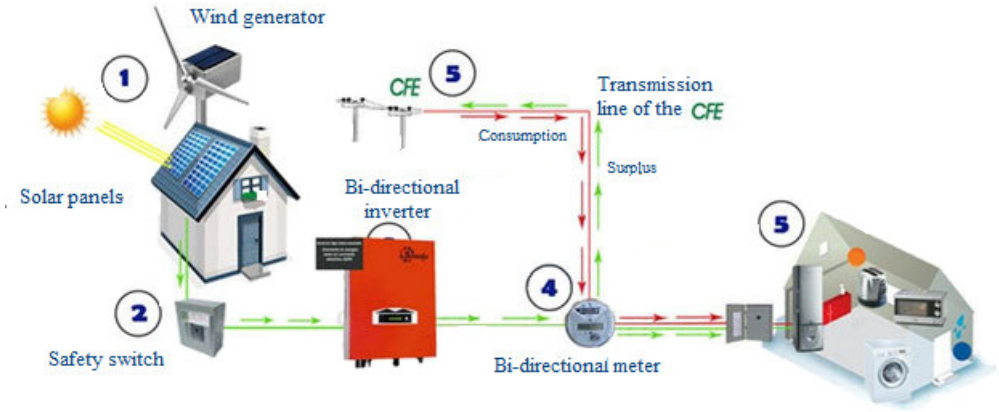

Figure 1.6: Main components of an electric power generation system with interconnection to the CFE's electrical network [8].

The system comprises various subsystems to generate, convert, and supply electricity to a house or building. Bidirectional systems provide power to the CFE's electrical network with the surplus generated by the renewable sources. Figure 1.6 illustrates a power generation system with interconnection to the CFE. This system can be implemented for solar panels and wind power. It

is divided into six subsystems:

1. Generation system: A photovoltaic panel converts solar radiation into electric current. Another option is a wind generator that uses the wind to generate electricity. It is possible to combine both solutions and create a hybrid system. Any solutions (solar or wind) generate direct current electricity (DC).

2. Safety switch: It cuts off the current flow from the generating source. It is an essential safety component since it protects against short circuits, over-currents, and residual loads. The low voltage circuit breaker (LVCB) protects the installation against failures by cutting and dissipating the energy without damaging the installation.

3. Inverter: It converts and adapts the energy from the energy source (commonly DC) into AC.

4. Directional meter: It measures the power generated by the user's system (wind, solar) and the power consumed from the CFE's electrical network. The system consumes CFE's power when having any power deficit, guaranteeing electricity to the user all time. If the user's system generates more energy than consumed, the user still has to pay the use of the CFE's electrical network.

5. Electrical network of the CFE: It supplies electric power at 120/220 V and 60 Hz for one and two poles, respectively. It supplies electricity to the house/building when a deficit is present by the generation system and receives the surplus from the house/building generation.

6. Electricity demand: The consumed electrical energy consumed by the house/building. Its structure and demand will depend on the devices that conform to it.

Power generation systems are limited to 0.5 MW for domestic use. Larger systems require a different approach for the interconnection with the CFE, but the 0.5 MW limit applies to most houses and small businesses. Previously, the balance of kWh in favor of the user could not be considered for selling to the CFE, so the user used to lose this surplus energy production.

In the case of bigger renewable energy power plants, such as solar PV fields, the interconnection to the commercial electricity distribution networks follows a similar pattern and installations. Figure 1.7 shows a diagram of the interconnection of a solar power plant to a commercial network.

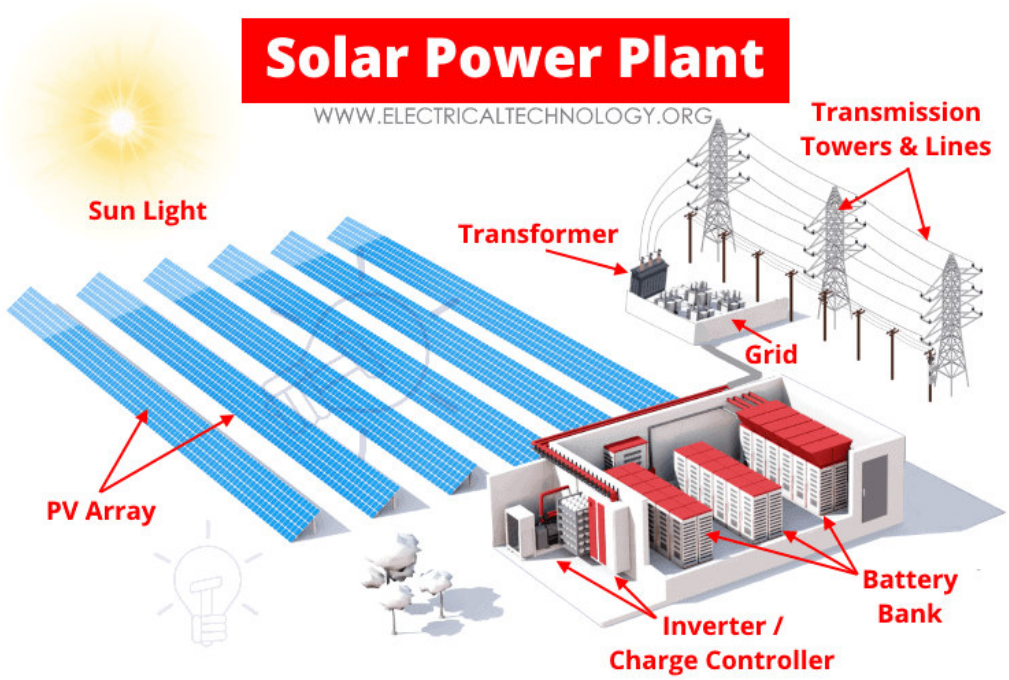

Figure 1.7: Layout plan of photovoltaic power plant [10].

As an example, the difference in magnitude of energy generated by a solar power plant to the one generated by a single user installation of solar panels is astounding. The largest solar PV power plant today is the Gonghe Photovoltaic Project, located in Qinghai, China, with a 3.1 GW power capacity [11]. Different solar PV power plants and power parks in the world

also produce energy in the range of hundreds of megawatts.

It is clear that large amounts of DC electricity are being generated by renewable sources and, given that the electricity distribution networks of the world still operate with AC as the basis [9], the interconnection of these new technologies to the supply chain of electricity is a vital point in the process.

1.3 DC circuit breakers

Protecting DC networks against short-circuits and safe disconnection is one of the most important challenges in the application of DC power systems. This is because safety devices in the case of a DC short-circuit are required in the process [12]. Figure 1.8 highlights the main safety devices required for a typical system of interconnection to an AC distribution network from a renewable source.

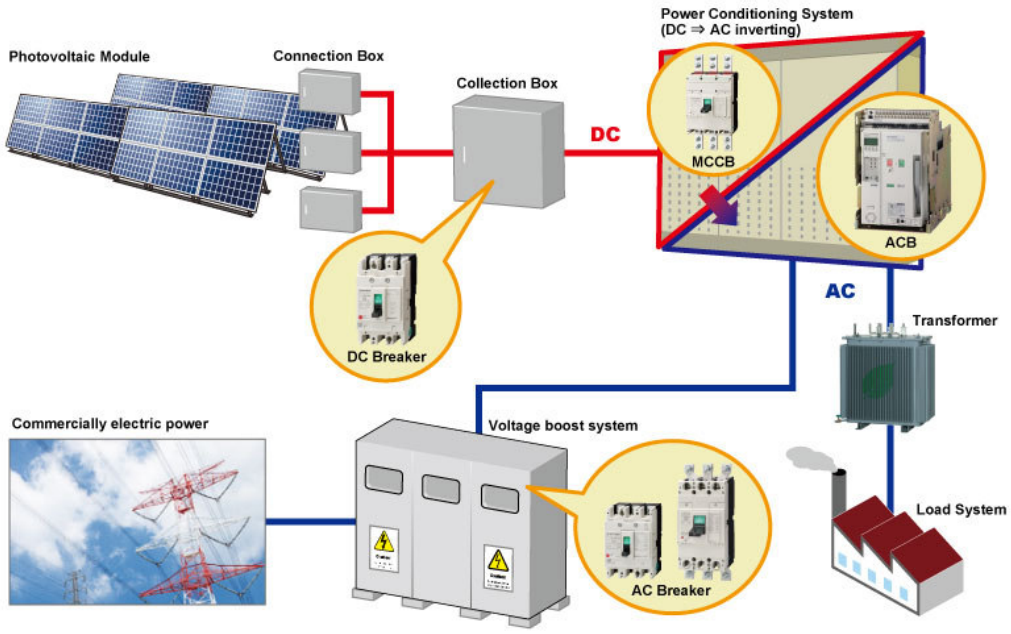

Figure 1.8: Installation example of industrial photovoltaic system [12].

The International Electrotechnical Commission (IEC) defines supply system low voltage as voltage in the range of 120 to 1500 V for DC systems. The device for the safe disconnection of electricity is called Circuit Breaker (CB). More specifically, if a CB is required to operate with DC electricity in the low voltage range, these disconnection devices are known as DC Low Voltage Circuit Breakers, DC LVCB, or simply LVCB.

An LVCB has a compact design. It is a single device that senses and opens/closes the circuit without external devices. Thermal or magnetic principles activate the LVCB. Figure 1.9 shows a Molded Case Circuit Breaker (MCCB) with its main components. There are many classifications for different kinds of circuit breakers, but the main components are the same in most cases. A more detailed view is explained in the next chapter.

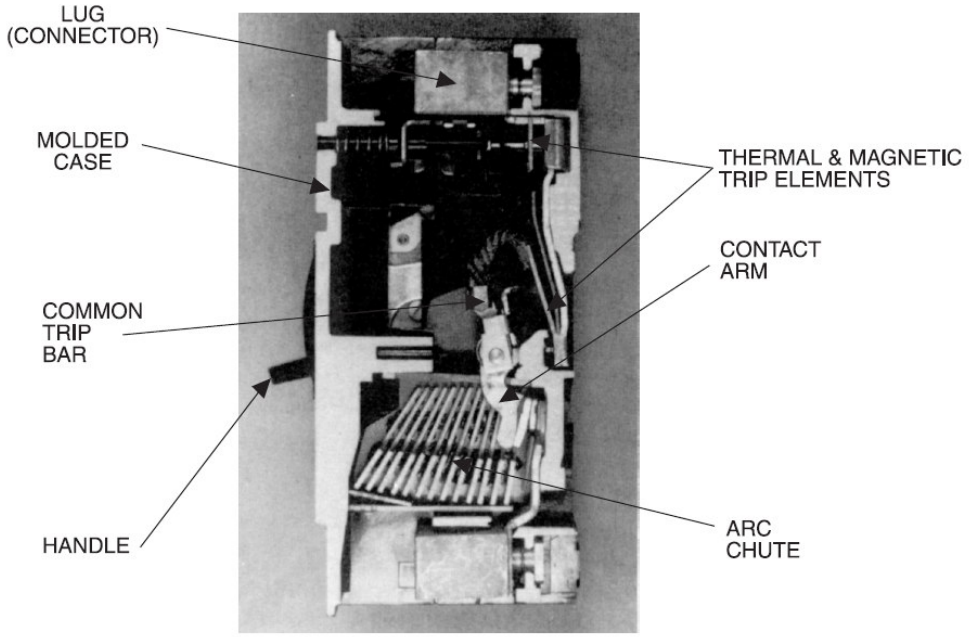

Figure 1.9: Thermal-magnetic trip MCCB [11].

A regular CB protects against short-circuit and overcurrent, offering a rapid trigger system for a fast response against short circuits.

The problem of disconnecting the DC electricity flow is more complex than in AC networks because the movement of electrons in DC is in a single direction and it never goes through a null value. These protection devices must extinguish a plasma column, which essentially is a high concentration of energy in a confined space, in the shortest time possible, and must dissipate the remaining energy in a way that protects the materials.

All CBs break the current using the same method, a high impedance/resistance method. An electric arc is formed in the middle of two contacts, increasing the resistance inside the circuit and dissipating the remaining energy after the arc is interrupted. It is necessary to break/dissipate the arc to stop the current flow [22]. The main techniques are based on the following ideas:

- Lengthening of the arc.
- Arc cooling.
- Split the arc into multiple parts.

Different fluids can be implemented inside the chamber to improve the arc dissipation, such as CO_2, SF_6, or air. The most common fluid for LVCB application is atmospheric air. More complex fluids, like mineral oil and compressed air, are used in medium and high voltage applications. Some CBs use a vacuum system, while others implement an insulator gas that suppresses the arc. Some DC CBs for high voltage applications (HVDC CB) use capacitors in parallel to make an artificial current zero point [22] .

LVCBs are designed to withstand various circuit faults without ever failing, offering a quick reconnection system without replacement parts. Since the current interruption in a CB is based on the formation and extinction of an electric arc, it is necessary to analyze this phenom, which can destroy the LVCB and the entire circuit if the arc is not quickly extinguished. The electric arc analysis is the main objective of this research, developing a model capable of replicating the arc behavior, and proposing a new geometry based in a commercial design.

1.4 Research in DC LVCBs

A good LVCB can be obtained based in an appropriated design and optimization of its geometry, materials, and operating conditions. This requires the analysis of the complex phenomena of arc propagation, which can involve experimental studies and numerical simulations. These studies are very expensive given the instrumentation costs for measuring the high levels of energy that occur in a very short span of time, and numerical simulation is limited given the complexity of the problem and the computing power available.

Research in electric DC arc propagation phenomena is being led by manufacturing companies, such as Siemens [13] and Schneider Electric [14] with 2D and 3D models for complex geometries that are the closest to reality. However, this research often includes proprietary code and not fully disclosed data. Simulations of an electric arc involve plasma fluid dynamics and electromagnetic interactions of the materials. This means that complex multi-physics numerical models must be constructed.

Initial studies in this field were carried out in 1996 by Karetta et al. [15], with an approach that considers the interaction of fluid dynamics, heat transfer, and electromagnetic phenomena, that can be solved by a numerical discretization procedure. This approach is known as Magnetohydrodynamics (MHD), and is the study of electrically conducting fluids, such as plasma and liquid metals. This modeling technique was further expanded to include the arc splitting process, due to the splitter plates in low voltage chambers, by Lindmayer et al. [9].

Iturregi et al. [4] studied the effects of the number of splitter plates in a simplified LVCB for a 3D magnetohydrodynamic model and validated the methodology with experimental data.

Lisnyak [16] extended the MHD model to include non-equilibrium effects near the electrodes due to plasma-elctride interaction in the electric distribution system of an aircraft, concluding that the results showed a good agreement with experimental measurements, and further improvements of the model were still possible.

Yang et al. [17][18] studied numerically how the arc-splitting process

was affected by eddy-current effects in the splitter and the electrodes. For this, they expanded the MHD model with the inclusion of the time-varying magnetic field term (necessary to produce the eddy currents effect in metals), and the ferromagnetic material's nonlinear permeability in the calculation. They concluded that the temperature rise produced by the effect of the eddy currents in the splitter plate is very small, which can be neglected. Including the eddy currents in the simulation makes the arc splitting process slower and the voltage peak values smaller. Also, if the number and volume of iron plates is small, the influence of the eddy currents on the arc splitting process can be neglected [18].

Singh et al. [19] simulated numerically the electric arc propagation phenomena by coupling Finite Element Analysis (FEA) and Computational Fluid Dynamics (CFD) to enhance the accuracy of the solution. They modeled the arc root effect as a thin shell layer having non-linear voltage resistance characteristics and included radiation effects using the Discrete Ordinates (DO) method. Integrating arc root physics in the analysis helped in understanding the effect of splitter plate configurations in LVCBs.

Arulanantha [20] proposed a different approach for the evaluation of DC circuit breakers. Using the concept of inverse problems, he predicted DC breaker performance at various short circuit currents. His work was based in experimental data and optimization to find the correct parameters for a mathematical model that would predict the performance of a LVCB when used at different short circuit conditions.

Lozano [21] realized a comparative study of different numerical simulation techniques for the complex phenomena of arc propagation in DC LVCBs. His work included a comparison of the main numerical characteristics and simplifications adopted by different works, such viscosity characteristics (laminar and turbulence models), radiation (no radiation effects, DO, radiative cooling, etc), arc roots (size, properties), magnetic field considerations (constant, time-varying), among other special consideration. His results suggest that the most efficient model in the simulation of arc propagation phenomena is achieved including the Net Emission Coefficient (NEC) model for radiation, $\kappa - \epsilon$ as the turbulence model, and the consideration of constant magnetic field as the pre-analysis. The NEC model with variable magnetic field should be reserved only for the best cases as the final solution given that it greatly

increases the computation costs and simulation time, and the enhancement in precision is small.

1.5 Scope of this work

The main objective of this work is to develop a model capable of replicating the arc behavior. The model will be used to analyze the thermal effects of the arc inside the LVCB. The analysis is focused on the LVCB during a circuit fault working with DC, by measuring the thermal effects in the extinction chamber during the arc expansion. The arc's ignition and extinction are not considered as there is no model capable of replicating with a reasonable cost (time/computation capacity).

With the above as the basis and the research discussed in the previous section, the numerical analysis for the arc propagation phenomena in this work will be carried out as an MHD model, coupling CFD and FEA numerical software, with the inclusion of arc root effects, nonlinear properties and constant magnetic field for the plasma, NEC model for radiation, and $\kappa - \epsilon$ as the turbulence model.

Once a model is developed, a geometry variation is compared against a commercial design. The new geometry is proposed by moving the splitter plates positioning inside the chamber, this with the objective of reducing the extinction time without increasing the manufacturing costs of the new geometry.

Chapter 2

The DC Low Voltage Circuit Breaker

A Low Voltage Circuit Breaker (LVCB) is an electro-mechanic device that works as a safety switch. An LVCB has four main characteristics [22].

- Allows the current to flow in the electrical network by closing the circuit.

- Operates normally at a nominal load for long periods of time without any interruption as long as the current does not exceed a limit imposed by design.

- Breaks the current by opening the electrical circuit from the electrical distribution network or the energy source. This action can be done by an external action (an operator) or after detecting a dangerous behavior in the electrical network such as an overcurrent or a short-circuit.

- Isolates the internal network from the electrical energy source. This protects the internal network, users, and equipment, preventing a potential failure from damaging and spreading to other circuits or network sections.

2.1 Types of LVCBs

LVCBs offer protection for voltages below 1,000 V in AC or 3,000 in DC. Voltages higher than 1,000 V need circuit breakers with a different kind of specifications. Conventional LVCBs are classified into three main groups: Low Voltage Power Circuit Breaker (LVPCB), Miniature Circuit Breaker (MCB), and Molded Case Circuit Breaker (MCCB). There are other classifications, such as Air Circuit Breakers (ACBs) and Insulated Case Circuit Breakers (ICCBs).

An ICCB is a circuit breaker enclosed in a case that does not allow exposure to live parts. It uses a glass-reinforced insulating material, such as fiberglass for dielectric strength. This description can also apply to MCCBs and MCBs. This depends on the standard, like the American National Standards Institute (ANSI) or the Underwriters Laboratories (UL) [23][35].

MCCBs and MCBs are assembled as an integral unit with an enclosure case. Likewise, an LVPCB is one of the older designs. It has a removable interrupter, making accessible the internal parts for maintenance and replacing parts after a fault. MCCBs are limited to 600 V and 6,000 A, while LVPCBs are used for applications with higher loads. MCBs are limited to 100 A, without the possibility to do any maintenance or repairs after a circuit fault, but are often used in domestic applications.
Each type of LVCB has different particularities, but its function in the circuit as a safety device is the same.

2.1.1 Molded Circuit Breaker

Molded Circuit Breakers (MCBs), also called Miniature Circuit Breakers (MCBs), are ideal for domestic, commercial, and small industrial installations, with a current load up to 100 A. MCBs are the smallest CBs found in the market, with an enclosed case to avoid contact with live parts [37].
MCB are usually mounted in racks or panels for easy access. Some MCBs only protect against residual currents, others are designed for quick action against faults, like short-circuits, while others protect against thermal effects due to overcurrent failures. The most common ones offer protection against short-circuits and long exposure to overcurrents at the same time [22][24].

Figure 2.1 shows a single-pole MCB. Multipole MBCs uses a very similar design, or multipole applications use a single-pole MCB protecting each pole.

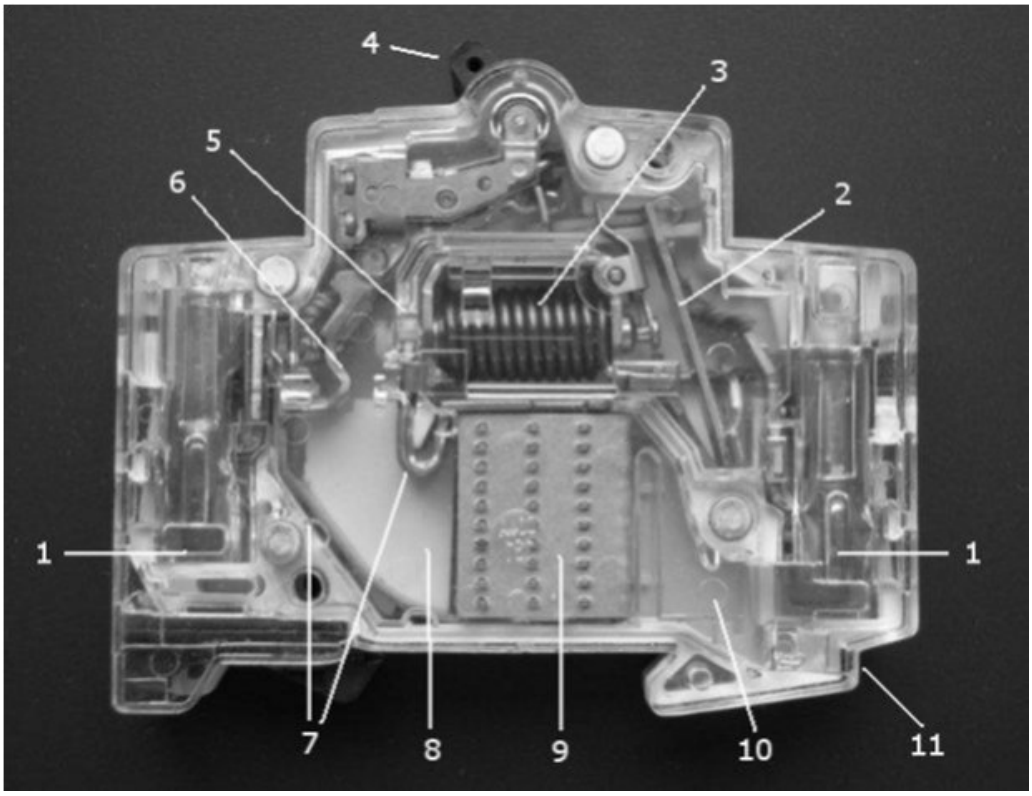

Figure 2.1: Modular Circuit Breaker (MCB) of ABB [22].

The MCB connects the circuit to the power source by the screwed terminals (1). This MCB has three ways to trigger the mechanics, a thermal switch (2), a solenoid (3) that works by electromagnetic principles, and a handle to be operated manually.
The current flows from the inlet screwed terminal to a bimetal (2). A bimetal is composed by two layers soldered at their ends. Each layer has a different thermal expansion coefficient. As current flows through these layers, Joule heating is produced. The difference in each layer's expansion coefficient produces a different elongation, producing a bend on the bimetal. The layer with the higher expansion coefficient will expand more, producing a curvature on it. As more current flows through the bimetal, it is heated

more and the curvature will increase. The curvature is used to push/pull a kinematic chain to trigger the aperture system of the MCB. This thermal arrangement is perfect for detecting overcurrent faults but not for short-circuits since the metals' thermal effects are slow and inertial.
The next safety mechanism to trigger the CB and interrupt the flow is the solenoid (3). The electrical operator, using solenoids, has a bistable latching mechanism to switch the circuit breaker ON and OFF. It is an electromagnetic device with a ferromagnetic plunger that can be retracted or extended. When charged, it can retract to trigger a mechanism that triggers the opening of the circuit. When uncharged, it can pop up to prevent the closing operation [38][39]. The plunger is counterbalanced by a spring to keep it in place. As the current flows through the solenoid coil, it produces magnetic fields that in contact with the ferromagnetic plunger induce Lorenz forces. When the Lorenz forces are strong enough to move the plunger and beat the spring that keeps it in place, a kinematic chain is activated, triggering the aperture system. This method avoids the inertial problems present in the bimetal method since magnetics fields are as quick as the speed of light. However, triggering the solenoid requires a considerable current load. A short-circuit produces a current load big enough to activate this system.
The third and last method to break the current is by manual operation, with a handle activated by the operator (4). This handle not only triggers the aperture system. After a fault, some components lose energy to activate the trigger system, discharging the spring or moving the components. When closing the handle, the internal mechanism like springs and actuator are charged/positioned, making the MCB ready to supply electrical energy and protect the circuit against electrical faults.
At this point, there are two ways for the current to flow. The regular way, where the fixed contact (5) and the mobile contact (6) are in physical contact, transferring the current to the outlet screwed terminal (1), supplying current to the circuit.
The other option consists of the trigger way, activated by one of the three methods mentioned above. The trigger system has the objective to break the current with a high impedance method. The fixed contact (5) and the mobile contact (6) are in charge of creating an electric arc. As the contacts are separated, a gap is formed between them. Figure 2.1 shows the contacts in the opening position. The current flow seeks to continue with its path, so an electric arc is formed in the gap. Since air is an excellent insulator

with very low conductivity, Joule heating increases the air temperature to the point of ionizing the air, forming an electric air. Once the electric arc is formed, it is free to move through the arc runners (7). Arc runners are two metallic conductors connected to the mobile and fixed contact. They are generally made of copper. Lorenz forces and the pressure gradients move the arc to the divergent channel (8). This channel separates the arc runners to the length of the arc, increasing the arc's resistance.

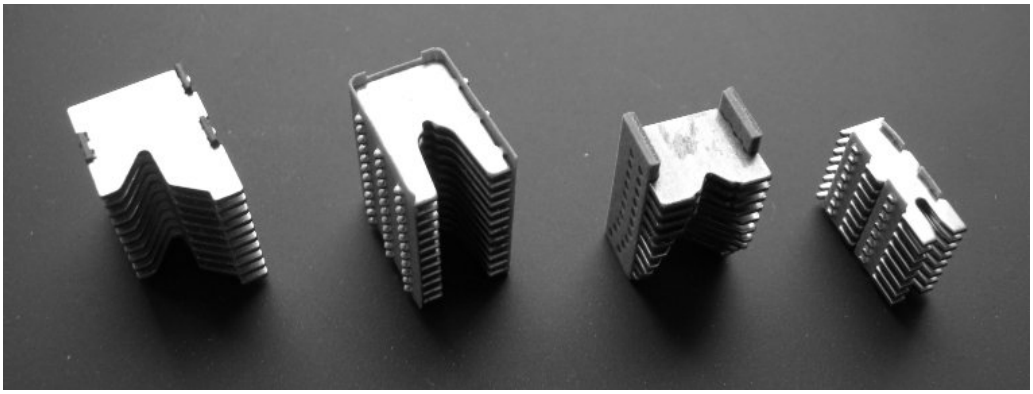

Figure 2.2: Samples of splitter plates [22].

De-ion chamber, extinction chamber, or arc chamber is where the arc ends is dissipated. A series of splitter plates compose it. Figure 2.2 shows some examples of splitter plates, which are commonly made of ferromagnetic materials. Some variations in the design are implemented to improve the arc movement, like U or V shape. The splitter plates' objective is to divide the arc into smaller arcs, making it easier to break it. The arc extinction process increases the temperature and pressure substantially inside the chamber. All the hot air is expelled through the extinction chamber's outlet (10) and the exhaust hole (11).

2.1.2 Molded Case Circuit Breaker

The Molded Case Circuit Breakers (MCCBs) are implemented for loads from 100 to 1,600 A. MCCBs are also fully contained in a plastic case, without the possibility to remove the inner parts or give maintenance [22][23][24].

Generally, MCCBs are bigger than MCBs due to the bigger load capacity. MCCBs work in a similar way to MCBs. The main difference is that the arc runners are pulled, generating the electric arc directly in the extinction chamber and lengthening the arc in the same process. Figure 2.3 shows the main components from an MCCB, where a shaft drives the mobile contact. The movement of the arc depends on the Lorenz forces produced by the current so, the greater the current load, the greater the speed of the moving contact [41].

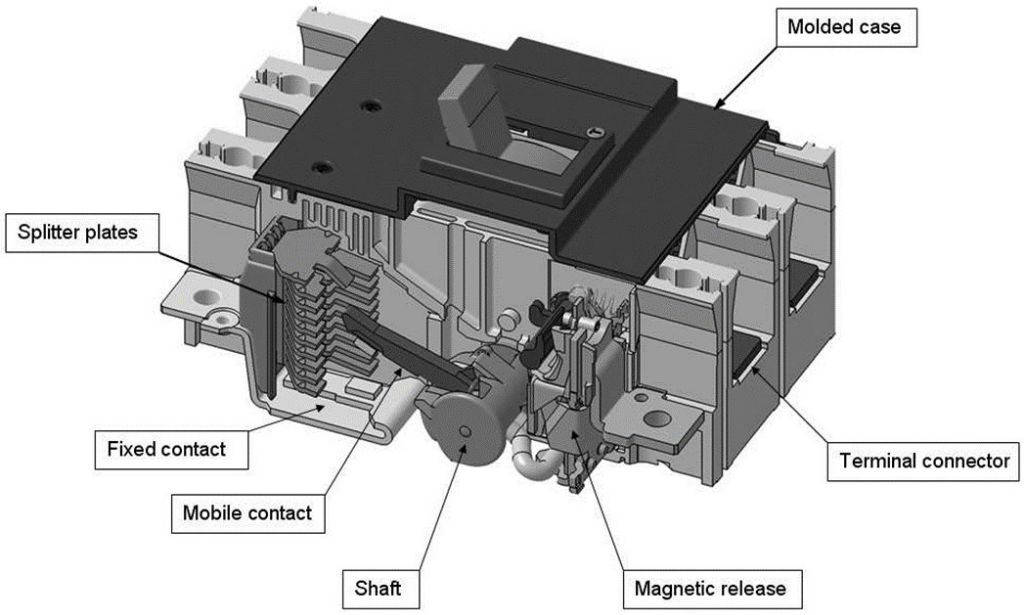

Figure 2.3: Principal parts of a Molded Case Circuit Breaker [22].

The shaft from Figure 2.4 operates a double system for the splitter plates. This method increases the resistivity, making a faster extinction of the arc but increasing the Joule heating and making the opening velocity the main advantage for this configuration.

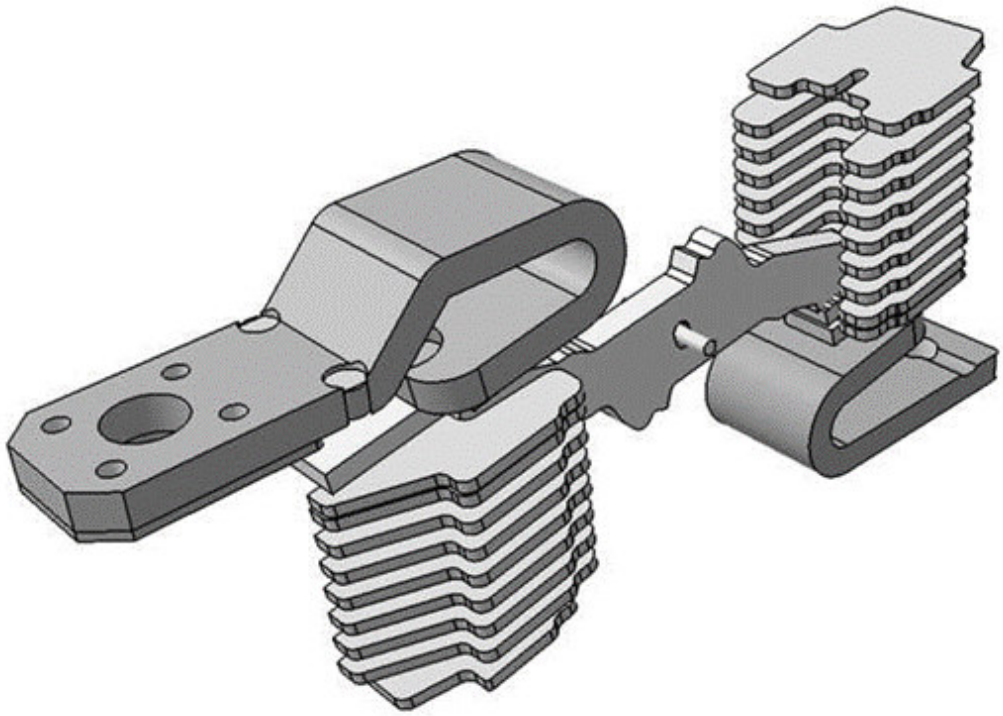

Figure 2.4: System of double interruption of an MCCB [22].

2.1.3 Other Types

The most common CB's operation was described, and just a very few variations can be found out of that. There are some differences in special LVCB models. Some limit the current on the circuit while others have a rapid trigger system. These systems are not covered in this work, but some variations in general applications are mentioned.

Low Voltage Power Circuit Breaker

Low Voltage Power Circuit Breaker (LVPCB) is the biggest type of LVCB, both in size and capacity. The system's complexity increases with respect to smaller models of LVCBs. It has a removable case for maintenance and part replacement.
In contrast to the MCCBs and MCBs, the trigger system is managed by

electronic devices, making it impossible to move the internal mechanism with only a handle. Figure 2.5 shows an LVPCB managed by push buttons to trigger the internal mechanism.

Figure 2.5: Low Voltage Power Circuit Breaker [22].

LVPCBs are implemented to work at high current loads and voltages. LVPCBs implement larger components to work up to 1,000 V and 2,000-6,000 A. Despite the load capacity and size, LVPCBs still implement air as the working fluid.

LVCB whit Induced Magnetic Fields

LVCB's have many variations despite performing the same function; sometimes, in order to minimize space, reduce materials or have a shorter extinction time. Some variations that have been implemented are magnetic arc chutes by adding an additional magnetic force to affect the arc movement.

It is important to mention that LVCBs with permanent magnets, or other external magnetic forces added to the system, are often dependent on a specific polarity in the connection of the CB. An incorrect connection could potentially cause the electric arc to move in the wrong direction entirely, away from the extinguishing chamber.

Some models implement an electromagnet [58] to produce a strong magnetic force. As shown in Figure 2.6, coils (60 and 78) are connected in series with the arc runners (66 and 82). The electromagnet (coil with a ferromagnetic core) uses energy from the arc by redirecting through the coil part of the current from the fault.

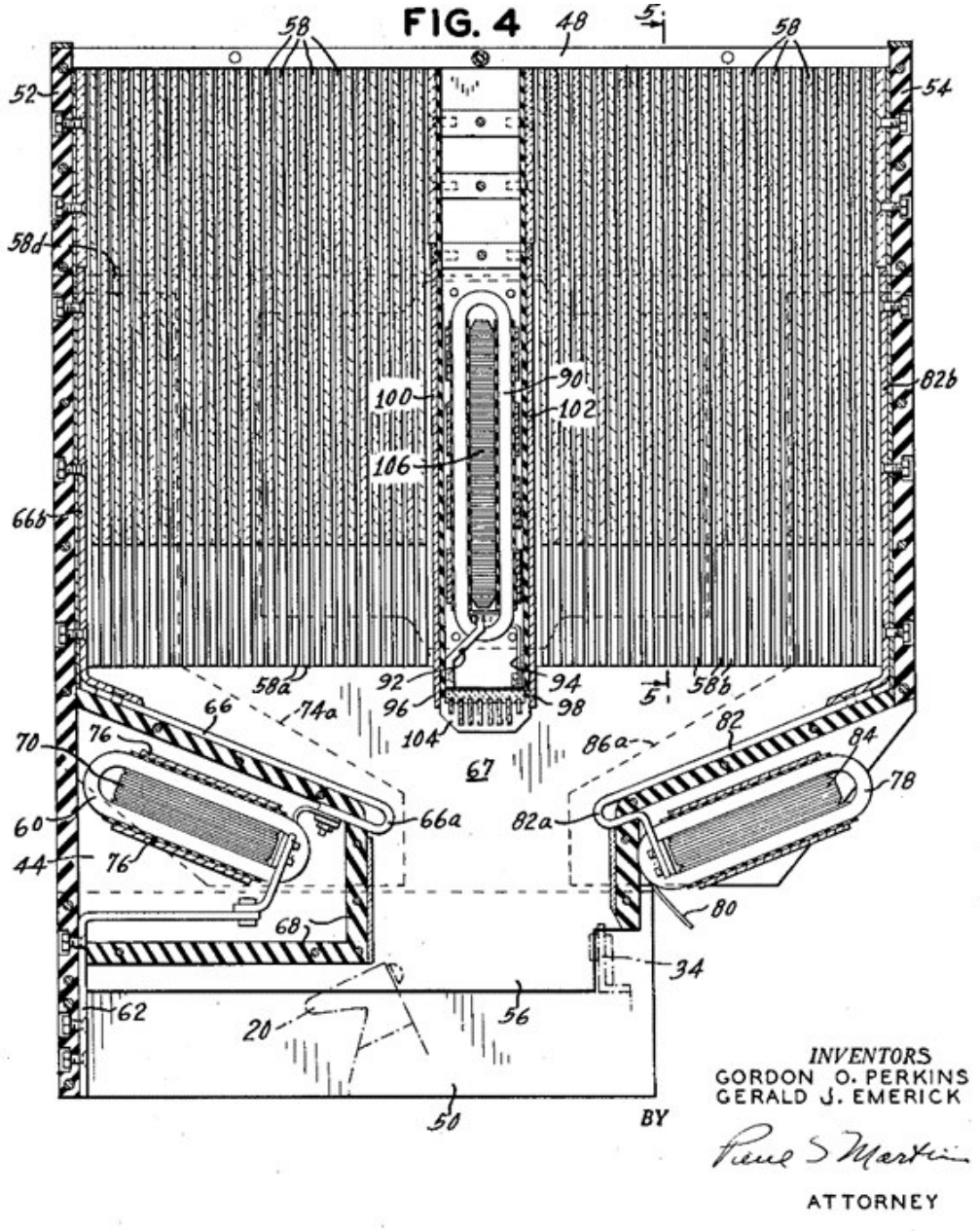

Figure 2.6: Circuit breaker with a magnetic arc chute implementing an electromagnet [58].

Another variation is to implement permanent magnets instead of electromagnets.

Permanent magnets are more subjected to shape variation compared to electromagnets. Permanent magnets do not require any current to operate; a heat isolator must be applied to protect the magnets since they can lose their magnetics properties when subjected to elevated temperatures [26][41]. Other variations are in the configuration of the splitter plates. There are many possibilities for modifications in the splitter plates of an extinguishing chamber, such as arrangement, materials, and splitter plate form.
Nahata [28] shows a combination of materials and geometrical variations in the plates. Figure 2.7 shows the arrangement for each splitter plate. The arrangement is composed of two components, a core (2) surrounded by two metal plates. The core is made of an ablative material. They all have a geometry that forms a magnetic field that promotes the arc's movement into the extinction chamber. Finally, all plates are joined by a resistive joint (3), a welding point that fixes both metal plates to facilitate conduction.
Due to its thermal properties, ablative materials can absorb the heat generated by the arc. This design aims to perform a faster arc's extinction, lower temperatures inside the CB, and avoid a re-ignition of the electric arc [28].

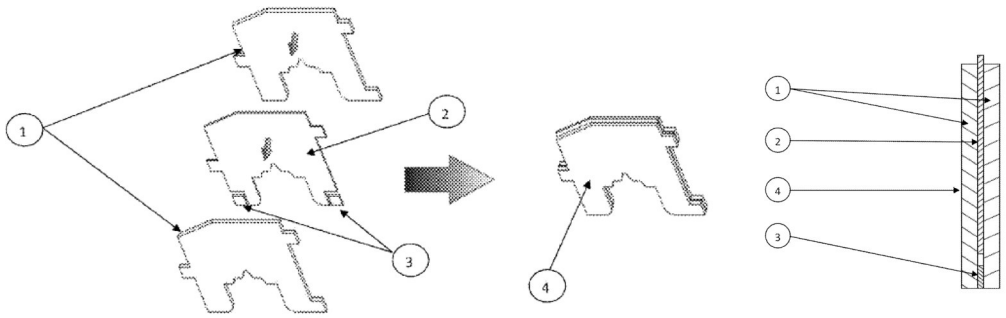

Figure 2.7: Arc chute arrangement for arc quenching in electrical switching device [28].

Another variation observed in various patents from several years ago is the absence of splitter plates. Some CBs use permanent magnets and electromagnets to extinguish the arc, while others create a splitter plate without metal. Each one offers a different advantage by changing the splitter plate system.

An example of this is the patent by Fasano [27], which implements a series of permanent magnets oriented to lengthen the arc. The system can be shown in Figure 2.8.

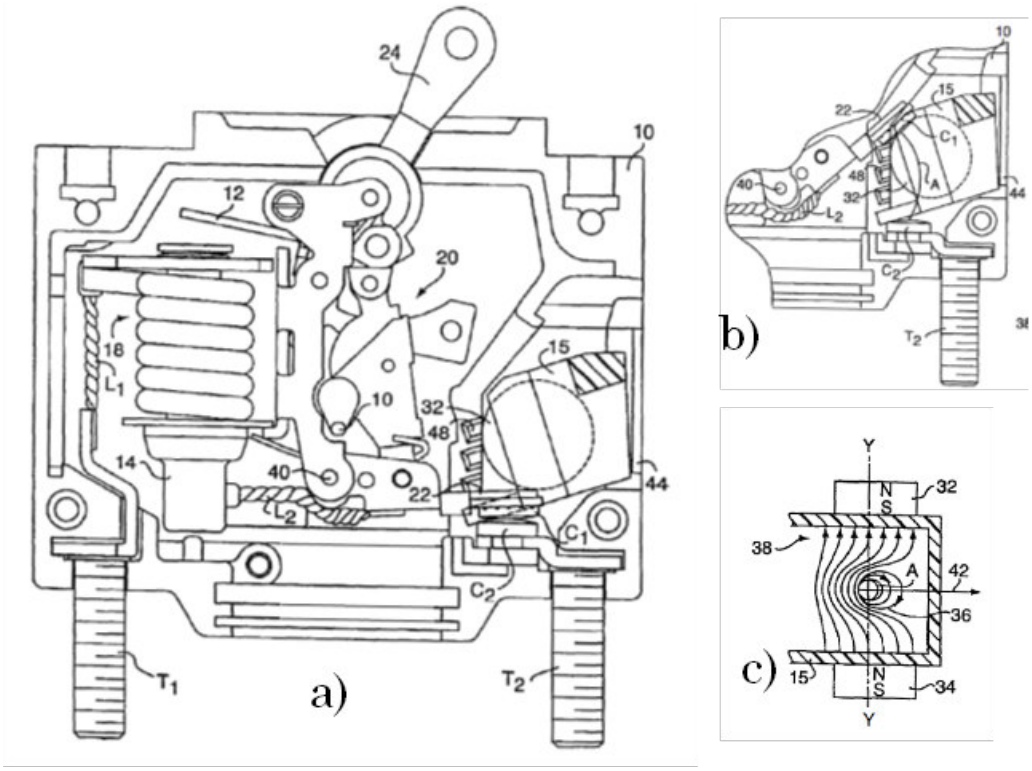

Figure 2.8: DC circuit breaker with magnets for reducing contact arcing [27].

- View a) shows the CB system. The CB has the splitter plate's slots (48) that are used to mount a magnet cradle (15) to support the magnets (32 and 34).

- View b) shows the system in an open position.

- View c) shows the extinction chamber, where the magnetic field from the arc (36) and the magnets (38) are positioned to lengthen and

redirect the arc in the direction of vector A (42).

LVCBs with permanent magnets can extinguish the electric arc quicker than designs with splitter plates only [27][42][43].
Another variation which avoids the use of metallic splitter plates is presented in the patent by Frind [29], where wall plates are used to extinguish the arc. It also incorporates electromagnets on both sides (26-31), as shown in Figure 2.9. Sidewalls replace the splitter plates with pins. These are sprayed with an isolating material composed mainly of amorphous fused silica.

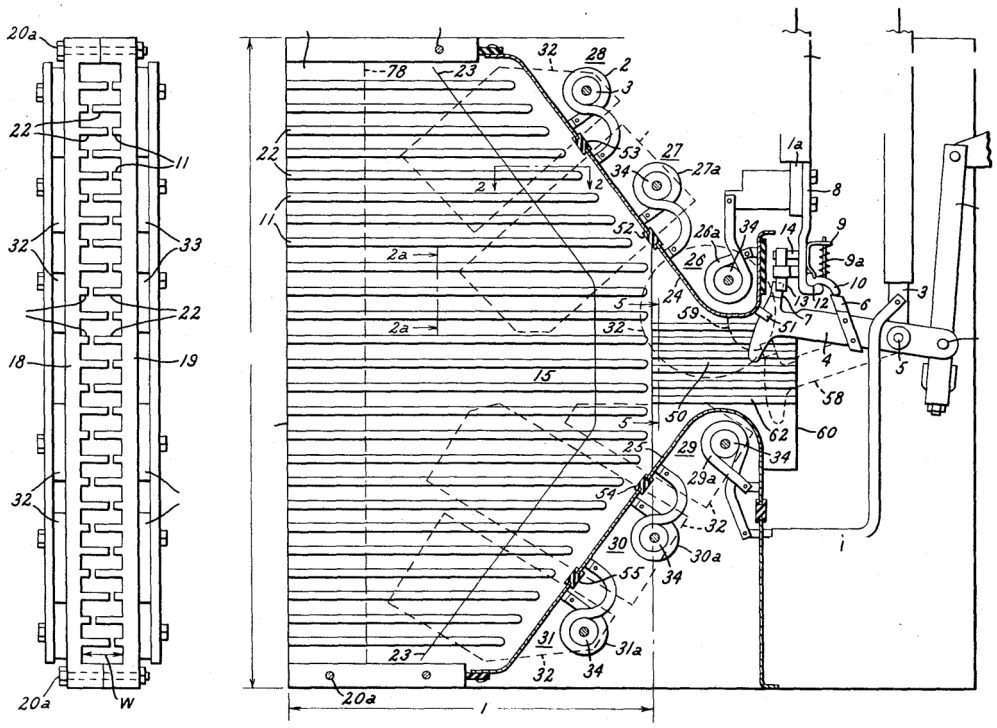

Figure 2.9: Lateral and frontal views of an arc chute for an electric circuit breaker [29].

Despite the differences of each of the models discussed in this chapter, dissipating an electric arc, by means of elongation, splitting, and increasing the impedance, is the main working principle of all of them. Achieving any improvement in the design of LVCBs must be analyzed before construction.

This objective of this work is proposing a new geometry based in simulation results that can shorten the span of time required to extinguish the electric arc, reducing wear of the materials and achieving a safer disconnection device for DC circuits.

Chapter 3

Methodology

The equations that describe the electric arc propagation phenomenon discussed in this work, are a combination of the Continuity and Navier-Stokes equations, together with the Heat Transport equation and the Maxwell's laws of electromagnetism. The model is enhanced with the inclusion of the Net Emission Coefficient (NEC) for the electric arc radiation, and arc root behavior modeled as a thin layer with voltage drop depending on the electrodes and splitter plate materials. Properties of air-plasma are considered as temperature-dependent, and the $\kappa - \epsilon$ turbulence model was considered for the fluid domain.

The specifics of the mathematical model used in this work will be discussed in the following sections.

3.1 Governing Equations

The Local Thermodynamic Equilibrium (LTE) approach, used in MHD theory, is applied to the arc propagation calculations, solving the system similar to a CFD analysis by solving the equations of Conservation of Mass, Momentum, and Energy, modeling the fluid flow, heat transfer, and, in some cases, chemical reactions, using discretized numerical models such as the Finite Volume Method (FVM). Maxwell's equations are used to solve the magnetic field: Gauss's Law, Gauss's Law for magnetism, Faraday's Law, and Ampere's Law. These equations can be solved using the Finite Element Method. The following sections contain a brief description of each equation [24] [49] [50]

[51] [52] [53] [54].

3.1.1 Fluid Dynamics

Conservation of Mass

$$\frac{\partial \rho}{\partial t} + \nabla \cdot \left(\rho \vec{V}\right) = 0 \tag{3.1}$$

Equation (3.1) shows the vectorial form of the Conservation of Mass Equation. For a transient analysis into a defined domain, density ρ can vary with time, so the change rate of density is defined in the first term of the equation. The second term describes the differences between the incoming and outgoing mass flow in the domain by using the fluid velocity $\vec{V}$ at inlets and outlets of the control volume.

Conservation of Momentum

Equation (3.2) is the vectorial form of the Conservation of Momentum for a transient analysis. Momentum is defined as the product of mass and velocity. Some considerations are taken into account to modify the equation and making it suitable for modeling the arc propagation phenomena in a LVCB.

$$\frac{\partial (\rho V)}{\partial t} + \left(\rho \vec{V} \cdot \nabla\right) \vec{V} = -\nabla P + \mu \left(\nabla^2\right) + \vec{J} \times \vec{B} \tag{3.2}$$

- The First-term represents the momentum change rate in the control volume

- The second term is the momentum difference on incoming and outcoming in the control volume.

- The third term is the pressure gradient.

- The fourth is the convective/diffusive term. Compressibility is neglected in most cases, while body forces take strength only in free burning arcs

[24].

- Finally, Lorenz forces are added as a source term, making a relation between electric and magnetic fields with the fluid dynamic.

The cross product of the current density $\vec{J}$ and the magnetic flux $\vec{B}$ generate an acceleration on the plasma fluid.

Conservation of Energy

$$\frac{\partial\left(\rho\ E_g\right)}{\partial t}\ +\ \ \nabla\cdot\left(\rho\ \vec{V}\ e\right)=\nabla\cdot\left(k\ \nabla T\right)+\ \nabla\cdot\left(\vec{V}\cdot\tau\right)+S_E \tag{3.3}$$

The Energy Transport Equation (3.3) comprises all the energy components inside the domain.

- The first term represents the energy variation over time.
- The second term is the variation of energy in the domain due to incoming and outcoming flows in the control volume.
- The third term represents the heat losses by conduction.
- The fourth term is viscous dissipation.
- The fifth term is a source term used to add energy interactions from other phenoms in the system, such as radiation.

It is important to remember that energy E_g is defined by tree main elements, enthalpy h, pressure work, and kinetic energy, as shown below.

$$E_g=H-\frac{P}{\rho}+\frac{V^2}{2} \tag{3.4}$$

Some considerations are taken to add the arc effects, like the Joule heating S_{Jh} and radiative heat losses S_R Due to the high temperatures in the arc. Considerations are also considered to simplify the problem, reduce the computing time, and help convergence in the CFD solution. These are pressure work, kinetic energy, and viscous heating are neglected. Equation (3.5) shows the resulting form of the Energy Transport equation with the last considerations.

$$\frac{\partial\left(p\ H\right)}{\partial t}\ +\ \ \nabla\cdot\left(\rho\ \vec{V}\ H\right)=\nabla\cdot\left(K\ \nabla T\right)+S_{Jh}-S_R \tag{3.5}$$

Joule heating is an irreversible process where heat is generated due to current passing through a conductor; in other words, it is the macroscopic effects of the electrons' movement through any conductor. This effect is governed by Equation (3.6), where $\vec{J}$ is the current density and $\vec{E}$ is the electric potential field.

$$S_{Jh}=\vec{J}\cdot\vec{E} \tag{3.6}$$

Radiative heat loses S_R due to the electric arc's high temperatures can be included in the model by different methods like DO or P1 models, but a significant simplification can be done by the Net Emission Coefficients (NEC), where heat losses on plasma are a function of radius and temperature $S_R\left(T,r\right)$. A deeper explanation is shown in the Arc Properties section.

Additionally, the electric potential equation is solved for the fluid dynamics. Equation (3.7) shows that the electric potential depends on the electrical conductivity σ multiplicated by the electric potential $\vec{E}$.

$$\nabla\cdot\left(\sigma_c\ \nabla\ \vec{E}\right)=0 \tag{3.7}$$

It is important to mention that the electric potential is only the gradient of the potential.

$$\vec{E}=\ -\nabla\phi.$$

At this point, the fluid dynamics are coupled with the electric and magnetic fields, including the Lorenz forces in the Momentum Equation (3.2). Radiative heat losses and Joule heating are included in the Energy Equation (3.5).

3.1.2 Maxwell's equations of electromagnetism

Law of Gauss

$$\nabla \cdot \vec{E} = \frac{q}{\epsilon_0} \tag{3.8}$$

Gauss's law, also known as Gauss's flux theorem, is shown in Equation (3.8). It is a law relating the distribution of electric charge to the resulting electric field, where the divergence on the electric field $\vec{E}$ in a control volume is proportional to the total charge q divided by the vacuum permeability ϵ_0.

Law of Gauss for Magnetism

$$\nabla \cdot \vec{B} = 0 \tag{3.9}$$

Equation (3.9) shows the Gauss law for a magnetic field $\vec{B}$. It states that the magnetic field $\vec{B}$ has divergence equal to zero, which means that it is a solenoidal vector field.
This implies that, in contrast to the electric field, it is impossible to store a magnetic flux $\vec{B}$ in any space. It is equivalent to the statement that magnetic monopoles do not exist.

Law of Faraday

$$\nabla \times \vec{E} = -\frac{\partial \vec{B}}{\partial t} \tag{3.10}$$

The Maxwell-Faraday equation, shown in Equation (3.10), is a basic law of electromagnetism predicting how a magnetic field will interact with an electric circuit to produce an electromotive force (emf); this phenomenon is known as electromagnetic induction.
$\vec{E}(\vec{r}, t)$ is the electric field and $\vec{B}(\vec{r}, t)$ is the magnetic field. These fields can generally be functions of position $\vec{r}$ and time t.

It states that a time-varying magnetic field always accompanies a spatially varying (also possibly time-varying), non-conservative electric field, and vice

versa.

AC motors, transformers, electromagnets, and any device that works with AC are based on this principle. It can also be used to explain the loops of electrical current induced within conductors known as Eddy currents.

Law of Ampere

$$\nabla \times \vec{H} = \vec{J} + \epsilon_0 \frac{\partial \vec{E}}{\partial t} \tag{3.11}$$

Equation (3.11) shows Ampere's law. Magnetic field strength $\vec{H}$ can be produced by the interaction of the current flux $\vec{J}$ and a variation in the electric potential over a domain.
The definition of $\vec{H}$ is shown in Equation (3.12)

$$\vec{H} = \vec{B}/\mu_0 - \vec{M}, \tag{3.12}$$

where μ_0 is the vacuum permeability, and $\vec{M}$ is the magnetization vector. In a vacuum, B and H are proportional to each other. Inside a material they are different. The H-field is measured in amperes per meter (A/m) in SI units.

3.2 Electric arc formation

An ideal circuit breaker must interrupt the electric current instantly. However, this behavior cannot be achieved in practice. When the contacts are separated, either by a fault or manual operation, the space between them is filled with air at high temperatures, becoming an ionized gas called an electric arc or plasma.

All LVCBs use air as the working fluid. Other fluids, such as Sulfur Hexafluoride (SF_6), carbon dioxide (CO_2) or argon (Ar), are used in medium and high voltage circuit breakers. The ionization of these fluids is a consequence of the high-energy state reached in extinguishing chambers, where some electrons are expelled out of the molecules, making the molecules an ion and changing its phase to plasma.

This plasma state can be achieved by an intense potential applied to the molecules or by heating a fluid to high temperatures. Both conditions are present in an extinguishing chamber, reaching temperatures up to 50,000 K [22]

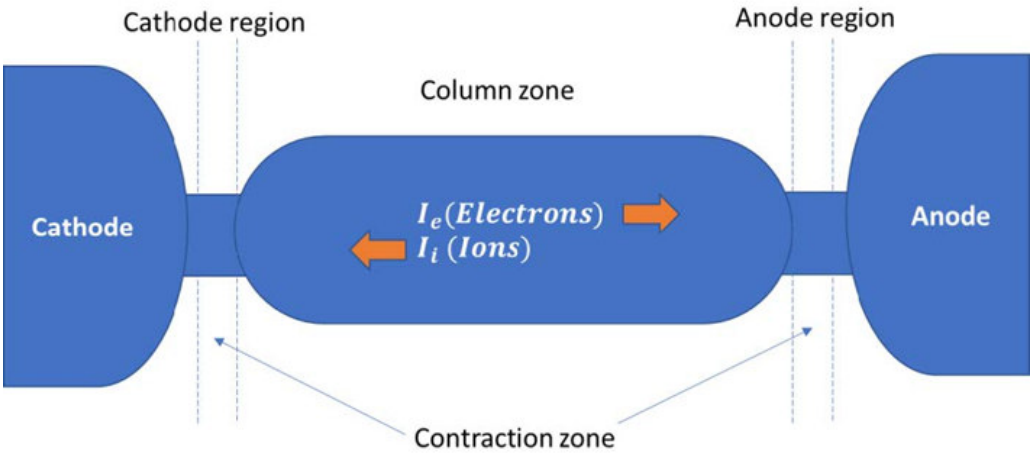

Figure 3.1: Electric arc structure [55].

The electric arc structure is divided into three parts; the arc column, and the two arc roots (anode and cathode regions) [55]. Each part contributes to the arc phenomenon and behaves differently.

3.3 Arc Behavior

Arc is formed due to the current flow through the contacts. As the contacts are separated, the current tends to continue its flow. Some air particles try to follow the current flow in an inertial effect.

Although the air is an insulator, it is heated by Joule heating increasing the magnitude of its electrical conductivity, which allows the conduction of all the current from the contacts in just a few air particles. This process is called electrical breakdown.
If the current is low, only a spark is originated without forming an arc. During

an electrical fault, the current increases up to many times the nominal value. This process heats and adds energy to the air particles to change it into the plasma state and generating an electric arc.

The plasma is composed of a mixture of electrons, ions, and neutral particles. The protons and neutrons are called heavy particles (H) due to the big difference in mass with respect to electrons (e).

Plasma is a state of matter whit high energy. Heavy particles start to emit photons once excited, looking to recover to a base state, giving a plasma its natural luminosity. A substance only can be considered as a plasma if the negative (electrons) and positive (ions) charges are equal, producing a balance and making an electrically neutral substance. This condition is called quasi-neutrality [50]. All the plasmas act as electrical conductors due to the free electrons.

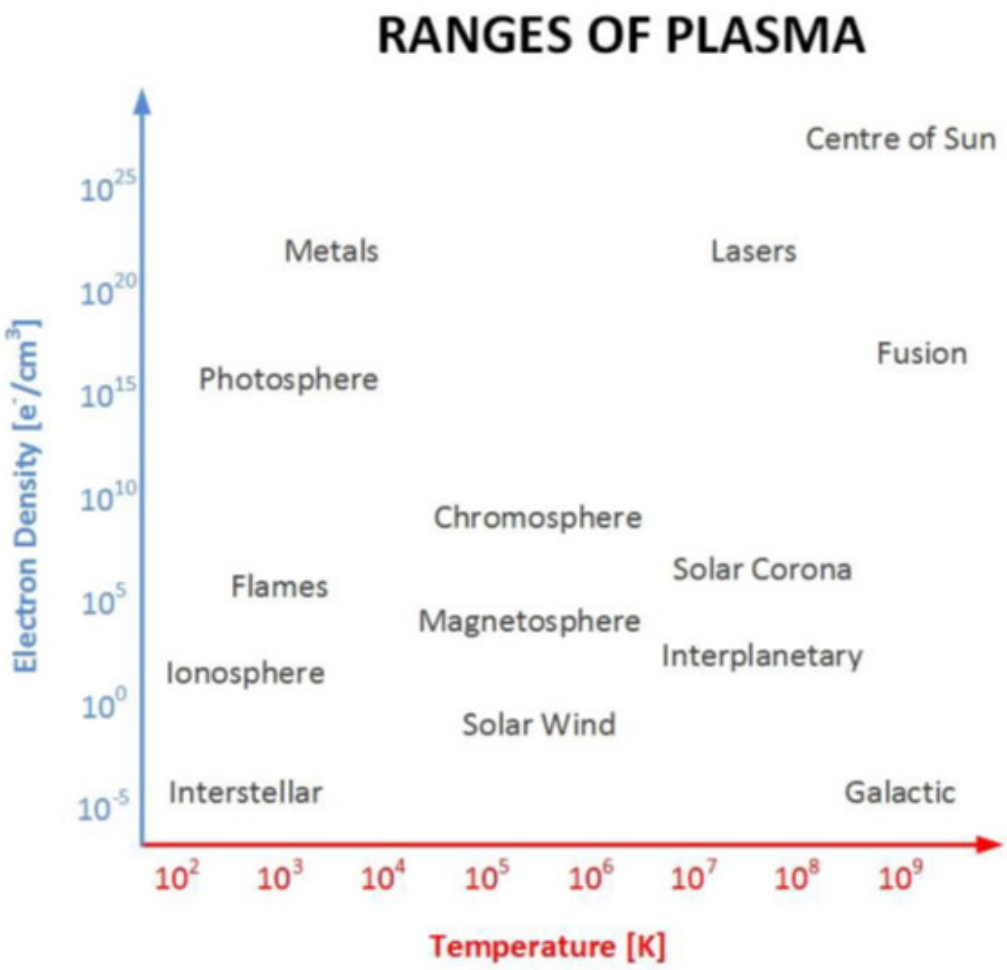

Figure 3.2: Plasma classification by electron density and temperature [50].

Plasma can be classified by temperature or density. Sometimes, the term electron temperature is used to describe plasmas, where $1eV$ equals 11,604 K. Figure 3.2 shows some examples of plasma classified on temperature and electron density [51]. Figure G.6 shows the plasma's characteristics in an electric arc, where temperature depends on the current flow [50]. As hotter a plasma gets, the denser it will be.

The high-intensity arcs are operated at currents greater than 50 A and 10 KPa of pressure. Below these conditions, and electric arc is considered as

a low-intensity arc.

Arcs can also be classified as thermal and non-thermal plasmas [50]. A non-equilibrium plasma or non-thermal plasma is when a strong derivation from the kinetic equilibrium is presented in the plasma. In other words, $T_e >> T_H$.

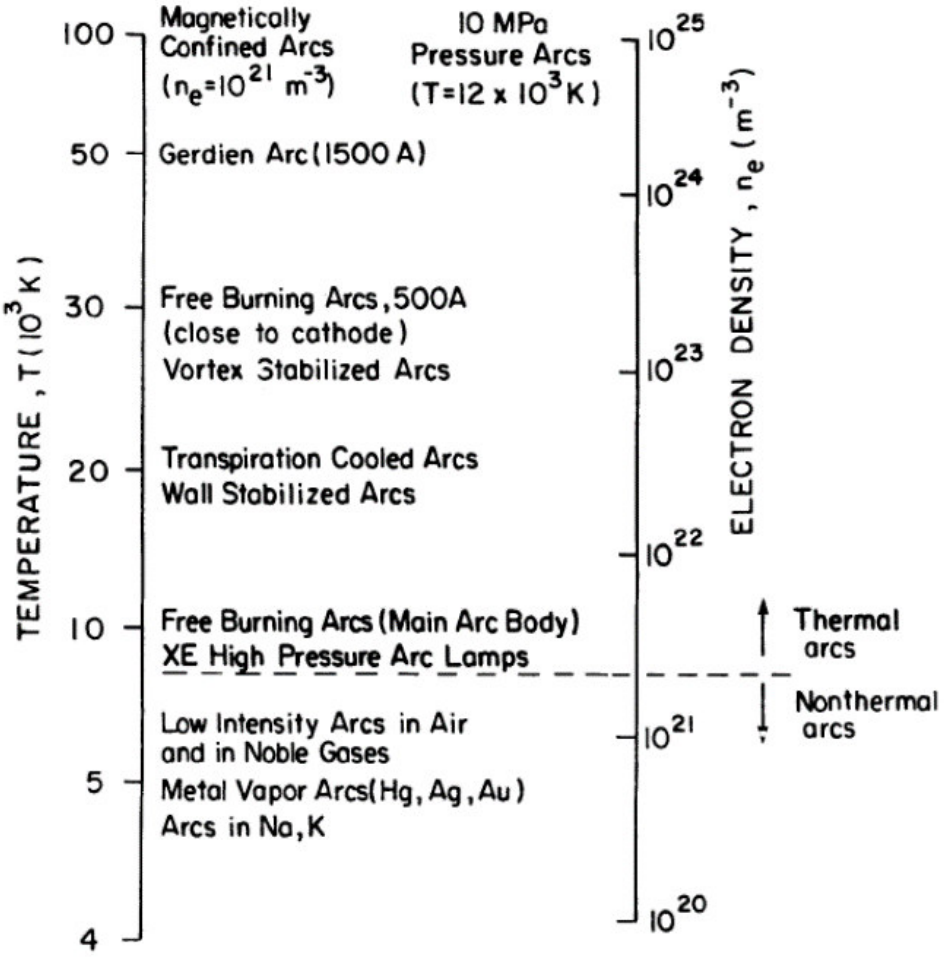

Figure 3.3: Temperatures and densities for some arc types [50].

3.4 Arc roots

Temperature is not the only thing that defines how the arc will behave. The plasma in contact with the metallic plates presents some particularities, which occur at the regions known as arc roots. This behavior is due to the plasma's micro-scale process and must be described as a non-equilibrium plasma.
A localized voltage drop results from this process. The driving mechanism behind it is not fully understood yet. The following is a brief summary of this complex process [22][49] [50][52].
Arc roots can be separated into many components, each one with a specific function in the arc. The zone where all of this occurs is the constriction zone. This zone contracts the arc column into a smaller space, getting bigger current densities up to 1,000 A/mm^2 while the arc column would be about 1-10 A/mm^2.

The first layer is the Constricted Plasma layer (CP). The CP layer produces high current densities, producing heat by the Joule effect. All the heat produced is mainly removed through radiation, conduction, convection, and species diffusion.

The next layer to the CP is the Thermal Perturbation/Heating (TP) layer. The TP layer is not governed by radiation heat transfer.

The next layer is the non-thermal equilibrium (NTE) layer. The NTE layer presents an electron temperature T_e different to the heavy particles' temperature T_H.

Following the NTE layer, the ionization layer (IL) is formed, this layer presents an electron density different from the regular plasma.

Usually, plasma properties are predicted by the Saha Equation (3.15). The NTE and IL layer do not follow the Saha prediction, something that is impossible to reproduce by the LTE/MHD approach.

Finally, a layer where plasma loses its neutral balance, depending on the contact, anode, or cathode; space is filled with electrons or ions, according to the current flow. This layer is named as charge-sheath layer or space-

charge sheath (SH). A powerful magnetic field characterizes the SH layer. This layer is responsible for the arc form, making its direction orthogonally to the electrode.

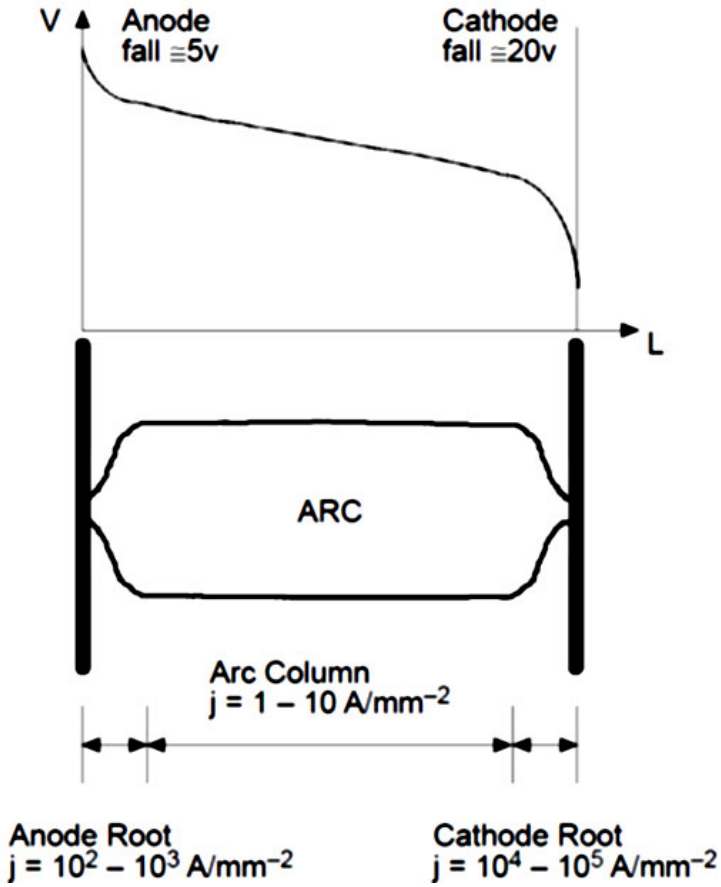

Figure 3.4: Roots of an electric arc.

Both roots do not have a symmetrical behavior due to many reasons, such as the mass difference between electrons and ions. Electrons present a considerable emission and re-absorption mechanism at the cathode surface, while ions move directly from anode to cathode. The differences are made by the SH layer and its strong magnetic field. The vast difference in the mass of ions and heavy particles also produces a different behavior in each plate. All these differences have a significant impact on the macroscopic approach.

As arc roots are constricted in a tiny place, the current density dramatically increases. The current density in the arc column is about 1-10 A/mm2. The movement of the electrons/ions at the arc roots creates a huge potential gradient in only about 0.1 mm. The speed variation between electrons and ions and the great recirculation of electrons generates a different potential in each contact. About 3-5 V for the anode (positive electrode) and 15-20 for the cathode (negative electrode) [56].

Although the magnetic field moves both roots, they have different behavior. The arc moves through the anode contact in a series of intermittent jumps. The cathode movement is continuous. This suggests that the cathode determines anode movement. This behavior is called arc commutation [56].

3.5 Magnetohydrodynamics

The arc implicates a series of complex processes, so various theoretical approaches have been developed to describe the plasma process [49][50][52]. Microscopic approaches describe each particle of the plasma; these approaches can explain the many processes in the arc-plasma propagation phenomena like the arc roots.

Microscopic studies analyze the movement of electrons, ions, and neutrons at the atomic size for each species in the plasma. Since air at 100 KPa and 273.15 K is composed mainly of nitrogen (N2) and oxygen (O2) in a ratio of 4:1, it is impractical to analyze each molecule by the microscopic approach. Other approaches describe the plasma as a macroscopic model, something more practical for engineering purposes.

When analyzing plasma properties, it is necessary to remember the essential components of the matter; the electron mass $m_e = 9.109 \times 10^{-31}$ kg is about 1836 times the proton mass $m_p = 1.672 \times 10^{-27}$ kg and the neutron mass $m_n = 1.675 \times 10^{-27}$ kg.

$$\frac{1}{2} m_p \ \bar{v}_p^2 = \frac{3}{2} k \ T_p \tag{3.13}$$

Temperature is defined by the average kinetic energy for each particle.

Equation (3.13) shows the relation between the mass of the particle m_p, the root-mean-square velocity of the particle $\bar{v}_p$, also called effective velocity, and the particle temperature T_p. For this relation it is assumed that particle movement is expressed by a Maxwell-Boltzmann distribution, resulting in Equation (3.14).

$$f(v) = \frac{4}{\sqrt{\pi}} \left(\frac{2\ k\ T_p}{m_p} \right)^{1/2} v^2 \exp\left(-\frac{m\ v^2}{2\ k\ T_p} \right) \tag{3.14}$$

Since air is composed of many types of molecules, the microscopic approach is problematic, impractical, and even impossible to solve for large analyses. Other approaches have been developed by adding some considerations. The multi-fluid approach separates each species (molecule) into charged particles and electrons, making a global balance for electrons, ions, and neutrons. Average values are taken for velocity and physical properties.

Unlike the particle model, the multi-fluid model assumes the continuum concept, making an average collision between components. This approach results in a simpler model but not convenient enough for engineering applications. Table 3.1 shows the average composition of atmospheric air to explain how many molecules are present in the air and the difficulty for microscopic and multifluid approaches.

Table 3.1: Composition of atmospheric air.

Species		Volume	
		ppmv	Percentage [%]
Nitrogen	N_2	780,840.00	78.084
Oxygen	O_2	209,460.00	20.946
Argon	Ar	9,340.00	0.934
Carbon dioxide	CO_2	383	0.0383
Neon	Ne	18.18	0.001818
Helium	He	5.24	0.000524
Methane	CH_4	1.75	0.000175
Krypton	Kr	1.14	0.000114
Hydrogen	H_2	0.55	0.000055
Dinitrogen oxide	N_2O	0.3	0.00003
Xenon	Xe	0.09	0.000009
Ozone	O_3	$\leq$ 0.07	$\leq$ 0.000007
Nitrogen dioxide	NO_2	0.02	0.000002
Iodine	I	0.01	0.000001
Carbon monoxide	CO	trace	
Ammonia	NH_3	trace	

Another approach is to use a two-fluid model, making a global value for electrons and another for heavy particles, including each species in the system as one.
Finally, the simpler plasma model is the one-fluid model, also called as Magnetohydrodynamic model (MHD). The main problem with this approach is that ignition, extinction, and arc roots effects cannot be solved. Despite its limitations, the MHD model produces good results, which has extended its use. The following chapter compiles the MHD model variants in the arc analysis.
MHD model makes some assumptions in the plasma particles, which most authors call it Local Thermodynamic Equilibrium (LTE) [24] [49] [50] [51] [52] [53]. There is a Complete Thermodynamics Equilibrium (CTE) approach, but it is not a practical model even at laboratory conditions.

LTE assumes that all fluid particles have enough time and contact to get a stable state. LTE makes some assumptions for the plasma particles, the most important are the following

- Thermal equilibrium: the electron temperature T_e is very similar (or equal) to the heavy particle temperature T_h.

$$T_e = T_h$$

- Ionization equilibrium: electron density n_e is equal to the predicted value by the Saha equation, with $n_e = n_{Saha}$.

$$\frac{n_e n_i}{n_n} = 2\frac{(2\pi m_e kT)^{2/3}}{h^3}\exp\left(-\frac{E1}{kT}\right) \tag{3.15}$$

- Quasi-neutrality: Plasma is neutral, so every electron in the plasma has a counterpart with an ion that makes the plasma a neutral substance, which is conductive due to the free electrons.

Since densities for each particle in the plasma are dependent on temperature, which is assumed to be very similar in all particles, a total density n is formed by adding up all the particles in the plasma. Remembering that ions and neutrons are called heavy particles, some relations are made with this arrangement: $n_i + n_n = n_h$.
Another consequence of assuming plasma neutrality, is that for each electron, there exists an ion in the plasma, so $n_e \approx n_i$.

Coupling all these assumptions transform the Saha Equation (3.15) to a simplified form shown in Equation (3.16). Where k is the Boltzmann constant, T is the temperature of the plasma, assuming to be equal or very similar for all the components, m_e is the electron mass, h is the Planck constant and E_i is the energy required to remove i electrons from a neutral atom.

$$\frac{n_e^2}{n_h - n_e} = 2\frac{(2\pi m_e kT)^{2/3}}{h^3}\exp\left(-\frac{E1}{kT}\right) \tag{3.16}$$

3.5.1 Plasma properties

In the MHD approach, plasma is considered as a single fluid, making the air-plasma properties a critical point in the analysis. Fortunately, many authors have obtained them experimentally. A good reference for most of the study cases is made by Murphy et al. [33], where air properties are calculated in the range of 300-30,000 K, conditions for the LTE approach.

Air is taken as a mixture of 78.09 % nitrogen, 20.94 % oxygen, 0.93 % carbon dioxide by volume. Other authors have calculated and corroborated these properties [50], [52], [57], showing the same behavior despite some small error difference.

For wide range of temperatures, the book *Thermodynamic Diagrams for High Temperature Plasmas of Air, Air-Carbon, Carbon-Hydrogen Mixtures, and Argon,* by Kroepelin et al [32], presents a good compilation of thermal properties common plasmas up to 100,000 K at different pressures.
Figure 3.5 shows the chemical composition of air at atmospheric pressure, where n is the total particle number. Although air is composed of many gases, as shown in Table 3.1, only nitrogen, oxygen, and argon are used in the plasma properties calculations, neglecting all other species.

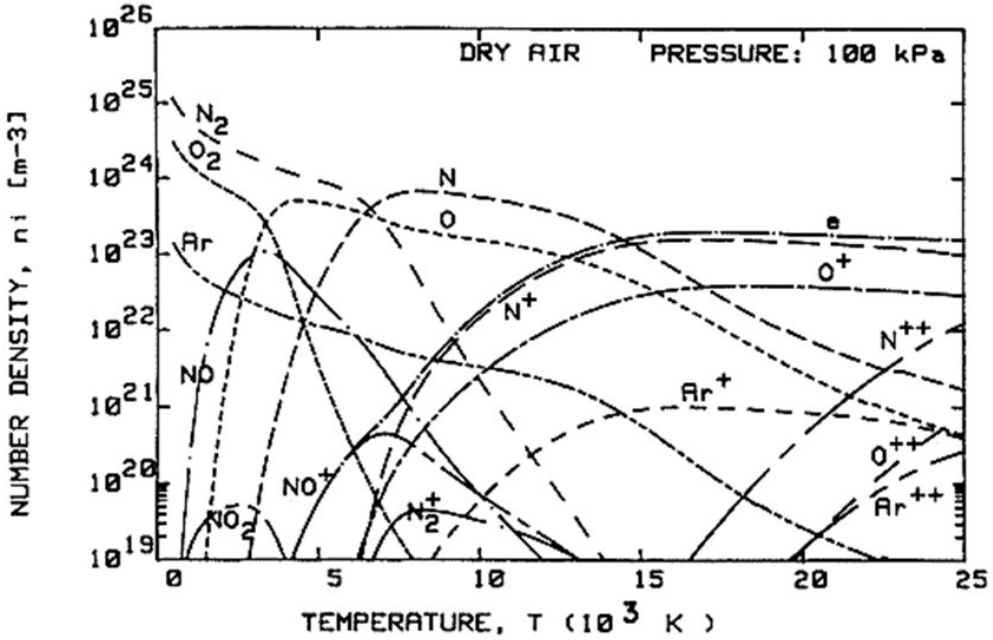

Figure 3.5: Chemical composition of air at atmospheric pressure [52]

If enough energy is applied to the air by joule heating, some chemical reactions take place between the nitrogen N^2 and oxygen O^2 molecules. A dissociation into neutral atoms N and O, 2000-3000 K for oxygen and around 4000-5000 K for nitrogen. Recombination takes place in the range of 2000 to 6000 K to form an electrical neutral nitrogen oxide NO. At 7000 K, almost all molecules become single molecules. Then at 9,000 K, a new ionization is present, forming ions for N^+, O^+ and negative ions e^+. For higher temperatures, around 20,000 K, a second ionization for nitrogen is present N^{++}.

All these associations/dissociation/ionizations result in the behavior observed in the plasma properties shown in the following sections.

Enthalpy

$$H - H^O = \int_0^T C_p\,(T)\,dT \tag{3.17}$$

Figure 3.6 shows the enthalpy for air plasma at atmospheric pressure. It is possible to calculate a specific heat C_p over the temperature differences from a reference state. Equation (3.17) shows this relation, where enthalpy H is defined by the enthalpy at reference state H^O with $T = 300$ K.

Peaks on the graph correspond to the dissociation in the plasma since each one requires a tremendous amount of energy.

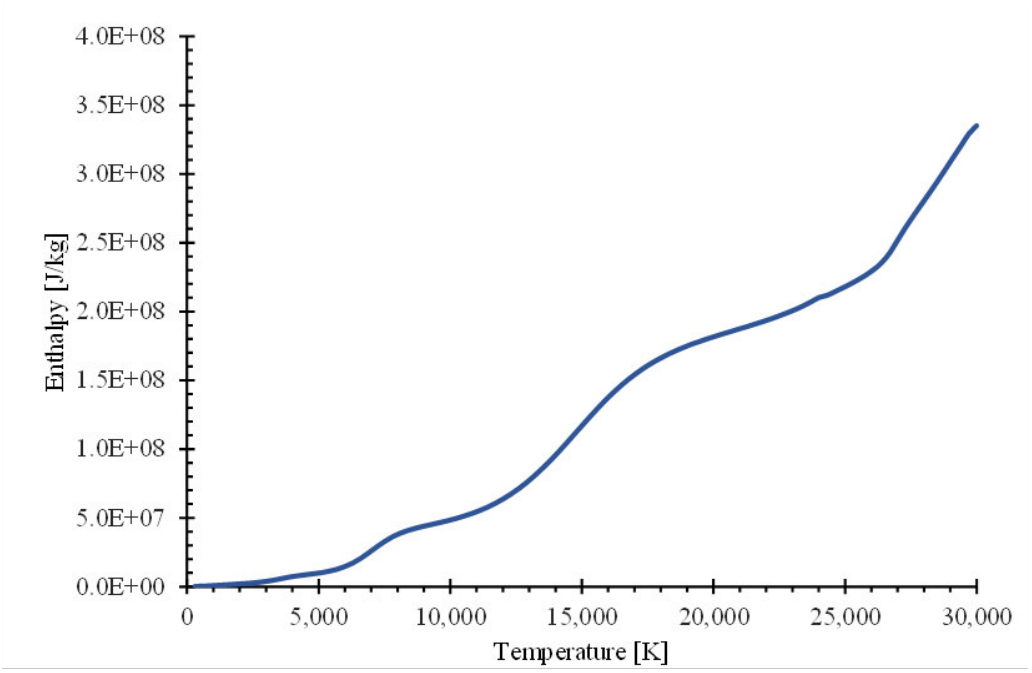

Figure 3.6: Enthalpy of air at atmospheric pressure [33].

Specific Heat, C_P

Figure 3.7 shows the specific heat for air plasma up to 30,000 K at atmospheric pressure. It shows peaks as temperature increases. These peaks correspond to the nitrogen and oxygen ionization.

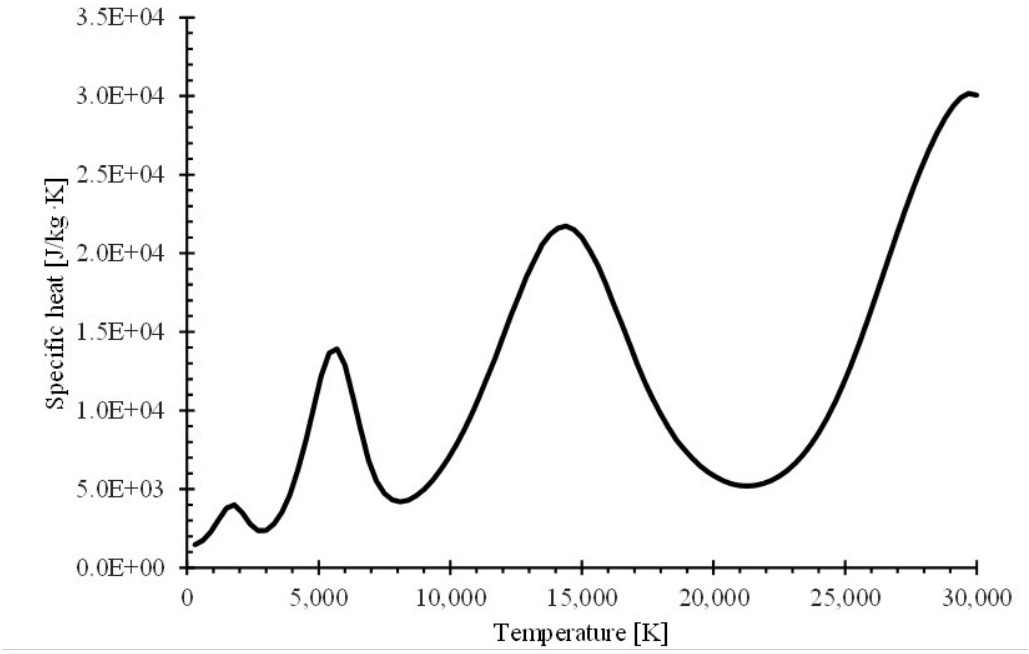

Figure 3.7: Specific heat capacity of air at atmospheric pressure [33].

Viscosity

Air-plasma viscosity is mainly determined by the heavy particles in the plasma (atoms, ions, and molecules), neglecting the electrons' influence. Viscosity increases as temperature increases due to the dissociation of oxygen from 3,000 to 5,000 K, together with the formation of NO^+ from 5,000 to 8,000 K.
Then, at around 10,000 K, viscosity tends to decrease due to the nitrogen dissociation, and it becomes almost constant at temperatures above 20,000 K. This behavior is shown in Figure 3.8.

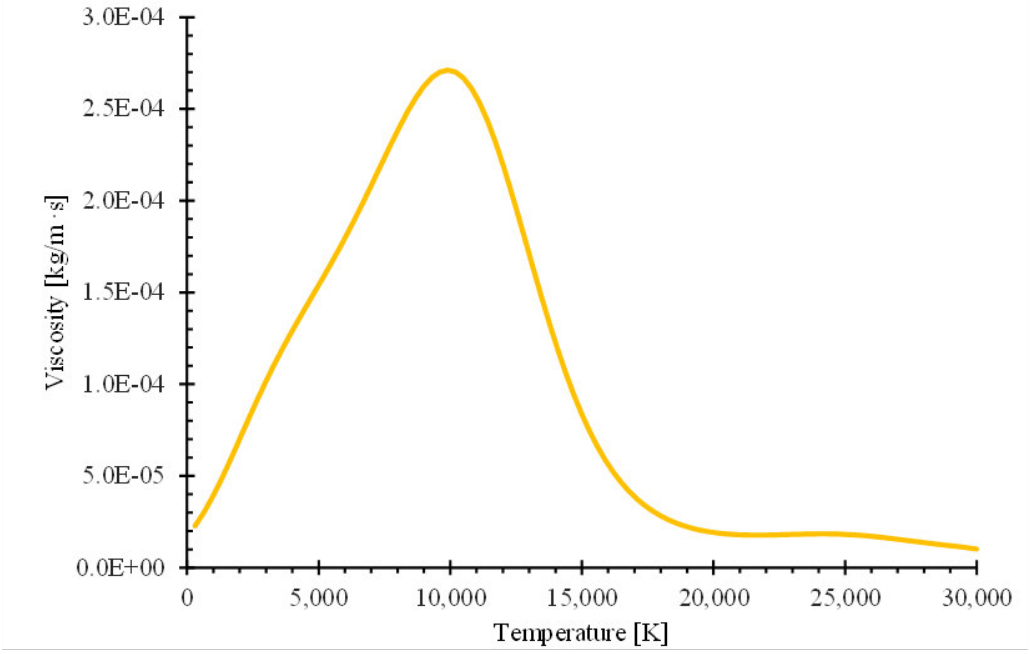

Figure 3.8: Viscosity of air at atmospheric pressure [33].

Electrical Conductivity

Electrons' mobility governs electrical conductivity since they can move easier than heavy particles. So, as the air gets ionized with temperature, the conductivity of the air can be neglected below 3,000-5,000 K. This can be seen in Figure 3.9, where electrical conductivity is almost null until it starts to increase the temperature above 5,000 K.
This effect coincides with the first ionization of air.

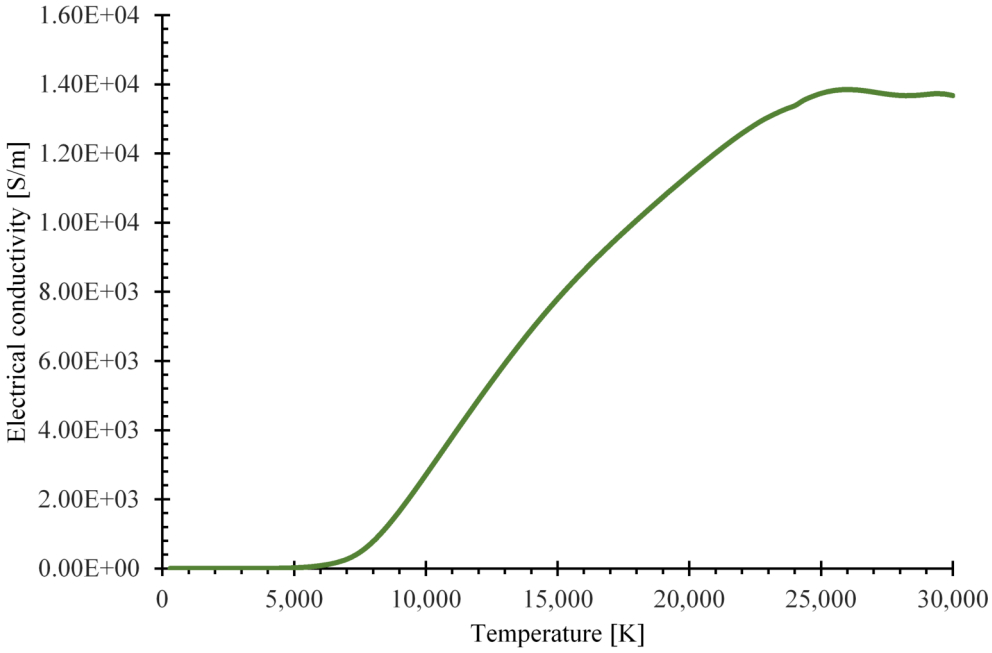

Figure 3.9: Electrical conductivity of air at atmospheric pressure [33].

Thermal Conductivity

All particles in the air determine thermal conductivity; each dissociation produces a high variation on the conductivity. The first peak is produced at around 3,500 K due to the oxygen dissociation, at the same time that NO.

The second peak starts above 7,000 K due to the nitrogen dissociation. The formation of nitrogen N^+ and oxygen O^+ ions in temperatures above 9,000 K produces the third peak. The second ionization of nitrogen N^{++} produces the final peak at 20,000 K. Thermal conductivity is shown in Figure 3.10, where the behavior is very similar to that of the specific heat capacity.

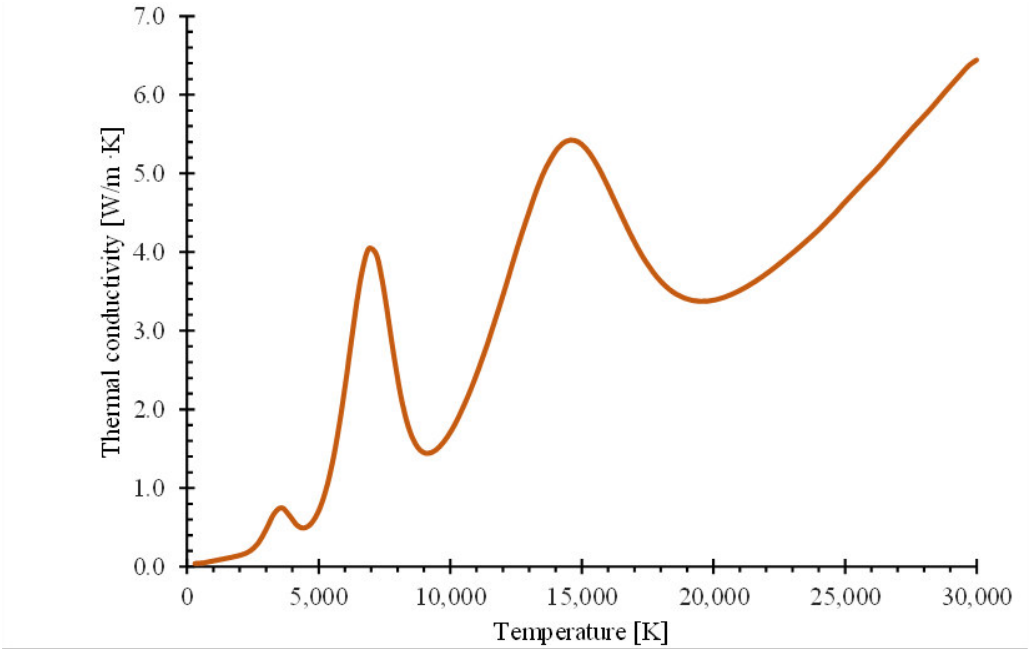

Figure 3.10: Thermal conductivity of air at atmospheric pressure [33].

Radiation

Radiation in the air plasma can be modeled using the Net Emission Coefficient (NEC). The NEC model corresponds to the difference between the radiation emitted at an isothermal sphere and the radiation emitted by the other points in the sphere [46][47].

Figure 3.11 shows the Net emission coefficient of air at 1 bar, considering an optically thin plasma with a sphere of 0 mm. According to Billoux et al. [46], NEC is a good approximation to characterize the radiation losses in hot regions.

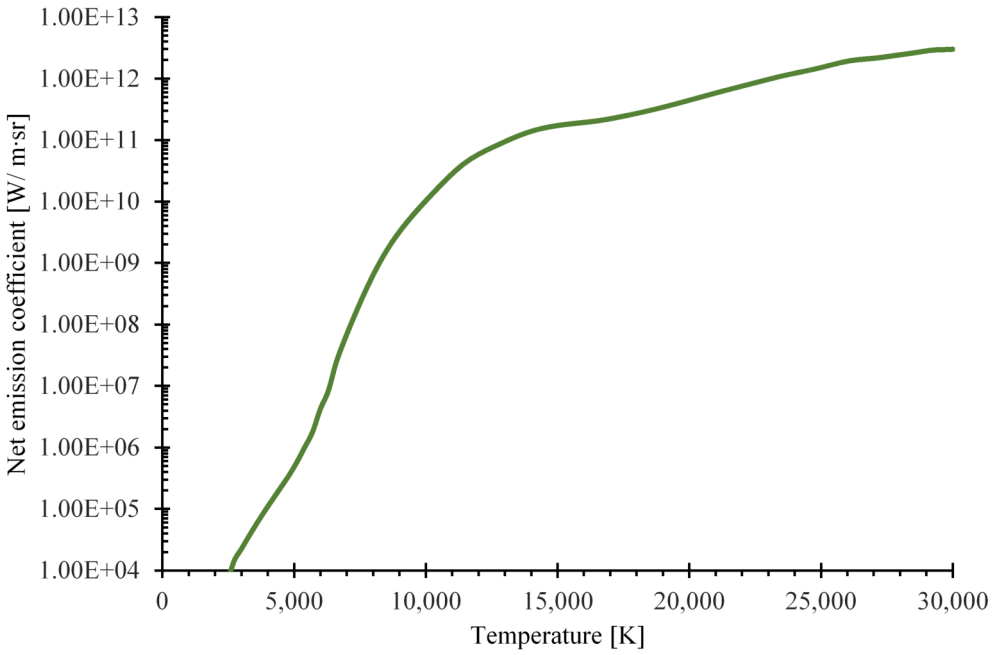

Figure 3.11: Net emission coefficient of air as an optically thin sphere at 1 bar [46], [47].

Another way to implement radiative losses on air-plasma is using models like the P1, Rosseland, or DO, where the calculation is based on the mean absorption coefficient. Bogatyreva et al. [48] have calculated the Rosseland and Plank mean absorption coefficients. Each method is only appropriate in certain circumstances. The Rosseland is appropriate when the system approaches equilibrium, absorbing/emitting almost all the radiation. The Plank model is also appropriate for the optically thin assumption in the LTE approach.
Figure 3.12 shows the Plank mean absorption coefficients for seven bands in the range of 0.01 to 6.0×10^{15} s^{-1}. Table 3.2 specifies the boundary frequencies for each group.

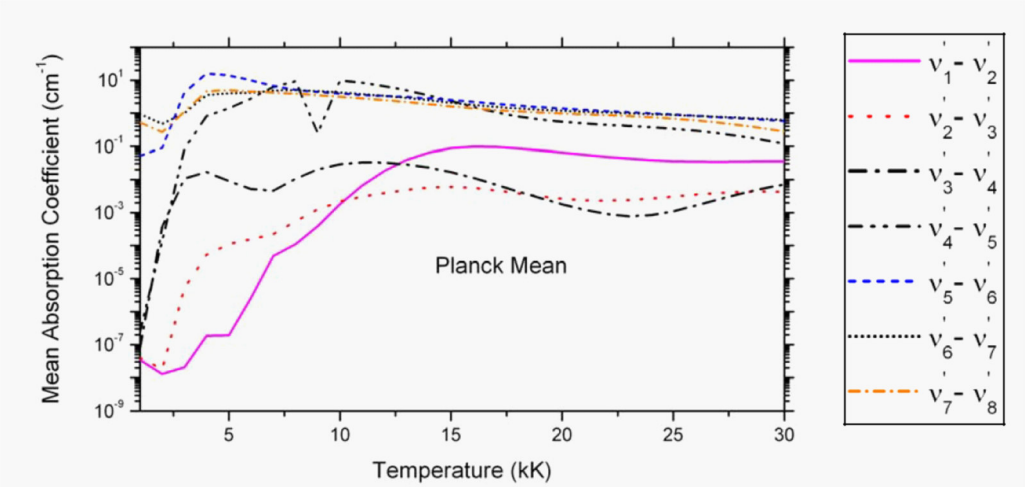

Figure 3.12: Planck mean absorption coefficient for seven specific groups, with a quasi-uniform splitting [48].

Table 3.2: Frequency $\left(v_k\ x10^{15}\ s^{-1}\right)$ groups for the Plank mean absorption coefficients [48].

v_1	v_2	v_3	v_4	v_5	v_6	v_7	v_8
0.01	0.1	1.0	2.0	3.0	4.0	5.0	6.0

Chapter 4

Problem Statement

4.1 Base Design

For this work, a geometry based in a real world circuit breaker used in renewable energy interconnections systems, such as solar panels grid systems and DC batteries that deliver high amperage, was used as the base design. The commercial model used as reference has the following characteristics:

- Up to 250 DC V as nominal operation voltage.
- 50 A as the limit value for overcurrent.
- 10 kA as the ultimate interrupt current the breaker can withstand, but might not be able to be put back in service.

An image with its general dimensions is shown in Figure 4.1.

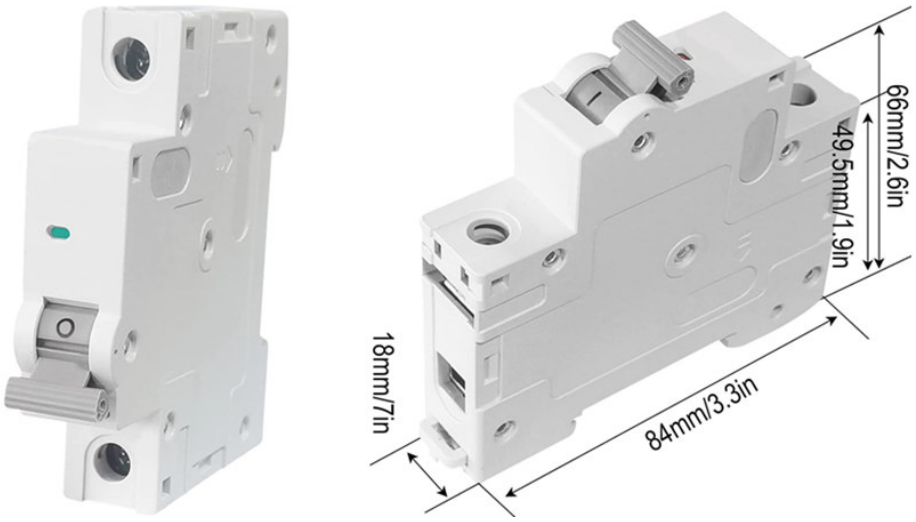

Figure 4.1: Commercial LVCB used as reference geometry.

Figure 4.2 shows the internal view of the components that make the LVCB selected for this study. Henceforth in the analysis, the $Al_{electrode}$ will be considered as the cathode and the $FE_{electrode}$ wil be the anode.

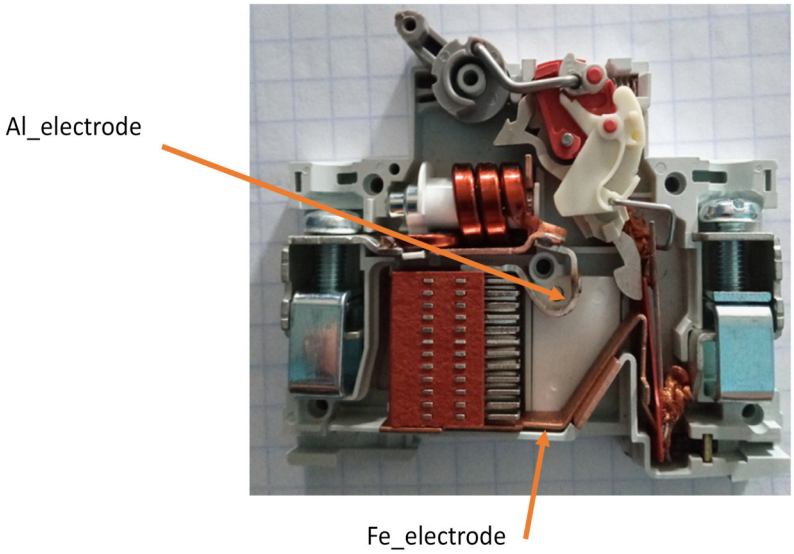

Figure 4.2: Internal view of a commercial LVCB.

Figure 4.3 shows the region that will be considered as the extinguishing chamber. This region is delimited by the blue line, and includes cathode, anode, and the splitter plates, as wall as the fluid domain that will be considered.

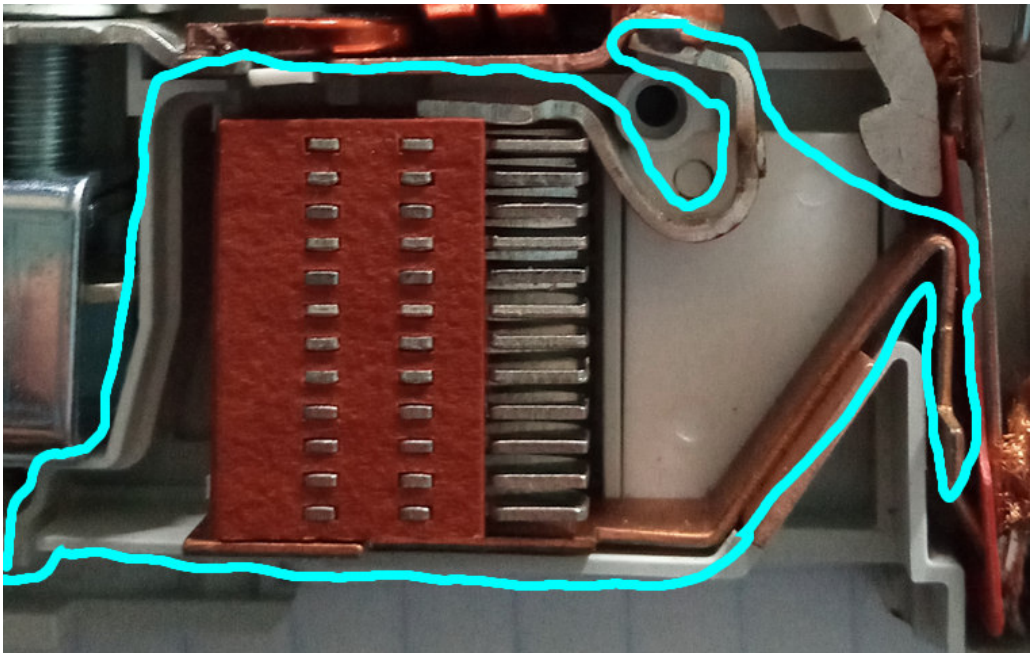

Figure 4.3: Extinguishing chamber of a commercial LVCB.

Figure 4.4 shows the splitter array used in the commercial LVCB used as reference. This array is composed of 12 identical splitter plates.

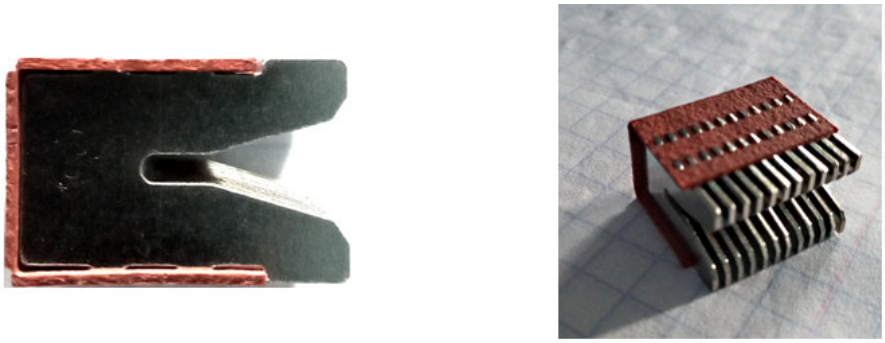

Figure 4.4: Splitter array of a commercial LVCB.

Figure 4.5 shows a 3D representation of the extinguishing chamber based in the physical device used as reference. The main parts are indicated, as

well as the plasma column that will be considered.

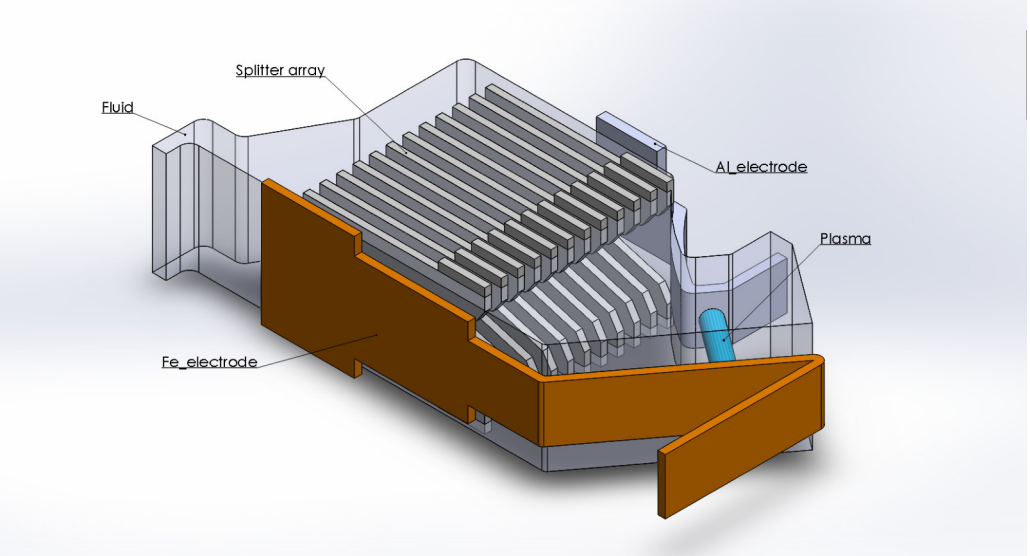

Figure 4.5: $3D$ geometry of an extinguishing chamber based on a commercial model.

4.2 Simulation Procedure

The 3D model of Figure 4.5 is still very complex and includes parts that can cause problems when making the mesh that will be used in the numerical simulations. To solve this, a simplified extinguishing chamber will be considered.

Figure 4.6 shows the simplified geometry for the DC LVCB extinguishing chamber used in the numerical simulations.

The materials are:

- Cathode - aluminum.
- Anode - iron.

- Splitter plates - iron.
- Fluid - air.
- Plasma - air (initial conditions at 1×10^4 K and atmospheric pressure).

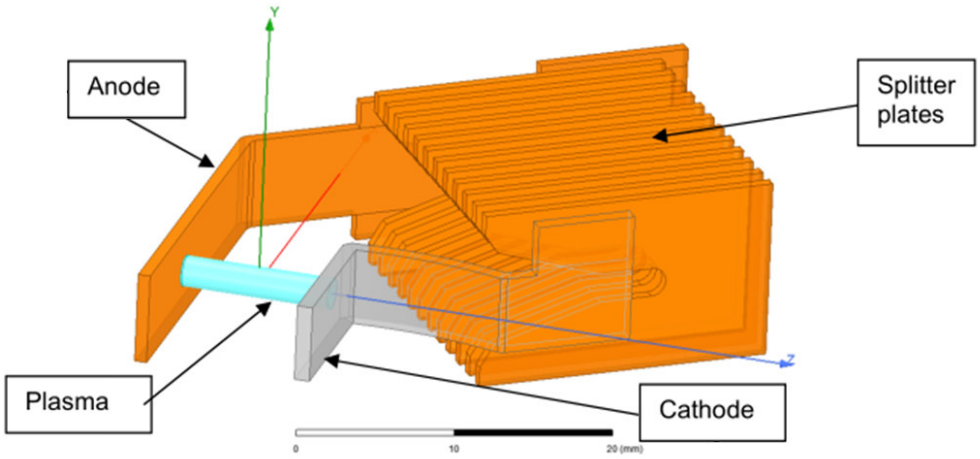

Figure 4.6: Simplified geometry of an extinguishing chamber.

CAD drawings for each component can be found in the Appendix section, as well as their dimensions.

4.2.1 Boundary Conditions

The simulation process is based on the magnetohydrodynamic theory (MHD). This discipline studies fluid dynamics in the presence of electric and magnetic fields.

The initial conditions are temperatures at 300 K and atmospheric pressure in the fluid domain. The external walls in the model are considered adiabatic and with a no-slip boundary condition. The vents serve as hot air outlets and for recirculation of air. The vents are at atmospheric pressure conditions.

The fluid domain is static at the beginning of the simulation.

The electromagnetic conditions are conductivity in the entire fluid domain as a function of temperature [33]. The initial electrical current is 100 A entering through the frontal face of the cathode (according to Figure 4.6). The electrical current flux is then produced by applying a voltage of 0 V to the frontal face of the anode. The arc is modeled as an air-plasma cylinder at 10,000 K, with temperature-dependent properties according to the literature [19][31][32][33][34].

The NEC radiation model is taken as the radiation contribution to the energy equation in the model.

The plasma cylinder is static at the beginning of the simulation and the movement of the electric arc is initially produced by the electromagnetic forces. In reality, the electric arc is produced at the moment of disconnection of the circuit when the gap is zero. The electric arc then travels between the electrodes and would be moving as it approaches the splitter plate. Arc ignition and contact opening are not considered in this study in order to simplify the model.

The arc roots are modeled as a fluid layer of 0.1 mm thick covering the surface of the electrodes and splitter plates that is in direct contact with the fluid domain.

For the cathode and anode, a 14.5 V and 2.1 V voltage drop was considered in the arc root region, respectively. In the splitter plate arc roots, a mean voltage drop of 8.3 V was considered as an approximation, given that the different faces of the splitter plates can be considered as arc roots of a similar nature as the cathode or anode depending on the angle in witch the plasma column is touching them.

The ANSYS FLUENT® (CFD) and ANSYS MAXWELL® (FEA) software were used with the implementation of a user-defined function (UDF). The UDF controls the initialization and importation into FLUENT® of the electromagnetic results calculated by ANSYS MAXWELL® at the beginning of each time step. ANSYS FLUENT® is able to calculate the heat generation effect due to the Joule heating phenomenon including the electric potential

equation in the model. The UDF also adds the contribution by the Lorentz forces in the momentum equation. Once these effects are incorporated, the fluid dynamics equations are solved in ANSYS FLUENT®. The UDF is included in the Appendix section.

The results are then exported to ANSYS MAXWELL® and the electromagnetism interactions are calculated again. The process is then cyclically repeated.

Of the materials proposed on this work for the splitter plate, iron is a ferromagnetic material, but aluminum is not. The electric arc can be conceptualized as a conductor with electricity flowing through it. This means that there is a magnetic field around it that can interact with other magnetics fields and other ferromagnetic materials. These interactions can affect the movement of the electric arc.

4.2.2 Considerations

In summary, the mathematical model for the numerical simulation has the following considerations:

- Air-plasma properties such as electrical and thermal conductivity, specific heat, viscosity and density, are considered as a function of temperature.
- Symmetry conditions are not considered in the 3D model.
- Electromagnetic contributions to the energy and momentum equations are calculated at the end of each timestep.
- The radiation model being considered is the NEC model.
- Arc ignition and contact opening are not considered in the simulation.

- All the elements in the model are static when the simulation starts.
- A model of voltage drop in the arc roots is considered for the electrode materials aluminum-iron (Al-Fe).
- The fluid flow is modeled using the $\kappa - \epsilon$ turbulence model.
- There is no deionization phenomenon model included in the calculations.
- The effective arc extinction is taken as the electric arc being split and the electrodes no longer connected by it [30].

4.3 Proposed designs

The first design, shown in Figure 4.7, is a simplified extinguishing chamber based on a commercial DC LVCB.

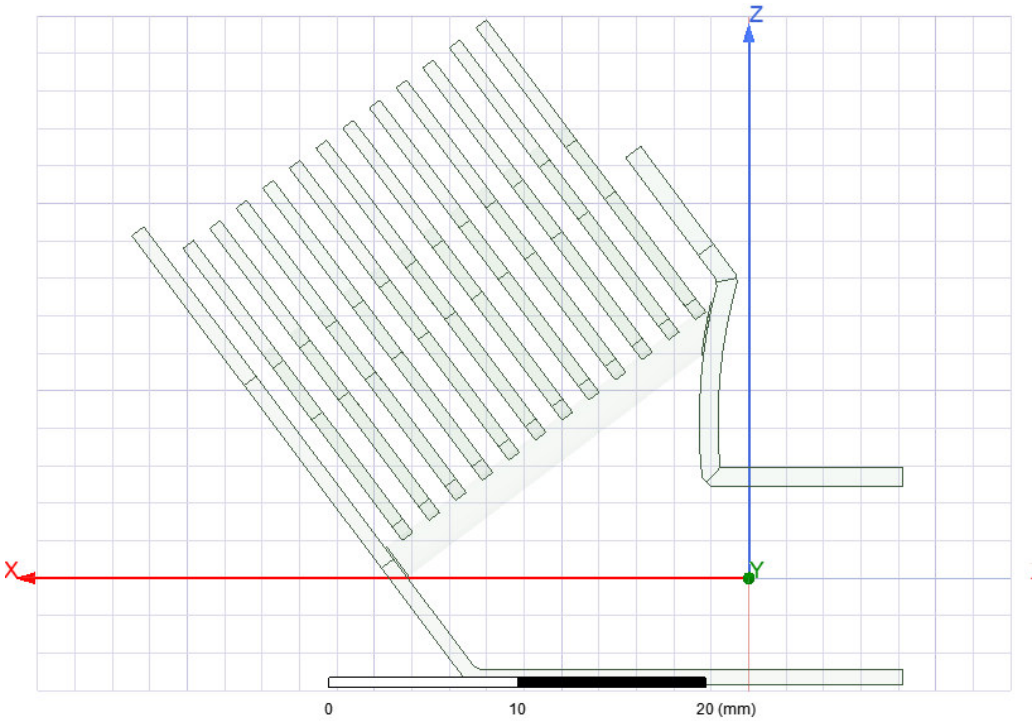

Figure 4.7: Base design with aligned splitter plates (Original).

Figure 4.8 shows the second proposed geometry. In this case, the splitter plates of the lower part (the ones closer to the anode) were displaced at a sequential value of 3.1876999/11 mm, with respect to the one before it. This proposal, as it is with the rest of the rest of new geometries proposed, was based in a simple redesign that does not require a modification of the extinguishing chamber, nor increasing the needed mass of materials, by modifying only the splitter plates arrangement. The name of this proposal is Bottom Displaced or BottomDisp

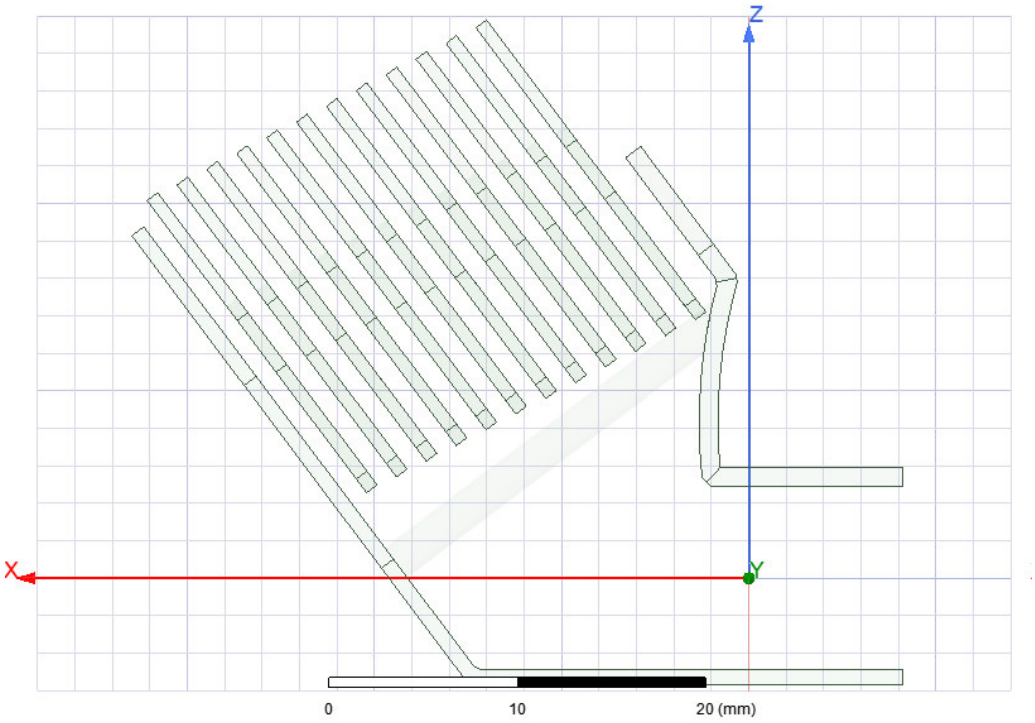

Figure 4.8: Modified design with displacement of the lower splitter plates (BottomDisp).

The third geometry, shown in Figure 4.9, was obtained by displacing 3.1876999/11 mm each splitter plate, with respect to the one before it, starting with the second splitter plate from the bottom. The name given to this proposal will be Upper Displaced, or TopDisp.

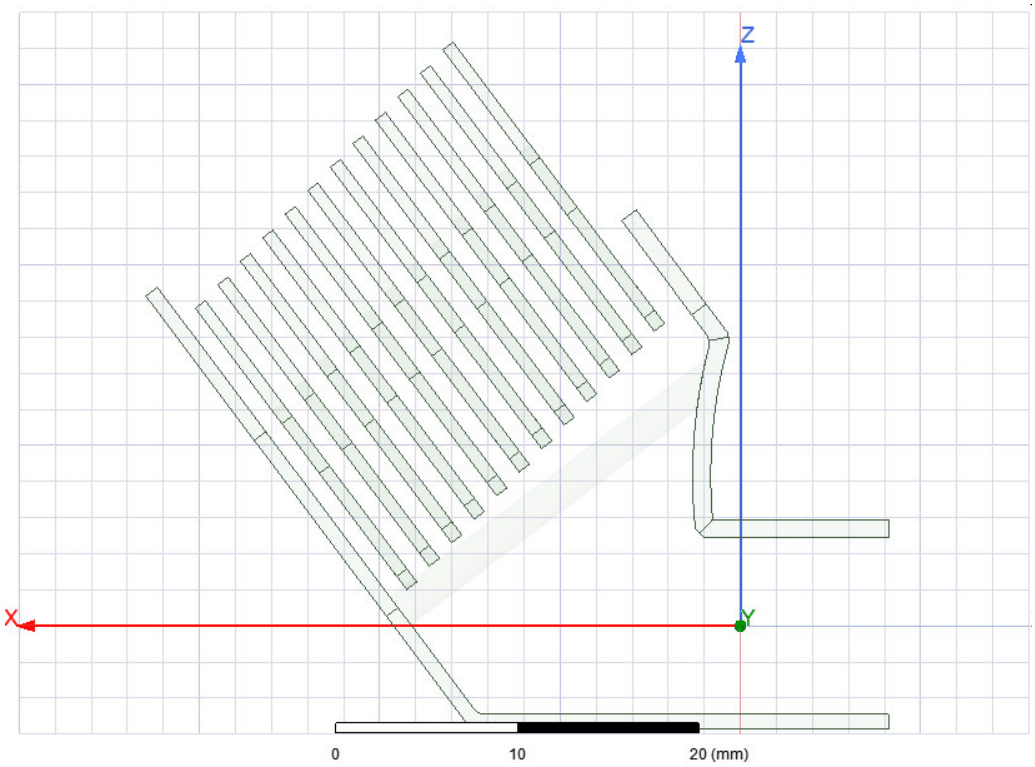

Figure 4.9: Modified design with displacement of the upper splitter plates (TopDisp).

The last geometry proposed in this work (Figure 4.10), is also based in a modification of the Original geometry, now with a displacement of 3.18766999/5 mm of each splitter plate with respect to the one before it, starting with the 5^{th} and 8^{th} splitter plate, respectively. That is, the two splitter plates at the center, the 6^{th} and 7^{th} splitter plates, are let in their original positions and used as reference for the displacement of the other splitter plates. The name that will be given to this proposed geometry is Sides Displaced, or SidesDisp.

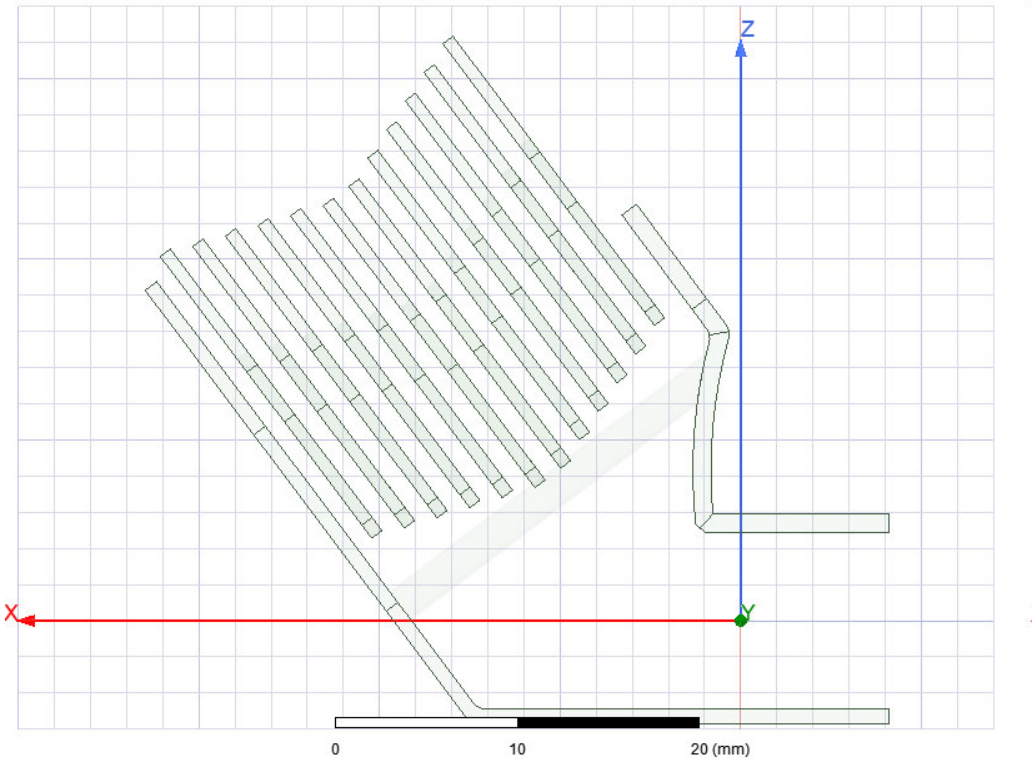

Figure 4.10: Modified design with displacement of the upper and lower splitter plates (SidesDisp).

As a starting point in the analysis, and with the intention of picking the best two geometries without wasting computer power and time, a pre-analysis is proposed. This pre-analysis will consist of a simulation solely based in the electromagnetic behavior of the extinguishing chambers proposed.

The aim of this pre-analysis is to put a plasma column near the splitter plates, numerically simulate for current density, electrical potential, and magnetic field density, and with these results calculate the force density that is felt by the plasma column. This analysis can be carried out using ANSYS MAXWELL®

This will tell us, as a good approximation, which geometries have a bigger chance of splitting the arc in a shorter amount of time, without needing to simulate the more complex mathematical model, which does take as much

as 50 times longer to converge.

However, this pre-analysis will not give us the specifics of the arc propagation process nor the predicted arc extinction time.

The results for the proposed simulations are presented in the next chapter.

Chapter 5

Results

5.1 Mesh sensibility

To obtain a reasonable number of elements for the mesh and good results in the simulations, a mesh sensibility analysis is required. For this, the arc propagation process was evaluated until 3 μs, at different mesh densities. The evaluated values for the mesh sensibility analysis were the mean temperature (T_{mean}) and mean electrical current density (J_{mean}).

Figure 5.1 shows the variation of T_{mean} and J_{mean} when increasing the mesh elements from 9×10^6 to 15.1×10^6.

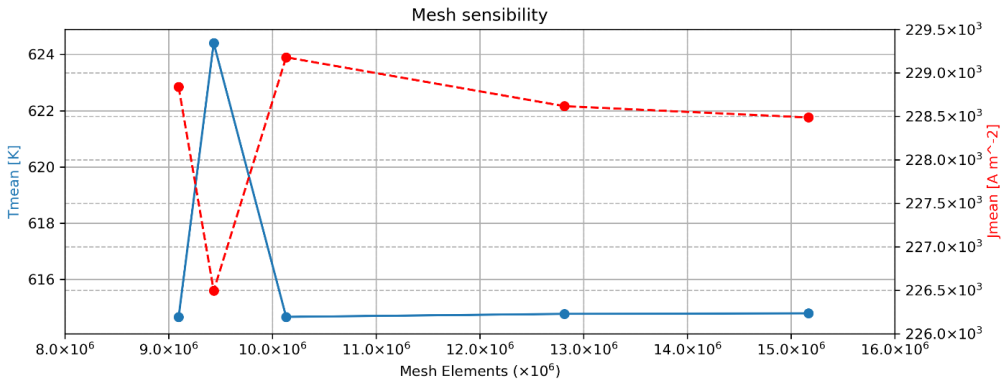

Figure 5.1: Variation of T_{mean} and J_{mean} at different mesh densities.

The difference in error after each mesh number of elements increase is shown in the Table 5.1.

Table 5.1: Mesh sensibility analysis after each mesh element increment.

Mesh Elements	T_{mean} [K]	% error T_{mean}	J_{mean}[A/m^{-2}]	% error J_{mean}
9096960	614.660000	—	228837	—
9434859	624.405000	1.560686	226494	1.034464
10133001	614.669000	0.001464	229178	0.148793
12815853	614.775000	0.018706	228616	0.096669
15167541	614.794000	0.021796	228486	0.153620

Based on the results of Table 5.1, a mesh of approximately 13×10^6 elements is a good enough mesh that offers a good balance between precision and computation costs, given that, beyond this point, the precision of the results do not increase by a significant margin with the number of elements, but the time required to achieve convergence in each timestep does.

5.2 Steady state analysis: Attraction forces in the plasma column

For the four proposed geometries in this work, the only significant change produced was splitter plate position. Given that the Lorentz Forces are a combination of the effect of magnetic flux and electrical current magnitude, we can start making predictions for which geometries have the potential of reducing the arc extinction time if we make a pre-analysis of the forces felt by the plasma column for steady state conditions. This pre-analysis will be carried out in ANSYS MAXWELL ®.

To visualize what will contribute to the arc forces felt by the plasma column, Figure 5.2 shows the electrical current magnitude (J) in the Original geometry, if we were to put a plasma column near the splitter plates, with the same 100 A as boundary condition.

Properties for the electrodes and splitter plates are taken at atmospheric conditions, and the same applies for fluid zones, except for the plasma column region, which is taken as having properties of air-plasma at 10,000 K.

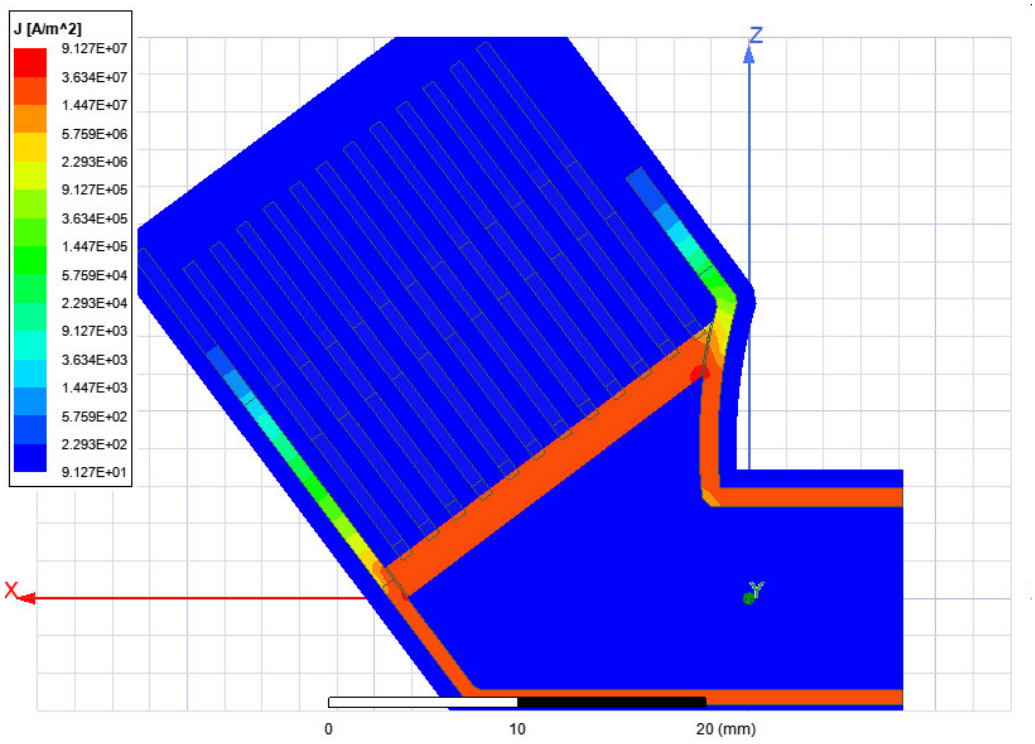

Figure 5.2: Current density produced by a plasma column near the splitter plates (Original geometry).

The electrical current magnitude is practically identical for each geometry, given that it is affected mostly by the conductors in the conduction path and, for this pre-analysis, it doesn't change in any case. You can verify this in the Appendix section for these results.

What will change in the steady-state analysis for each case when a plasma column is near the splitter plates, is the magnetic field (B). The magnetic field in each of the cases analyzed is produced by the ferromagnetic materials in the presence of an electrical current flux. Given that the positioning of the splitter plates changes, the magnetic field B will be different in each geometry

and will have a different shape. This will produce a different resulting force applied to the plasma column for each geometry.

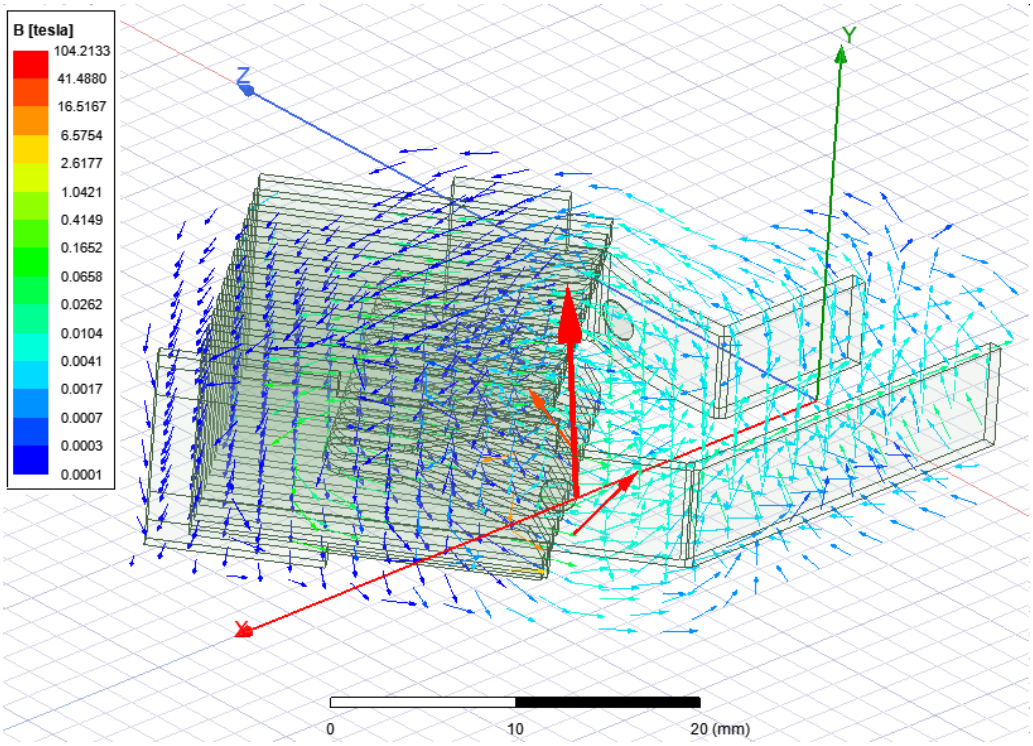

Figure 5.3: Magnetic flux density produced by a plasma column near the splitter plates (Original geometry).

Figure 5.3 shows the magnetic field B vectors in the Original geometry. The magnetic field for each geometry is in the Appendix section.

The important point of this analysis is finding what will be the effect of changing the splitter plate configuration. None of the splitter plates are closer than the original, and the resulting magnetic field is the most worthwhile change that can be observed for each case.

With the results of the steady state analysis, we can calculate the force felt by the plasma in two ways, the force felt by the plasma column in its surface, and the volume force density felt in a line along the center of the

plasma.

Figure 5.4 shows the force vectors in the surface of the plasma column in the Original geometry. We can observe that the resulting force will have a general direction towards the splitter plates, and the strongest force is felt at the cathode side.

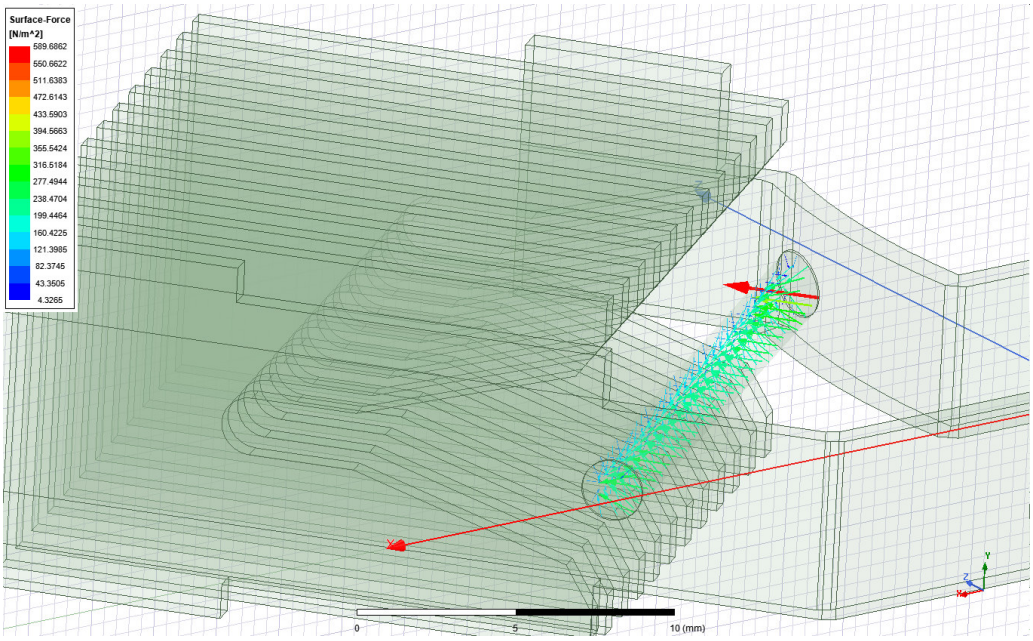

Figure 5.4: Area force density in the plasma column – Original geometry.

Surface force in the plasma column of the Bottom Displaced geometry is shown in Figure 5.5. We can observe that the resulting force will have a general direction towards the splitter plates, and the strongest force is felt at the cathode side, same as in the Original geometry. However, the peak surface force is bigger than in the Original geometry by $3.5 N/m^2$. Whether this has a real impact in the arc propagation process and extinction time will be analyzed in the transient analysis.

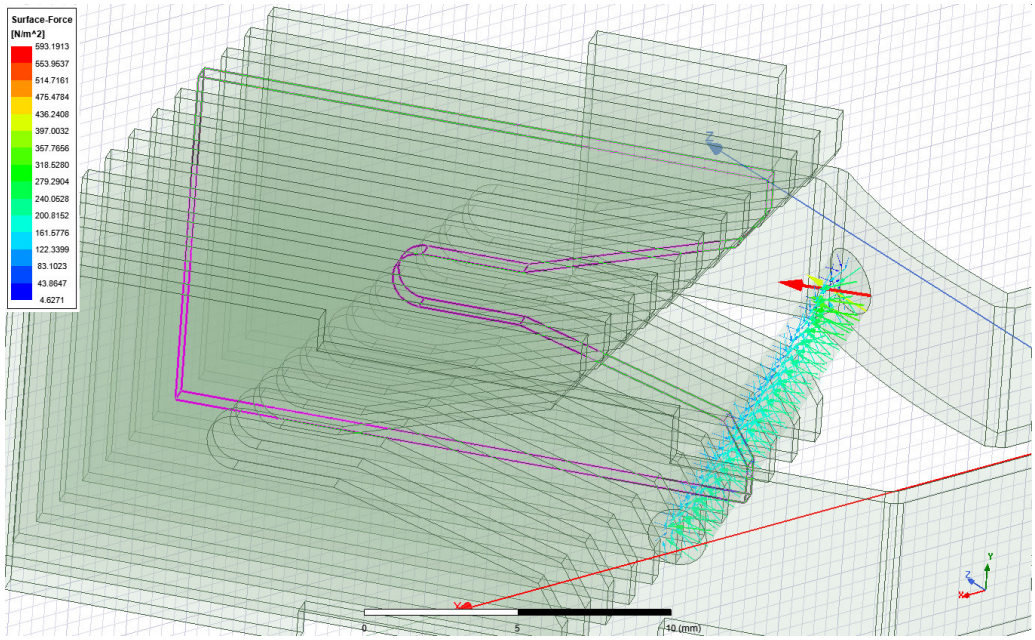

Figure 5.5: Area force density in the plasma column – Bottom Displaced geometry.

The results for the surface force felt by the plasma column in the Top Displaced and Sides Displaced geometries are show in the two figures below. We can observe that for these cases, a bigger peak force in the general direction of the splitter plates was not achieved.

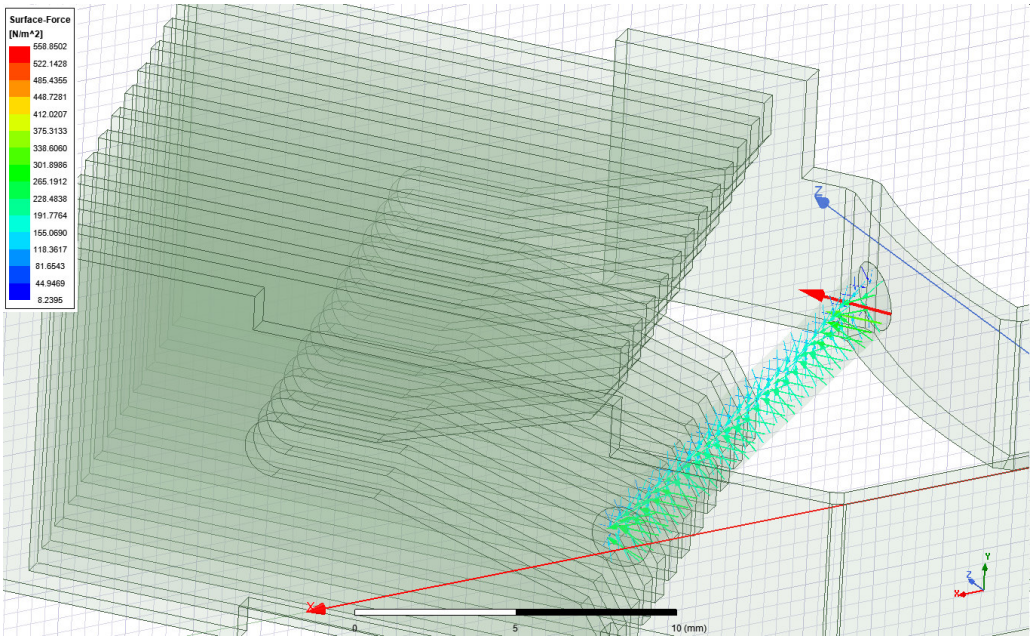

Figure 5.6: Area force density in the plasma column – Top Displaced geometry.

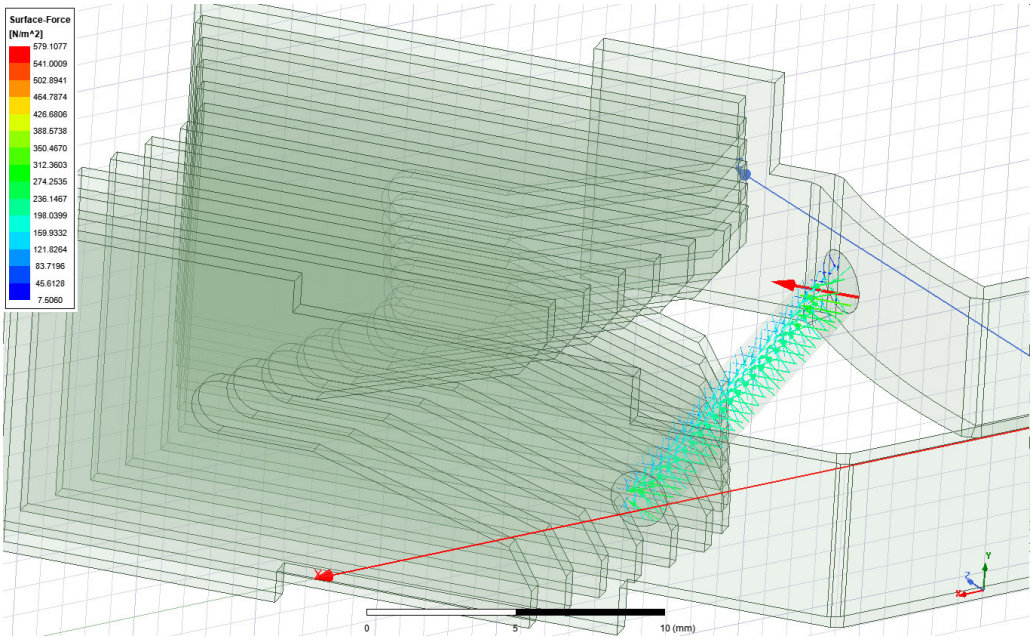

Figure 5.7: Area force density in the plasma column – Sides Displaced geometry.

As a way to condense the results of surface forces felt by the arc, Figure 5.8 shows the volume force density that can be felt by a line that runs along the center of the plasma column, from the cathode to the anode side.

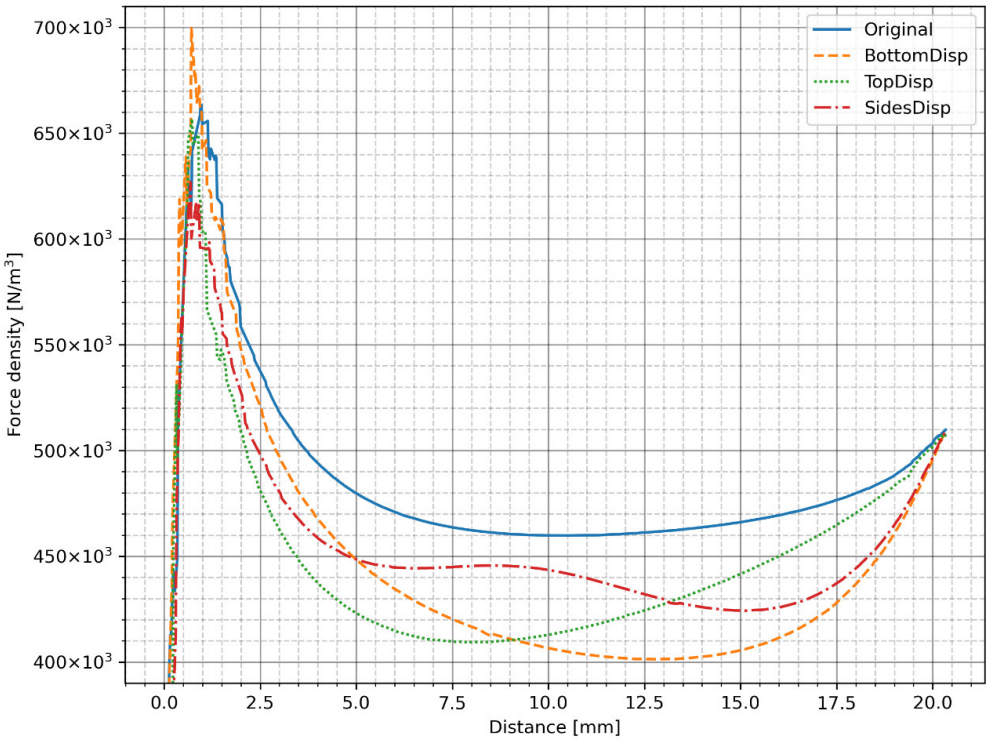

Figure 5.8: Volume Force density comparison along the plasma column for the different geometries proposed.

In Figure 5.8, we can see that the results obtained are in accordance with the figures of surface force. The strongest force is felt at the cathode side, and a peak value bigger than the Original geometry is only achieved for the Bottom Displaced geometry, with a total difference in peak volume force density of $40N/m^3$.
According to Figure 5.8, the following points can be highlighted:

- The Original geometry has a more constant behavior along the plasma column, as is expected given that the splitter plates are parallel to the arc.

- The Bottom Displaced geometry has a peak value near the cathode side higher than any other case, however, after the 10 mm mark, the

volume force density is the smallest of all the cases analyzed.

- The Top Displaced geometry has a bigger force than the Sides Displaced and Bottom Displaced geometries only after the 13 mm mark, and it is still smaller than the Original geometry.

- The Sides Displaced geometry is only bigger than the Top Displaced and Bottom Displaced Geometry between the 5.5 and 13 mm marks, and it is not bigger than the Original geometry in any section of the plasma column.

Given that the transient simulation of the arc propagation process will have a very high computational cost and needs a lot of time to achieve convergence in each timestep, only two geometries are selected for the transient analysis.

According to the points discussed above and given that the electrical arc will have the strongest resistance to being split near the cathodes, the two geometries that will be selected are the Original geometry, which has a bigger force felt by the arc overall, and the Bottom Displaced geometry, which has a bigger peak force near the cathode of all the geometries proposed in this work.

5.3 Transient Analysis: Arc propagation simulation

The arc propagation process is simulated numerically in the software ANSYS FLUENT ®, coupled with the software ANSYS MAXWELL ®, using a User Defined Function (UDF) as the connecting point between them.

The propagation of the arc can be better analyzed if we look at the transient behavior of the electrical current magnitude in the extinguishing chamber. The results for the Original geometry are shown in Figure 5.9.

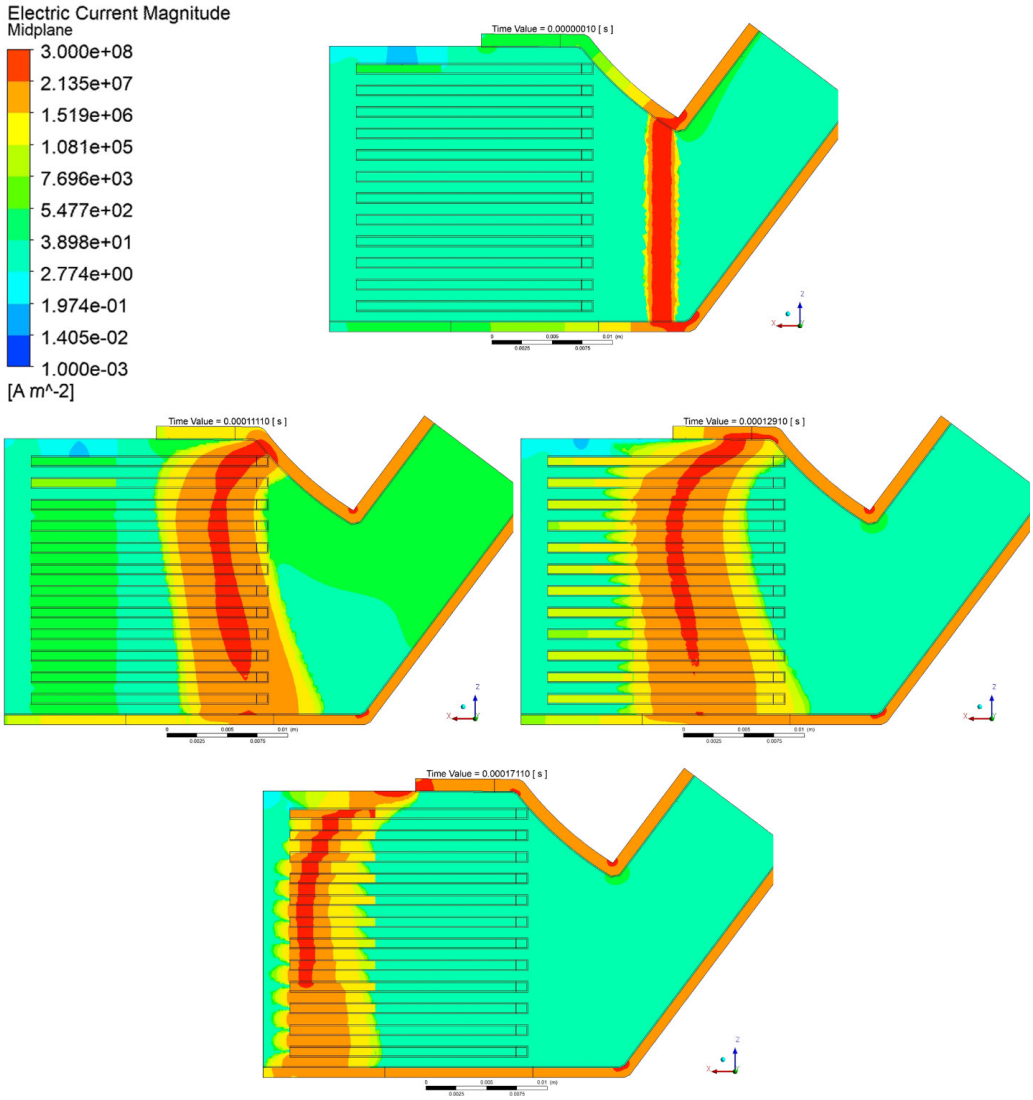

Figure 5.9: Electrical Current Magnitude for the Original geometry at 0.1 μs, 111.1 μs, 129.1 μs and 171.1 μs.

Analyzing the movement of the arc, we can see that at the beginning of the process, the electric arc was attracted by the splitter plates and the arc increased its size when it got in the proximity of the splitter plates. Near the end of the simulation, the arc was attached to the cathode by slim strand that got disconnected once it became too thin.
As discussed in the previous section, the electric arc ionization and deionization

process was not included in the numerical model, so the real dissipation process of the electric arc cannot be reproduced. As it is, the physical disconnection of the arc will be taken as the arc being successfully split.

For the Bottom Displaced geometry, Figure 5.10 shows how the arc propagation process was carried out.

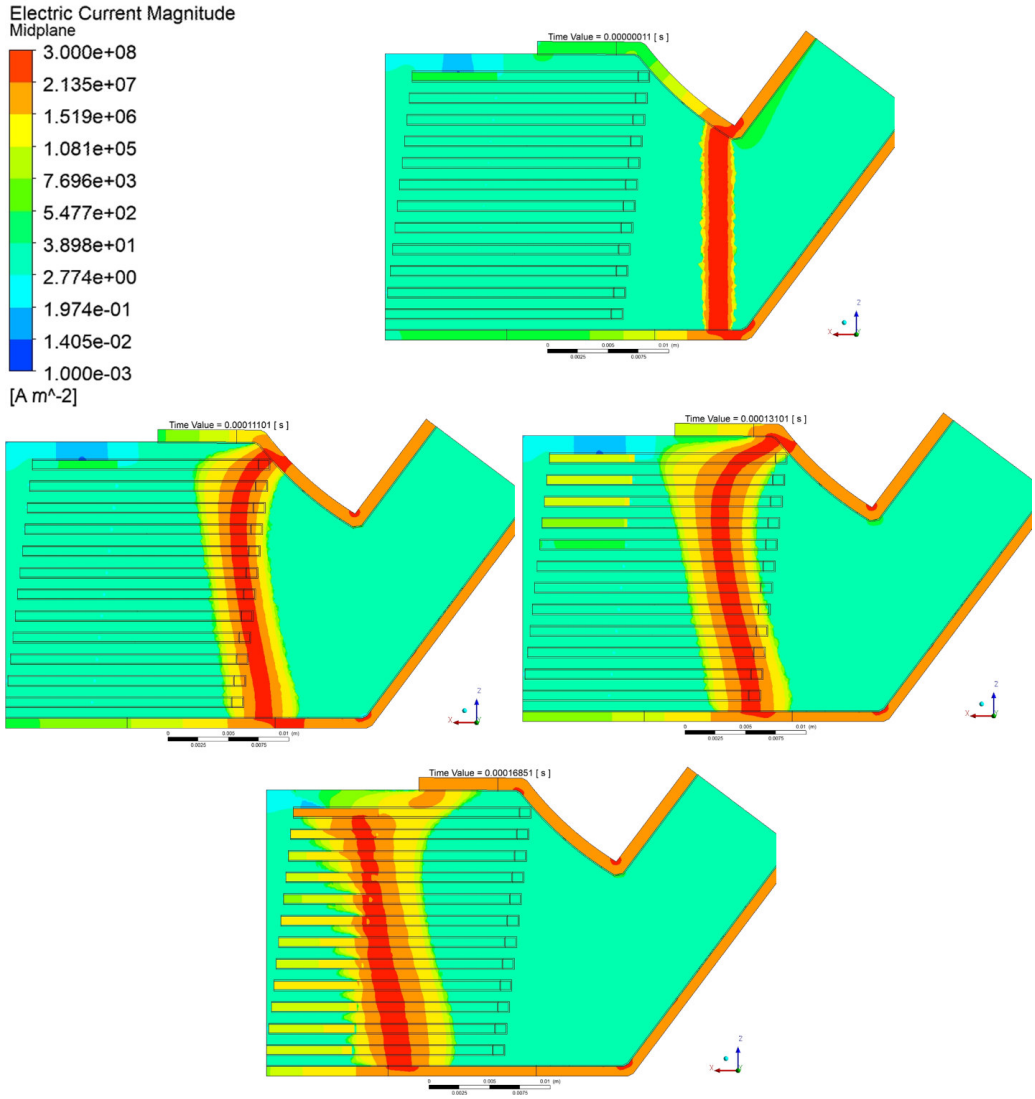

Figure 5.10: Electrical Current Magnitude for the Original geometry at 0.11 μs, 111.01 μs, 131.01 μs, and 168.51 μs.

Contrary to what happened with the Original geometry, the arc didn't swell in size as much, and the disconnection of the arc happened sooner. We can observe that the arc was split with a stronger pull from the top, and the arc didn't remain attached to the cathode with a slim thread, which happened in the Original geometry.

As a way to better compare the transient behavior of the arc propagation process, the hottest temperature in the plasma column was tracked. This temperature will occur at the point in which the most energy is flowing across the plasma column, that is, the slimmest part of the arc. Figure 5.11 shows the position of the hottest point in the fluid versus the flow time.

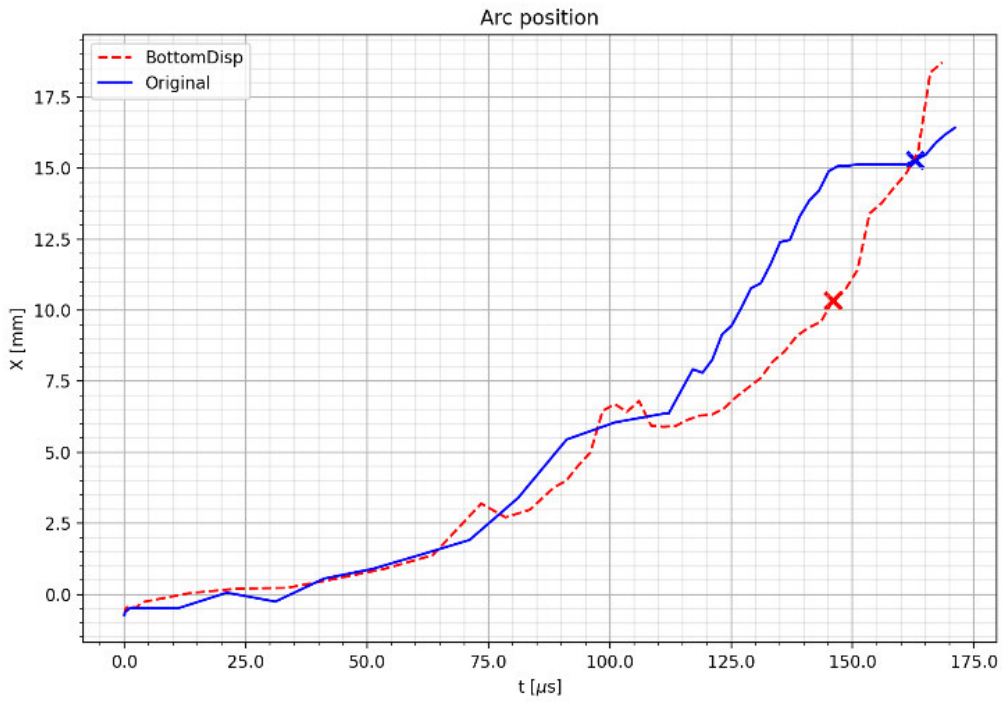

Figure 5.11: Thinnest part of the arc tracked since the arc ignition until its extinction.

Analyzing Figure 5.11, we can conclude the following:

- Until the 120 μs mark, the position of the hottest point is approximately the same for both cases.

- After 120 μs, the Original geometry shows a faster movement of the electric arc, but it gets stuck at the $15mm$ point, which is the furthest

point of the cathode. The arc in the Original geometry is split at 169.1 μs.

- The Bottom Displaced geometry did not get stuck like in the Original geometry, and a visual separation of the plasma column occurs at 146.01 μs. After this point, a steep increase in the movement of the arc is observed given that the arc is no longer connected to the cathode.

Wear in the materials is a problem that needs to be considered in LVCBs. This can be analyzed if we consider the elevated temperatures in the extinguishing chamber and for how long are they in contact with the electrodes and the splitter plates. Remembering that the working fluid in this work is atmospheric air, we can correlate the combination of these two factors to the oxidation process, which will be the main cause of wear in a LVCB.
To decide which of the two geometries selected for the transient analysis has the potential of producing less wear in the materials, the mean temperature of the fluid domain was plotted against the flow time in Figure 5.12.

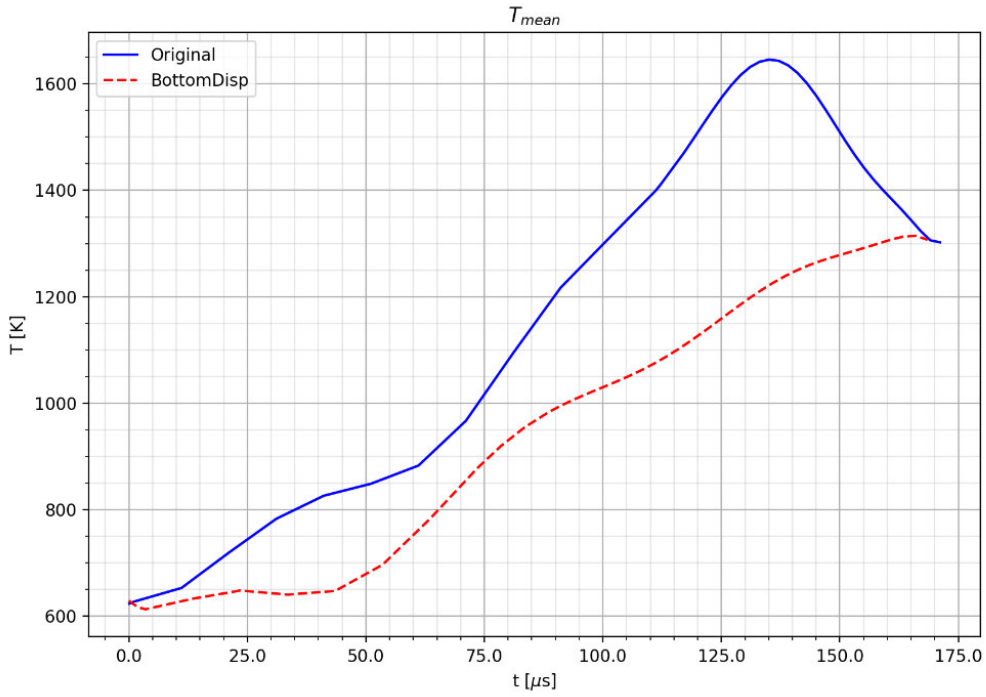

Figure 5.12: Mean temperature of the fluid domain.

Figure 5.12 shows that, in general, the Bottom Displaced geometry will produce less accumulation of energy in the beginning of the arc propagation, but the temperature at the end of the process is approximately the same. This behavior is expected, given that the Bottom Displaced Geometry is very similar to the Original geometry, but diminishing peak temperatures will help in reducing wear in the materials for real conditions.

We can also observe that the Original geometry has a sudden descent in mean temperature around the 135 μs mark. This is explained by the recirculation of air to the system. That is, part of the air at high temperatures that was in the chamber exited the control volume, and new air at atmospheric conditions was introduced to the system. This reduced the peak mean temperature at the Original geometry (1650 K), and the arc was split shortly after that.

Figure 5.13 shows residual temperatures for the Original and Bottom

Displaced geometries.
We can observe that the Original geometry has a hot point near the cathode, and for the residual temperatures of the Bottom Displaced geometry this does not occur.

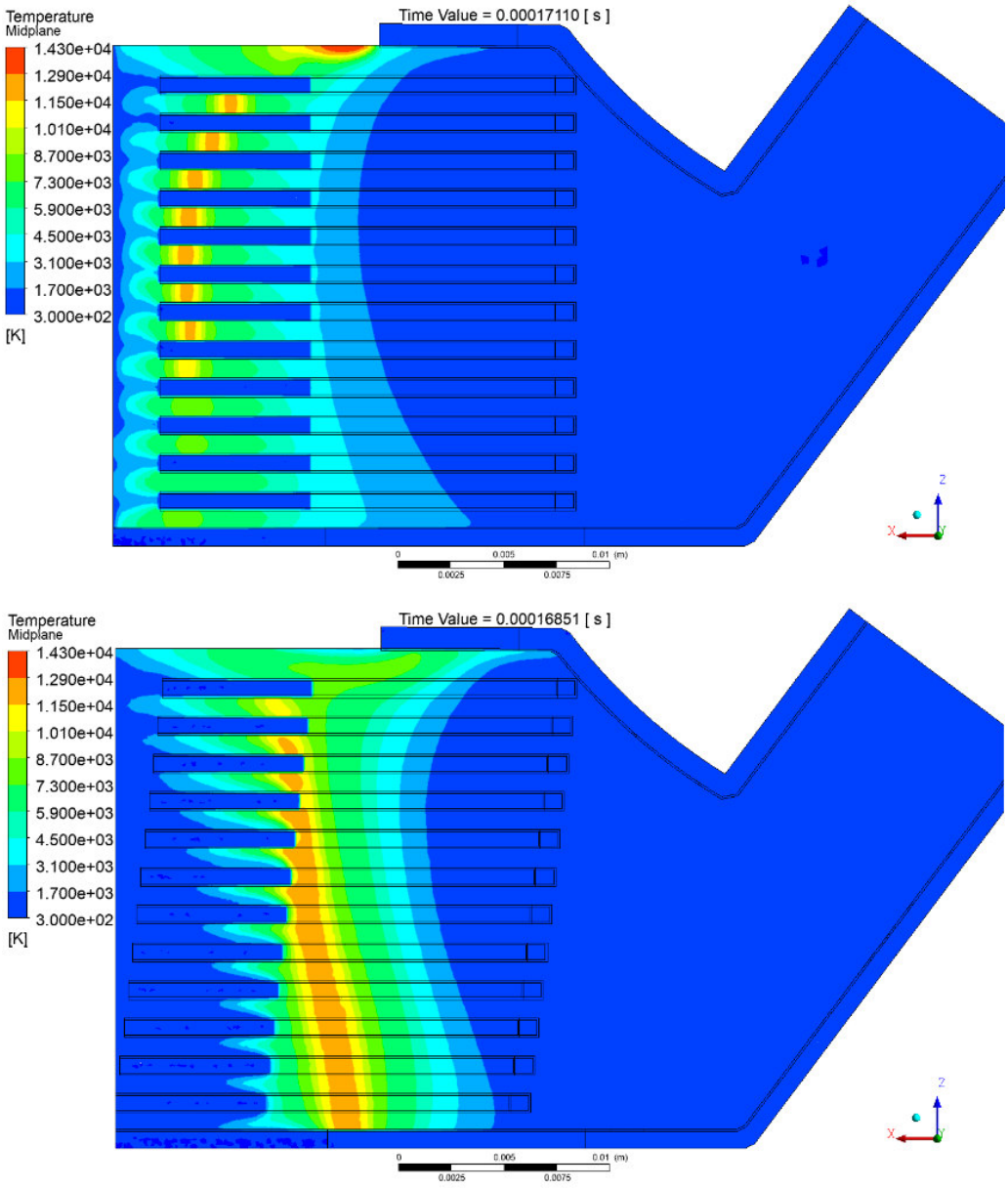

Figure 5.13: Residual temperatures for the Original geometry (top) and Bottom Displaced geometry (bottom).

When it comes to peak temperature reached overall, similar values of 20305 K (at 157.1 μs) and 22626 K (at 73.51 μs) were found for the Original

and Bottom Displaced geometries, respectively.

A complete view of the temperature distribution for the Original and Bottom Displaced geometries is shown in the Appendix section.

Chapter 6

Conclusions and future work

The present work analyses the electric arc propagation process and its effect in a LVCB based in a commercial design. An MHD model capable of replicating the arc behavior was implemented, and geometry modifications that do not require more materials or complicated manufacturing were proposed.

The implementation of a steady state analysis of the electromagnetic forces produced in a plasma column near the splitter plates was proposed as a starting point for selecting which geometries have a higher chance of shortening the arc extinction time. This approach was used given that computational costs for the transient analysis of this phenomenon are very high.

The selection criteria for the best two geometries were peak force value at the surface and across a line in the plasma column. The two geometries that were selected were the Original geometry, that has a better force distribution performance overall, and the Bottom Displaced geometry, which had a peak value of $40N/m^3$ volume force higher than the Original geometry near the cathode.
A more complete analysis can be done by doing the transient simulation of the arc propagation process in the rest of the geometries that were proposed in this work, and repeating the simulations for different input current values.

For the transient analysis, the following main points are presented:

- The Bottom Displaced geometry achieved a decrease in the time required

for the arc extinction of 13.65 %.

- Mean values of peak temperature and overall less energy accumulation was achieved in the Bottom Displaced geometry. This can reduce wear in the materials that make the extinguishing chamber.

It is important to mention that this work was focused in selecting and implementing a numerical model capable of reproducing the complex phenomenon of DC arc propagation and using it to simulate geometries based in commercial applications, with the intention of proposing improvements to this technology. Now that the know-how and the tools required for this task were obtained, future work is expected to come out with the results obtained in this work.

The model used in this work has a good congruency with experimental data, however, many idealizations and suppositions are present in its implementation. A more complex model that reproduces the real behavior is suggested for future studies. The suggested additions to a model for arc propagation simulations are:

- Contact opening.
- Arc ionization and deionization process.
- Variable properties for the solid zones.
- Transient magnetic field.
- Wear in the materials.
- A more complex radiation model.

More complex geometries and the inclusion of permanent magnets to the model will be studied in future works.

Appendix A

Drawing of aluminum electrode

Drawing of the aluminum electrode

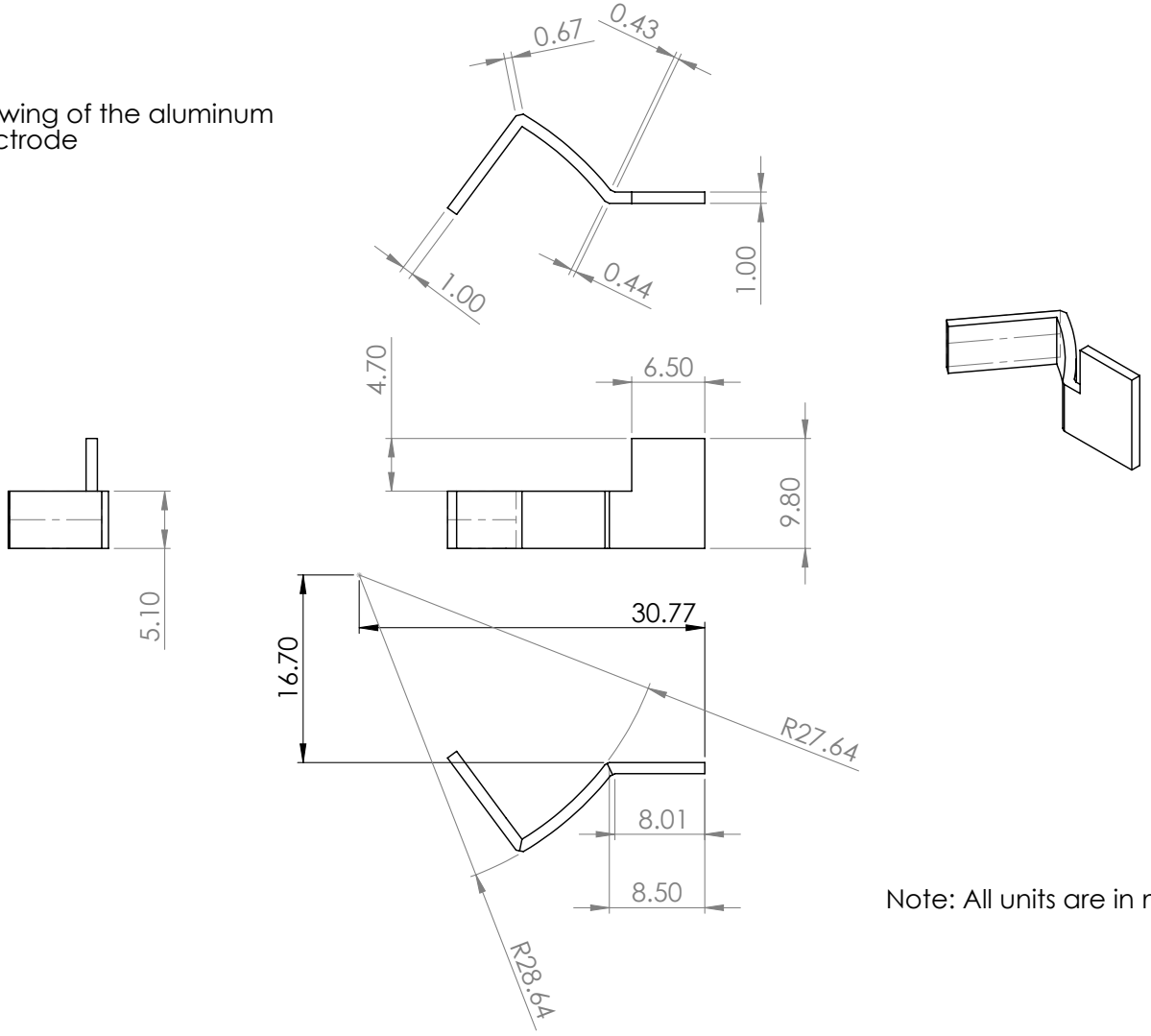

Note: All units are in mm.

Appendix B

Drawing of iron electrode

Drawing of the iron electrode

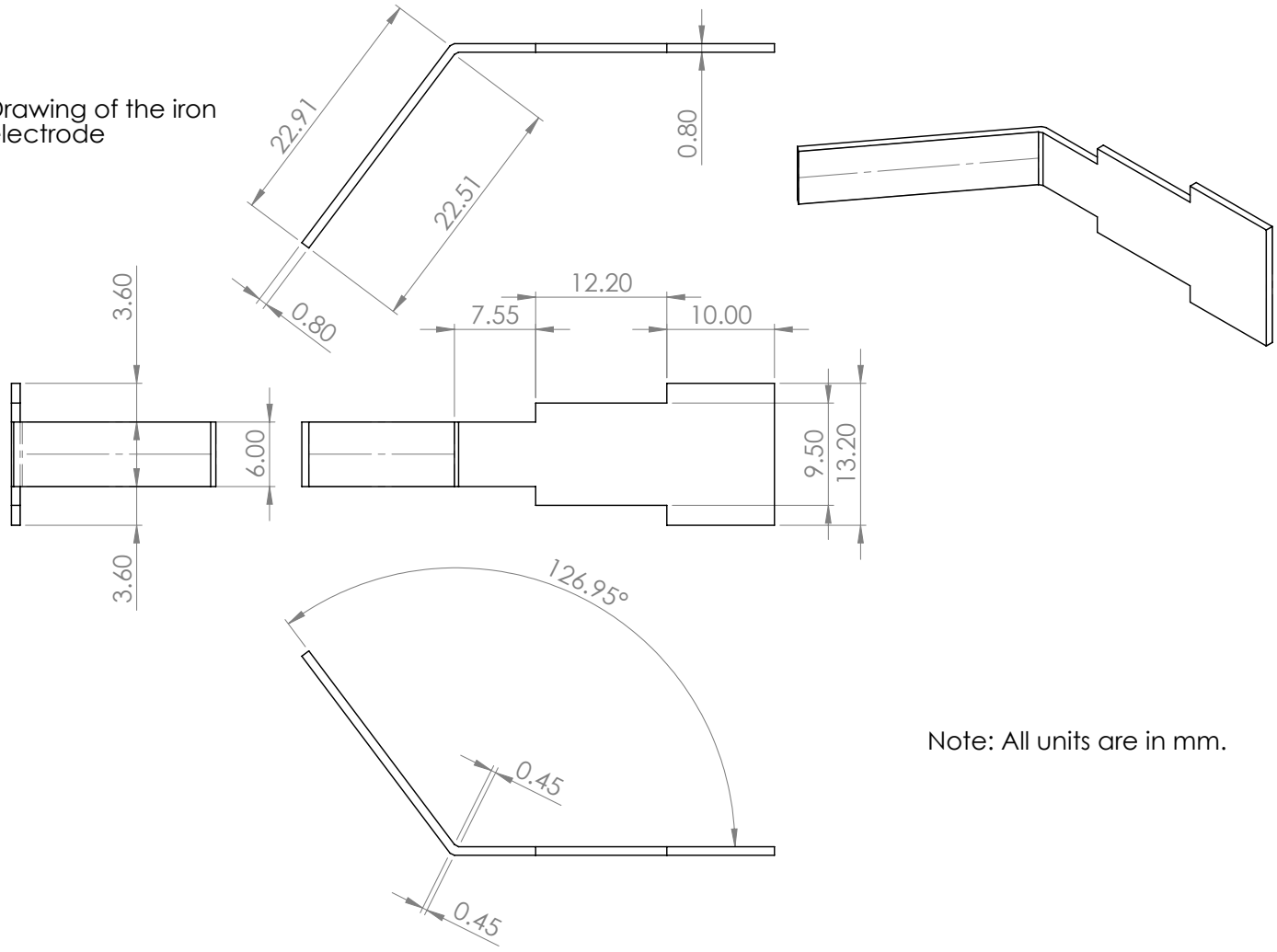

Note: All units are in mm.

Appendix C

Drawing of iron splitter plates array

Note: The splitter plates are equally spaced.

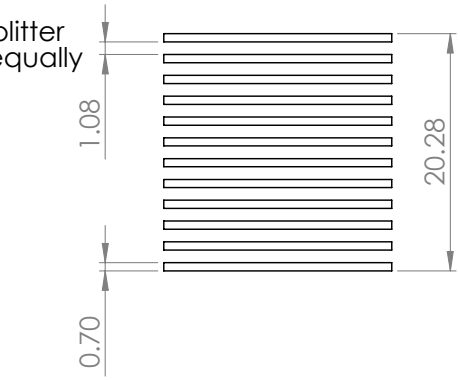

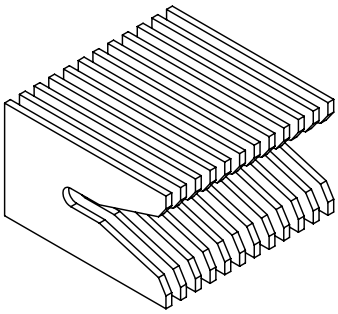

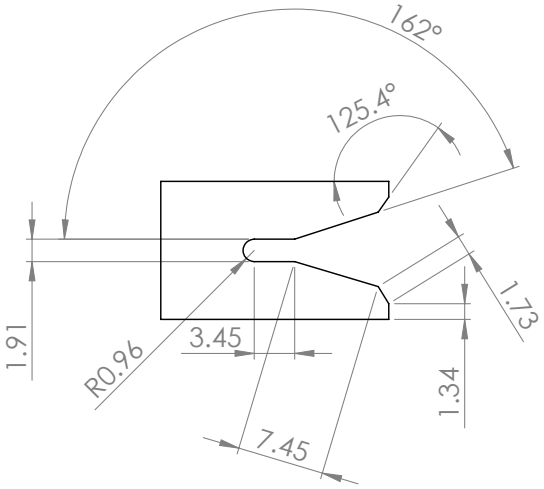

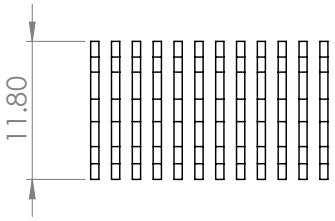

Drawing of the splitter plates array

Note: All units are in mm.

Appendix D

Drawing of the simplified extinguishing chamber

Drawing of the simplified extinguishing chamber

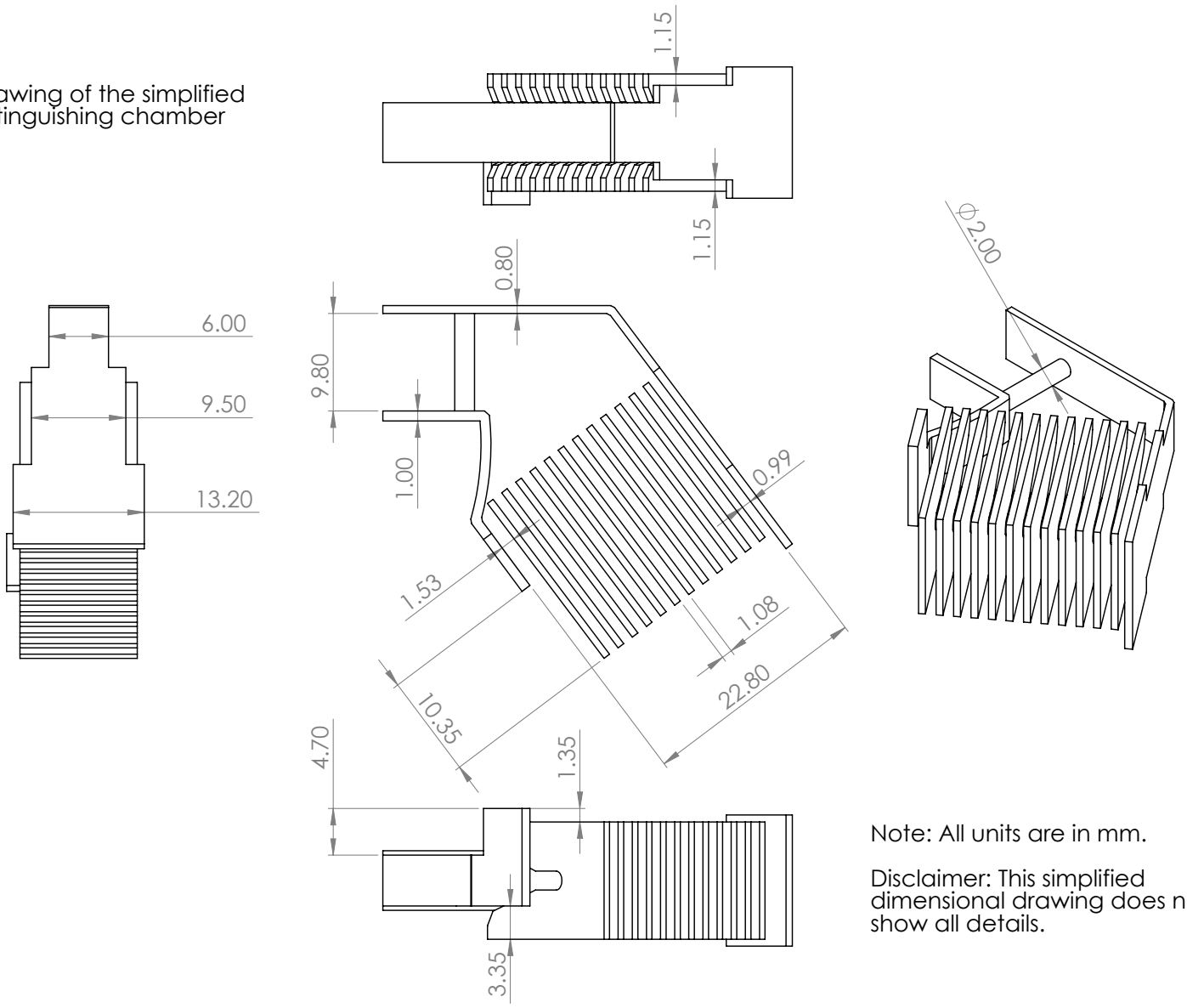

Note: All units are in mm.

Disclaimer: This simplified dimensional drawing does not show all details.

Appendix E

User Defined Function

https://raw.githubusercontent.com/Miguel-N/dc_arc_fluent_maxwell/main/arc_udf.c

Appendix F

Steady State Results

F.1 Magnetic Field

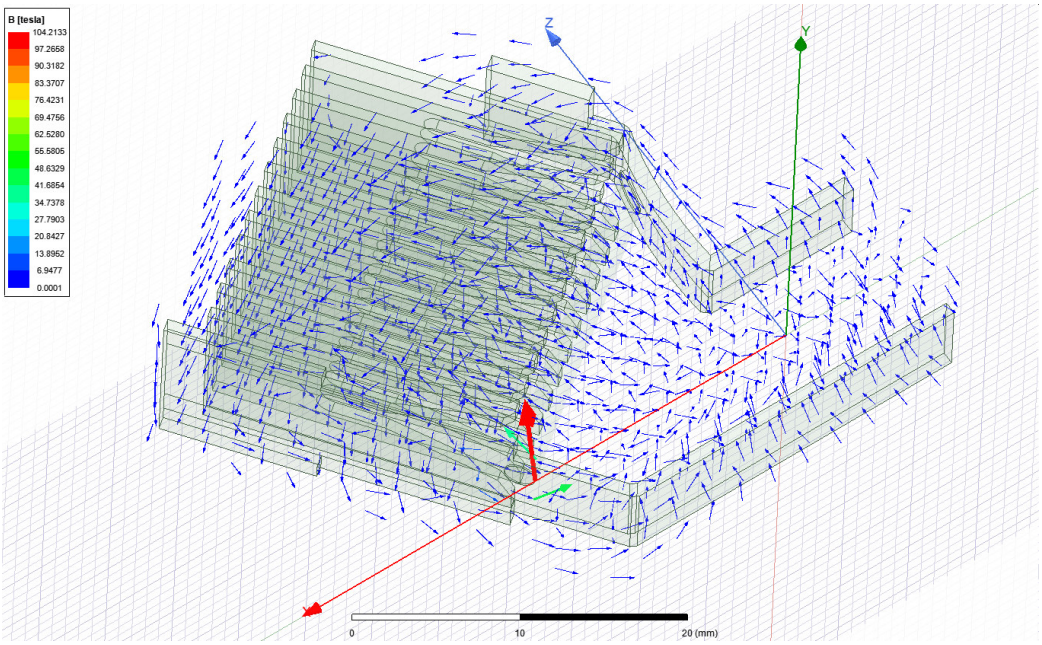

Figure F.1: Magnetic field distribution - Original geometry.

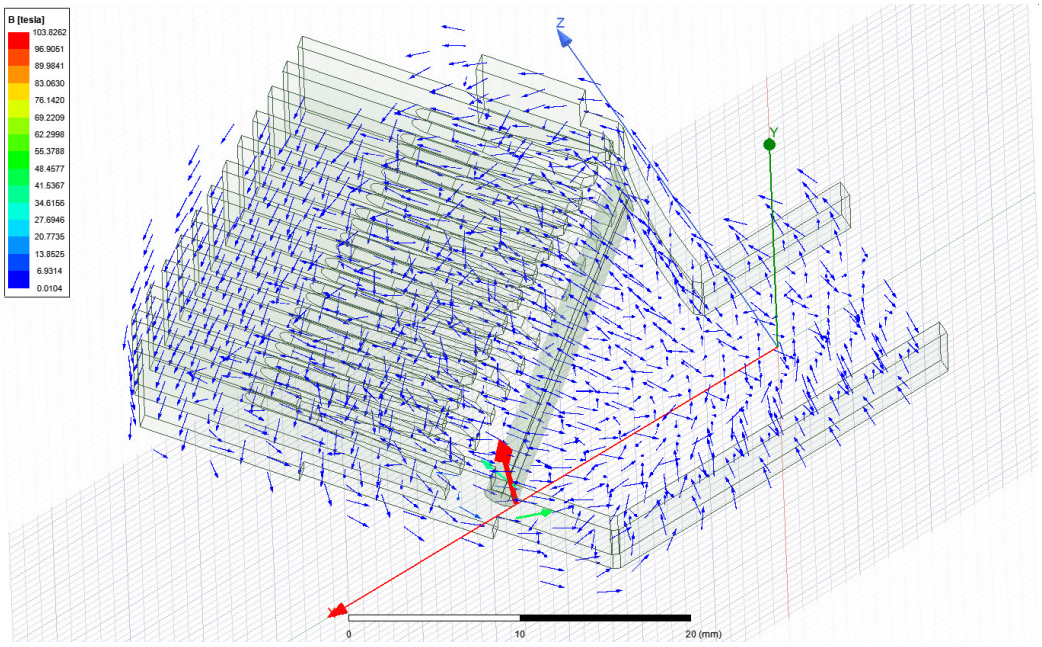

Figure F.2: Magnetic field distribution - Bottom Displaced geometry.

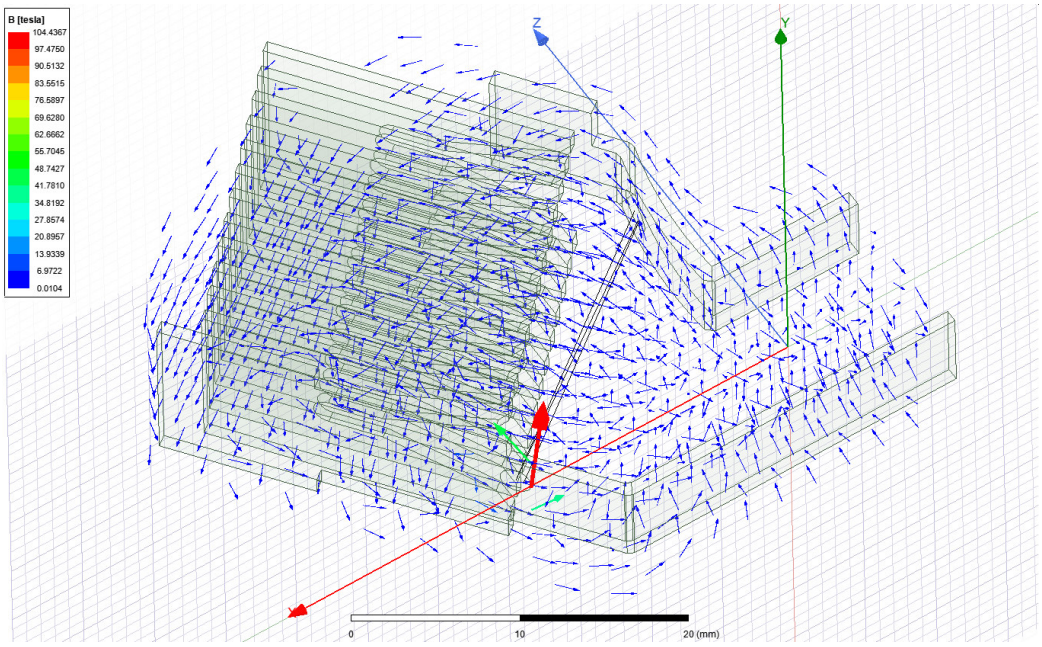

Figure F.3: Magnetic field distribution - Top Displaced geometry.

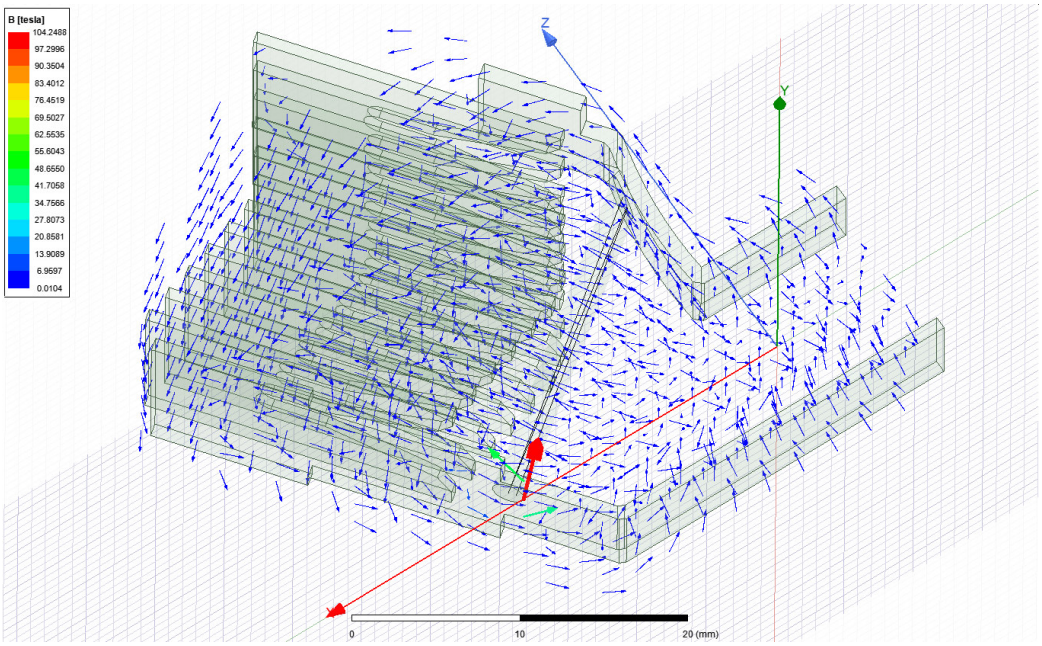

Figure F.4: Magnetic field distribution - Sides Displaced geometry.

Appendix G

Transient Results

G.1 Temperature Distribution

G.1.1 Original geometry

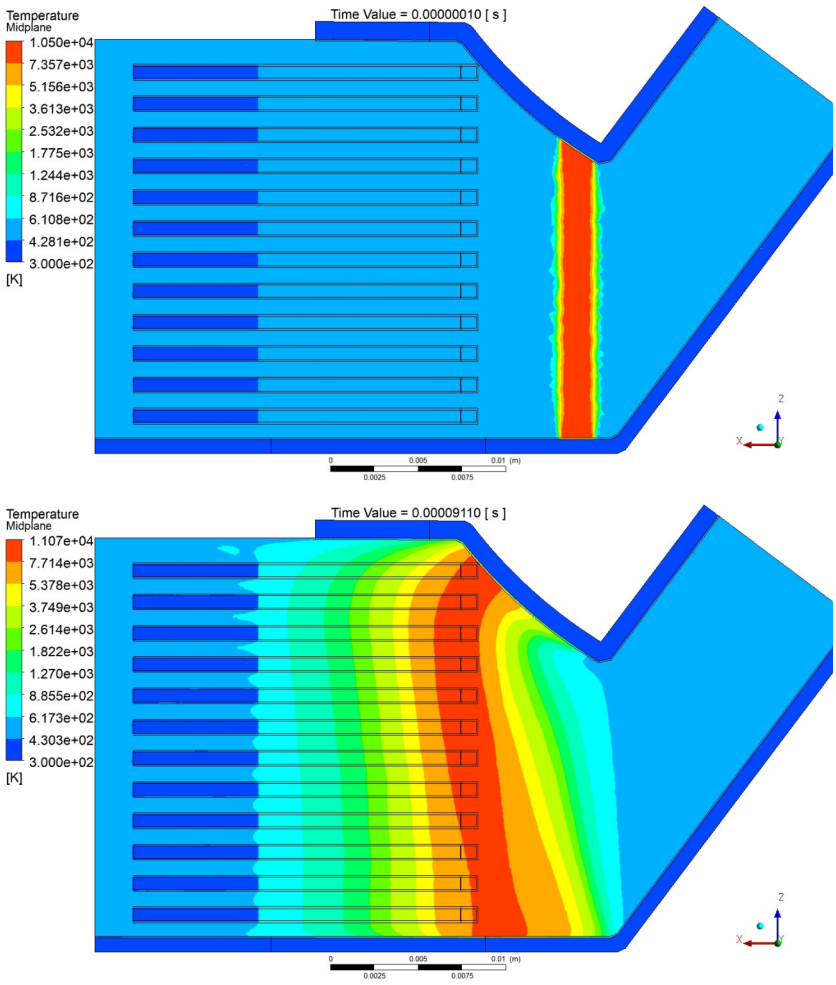

Figure G.1: Temperature distribution - Original geometry ($0.1 - 91.1\ \mu s$).

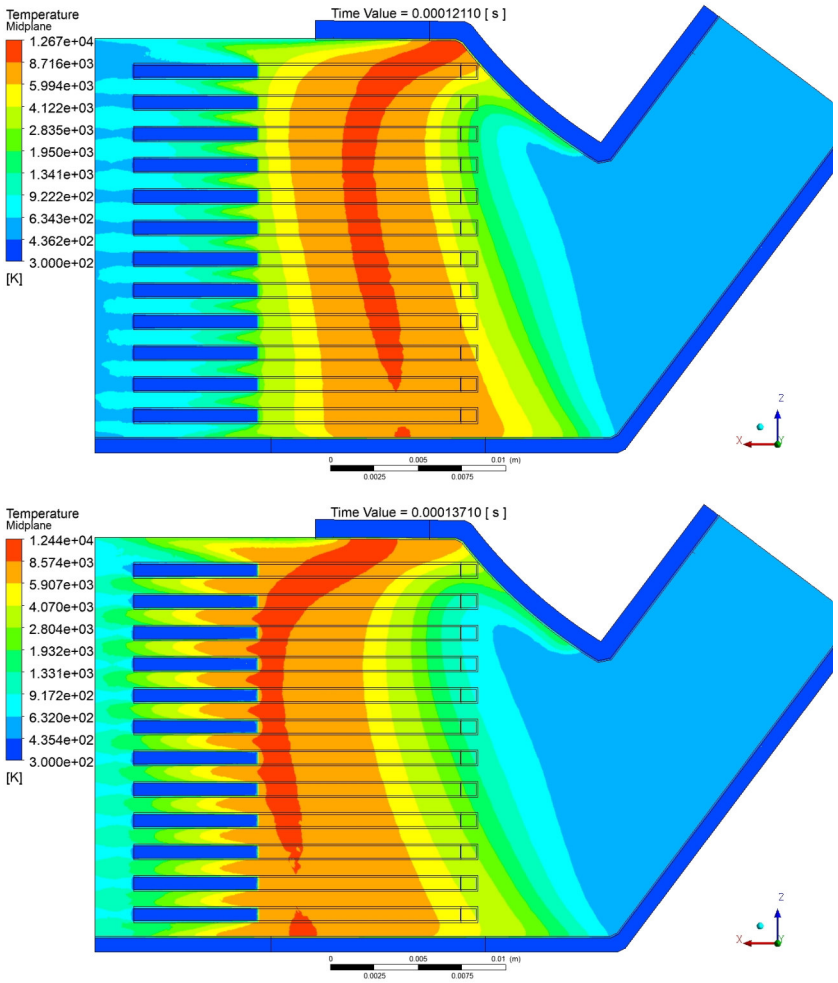

Figure G.2: Temperature distribution - Original geometry ($121.1 - 137.1\ \mu s$).

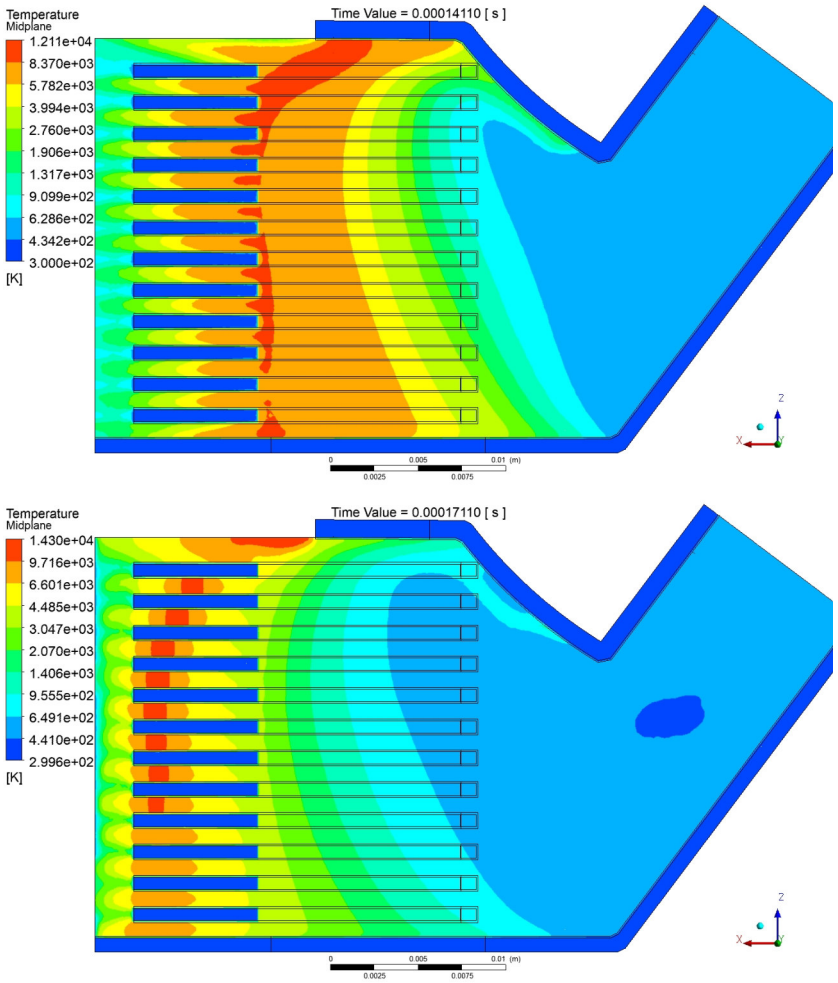

Figure G.3: Temperature distribution - Original geometry ($141.1 - 171.1\ \mu s$).

G.1.2 Bottom Displaced geometry

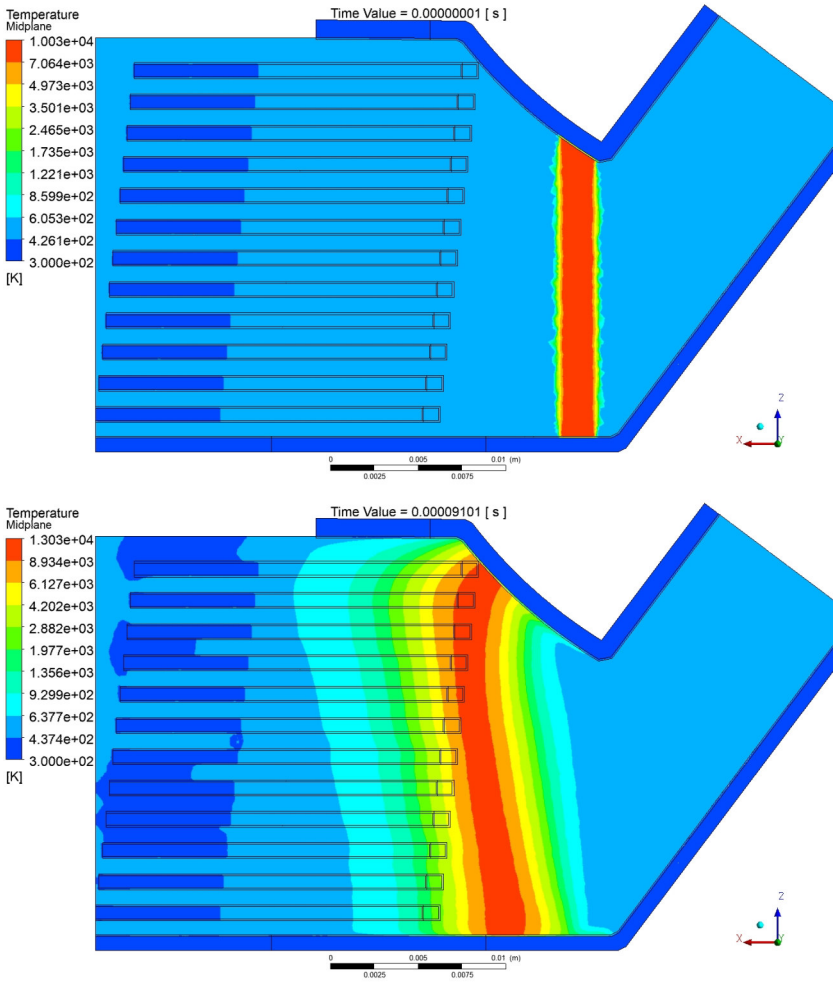

Figure G.4: Temperature distribution - Bottom Displaced geometry (0.01 – 91.01 μs).

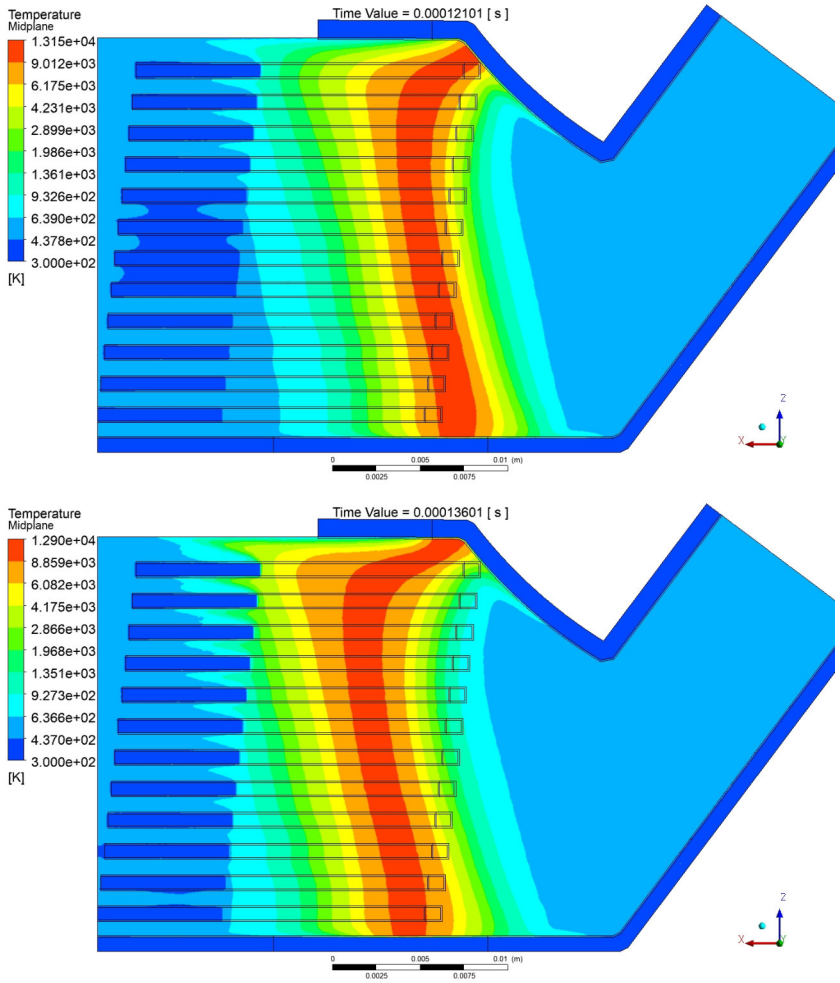

Figure G.5: Temperature distribution - Bottom Displaced geometry (121.01–136.01 μs).

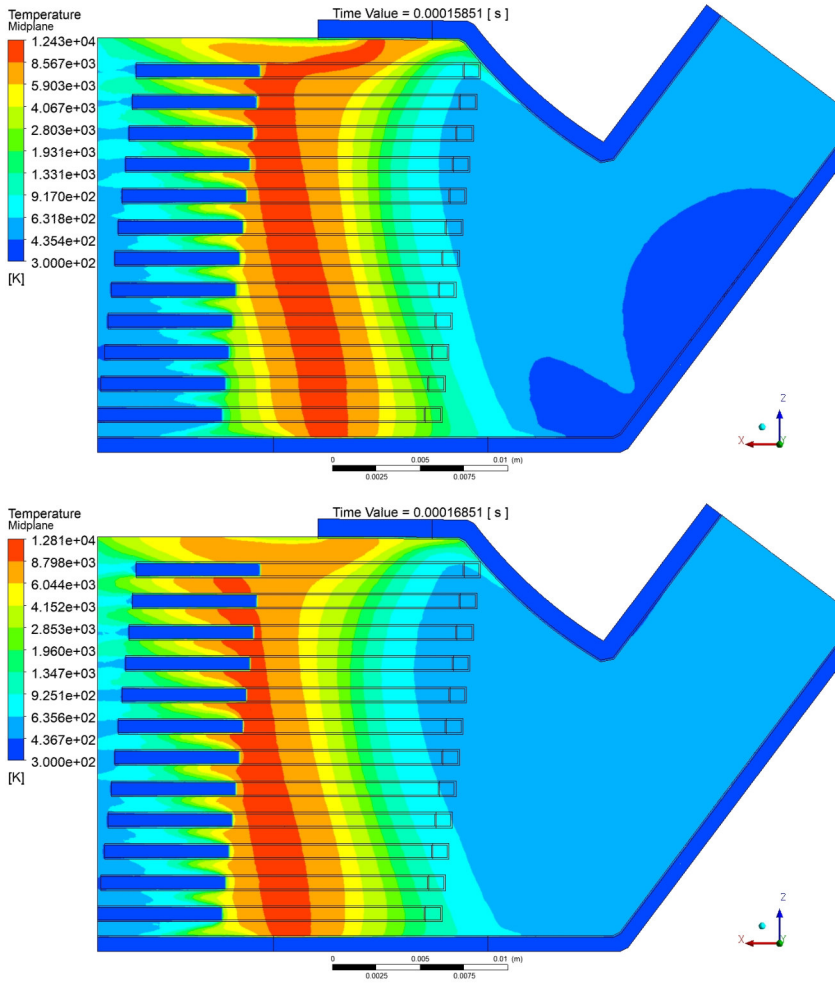

Figure G.6: Temperature distribution - Bottom Displaced geometry (158.51–168.51 μs).

References

[1] Renewables 2021 – Analysis - IEA. (2022). Retrieved 6 October 2022, from https://www.iea.org/reports/renewables-2021.
[2] DNV, G. (2017). Energy transition outlook.
[3] Vidal-Ama ro, J. J., & Sheinbaum-Pardo, C. (2018). A transition strategy from fossil fuels to renewable energy sources in the Mexican electricity system. *Journal of Sustainable Development of Energy, Water and Environment Systems*, *6*(1), 47-66.
[4] Chrobak, U. (2021). Solar power got cheap. so why aren't we using it more?. *Popular Science*, *28*.
[5] Hamilton, J. (2020). Lazard's levelized cost of energy analysis-version 14.0.
[6] Dale, S. (2021). BP statistical review of world energy. *BP Plc, London, United Kingdom*.
[7] COMPITE, GIZ. (2015). *Tarifas Eléctricas – Tutorial para el trabajo en campo* [Ebook] (pp. 16-17). Ciudad de México. Retrieved from https://energypedia.info/images/f/fb/GIZ_Tutorial_Tarifas_Elctricas_2015.pdf.
[8] GreenTouch, Diagrama Interconexión a CFE. (2022). Retrieved 6 October 2022, from http://www.greentouch.com.mx/productos/sistemas-fotovoltaicos/diagrama-interconexin-a-cfe/.
[9] Wall Plug and Voltage Standards Worldwide Countries, plug styles, voltages, frequency 50Hz or 60Hz. (2022). Retrieved 6 October 2022, from https://www.powerstream.com/cv.htm.
[10] Solar Power Plant - Types, Components, Layout and Operation. (2022). Retrieved 6 October 2022, from https://www.electricaltechnology.org/2021/07/solar-power-plant.html.
[11] The world's largest solar power plants. (2022). Retrieved 6 October 2022, from https://www.pv-magazine.com/2021/09/09/the-worlds-largest-solar-power-plants/.

[12] Product Features Low-voltage Circuit Breakers Molded Case Circuit Breakers for DC circuit (up to 1000VDC) MITSUBISHI ELECTRIC FA Factory Automation. (2022). Retrieved 6 October 2022, from `https://www.mitsubishielectric.com/fa/products/lvd/lvcb/pmerit/dcmccb/index.html`.
[13] Anheuser, M., Beckert, T., & Kosse, S. (2011, September). Electric arcs in switchgear–theory numerical simulation and experiments. In *Proc. 19th Symp. Phys. Switching Arc* (pp. 3-15).
[14] J. Wild, J.Y. Battandier, R. Delahaye, T. Devouassoux, M. Perrot, J.L. Ponthenier, 2D arc modelling of a double breaking circuitbreaker. Comparison with measurement and optimisation, in: 15th International Conference on Gas Discharges and their Applications, Toulouse, 2004.
[15] Karetta F, Lindmayer M. Simulation of the gasdynamic and electromagnetic processes in low voltage switching arcs. In Electrical Contacts-1996. Proceedings of the Forty-Second IEEE Holm Conference on Electrical Contacts. Joint with the 18th International Conference on Electrical Contacts 1996 Sep 16 (pp. 35-44). IEEE.
[16] Lisnyak, M. (2018). *Theoretical, numerical and experimental study of DC and AC electric arcs* (Doctoral dissertation, Université Orléans).
[17] Yang F, Rong M, Sun Z, Wu Y, Wang W. A numerical study of arc-splitting processes with eddy-current effects. In2008 17th International Conference on Gas Discharges and Their Applications 2008 Sep 7 (pp. 197-200). IEEE.
[18] Yang, F., Rong, M., Wu, Y., Sun, H., Ma, R., & Niu, C. (2012). Numerical simulation of the eddy current effects on the arc splitting process. *Plasma Science and Technology*, *14*(11), 974.
[19] Singh, A. K., Ahmmed, N., & Atharparvez, M. (2015, October). Numerical simulation of arc splitting process in a LV switching device considering thermo-field emission mechanism. In *2015 IEEE 61st Holm Conference on Electrical Contacts (Holm)* (pp. 391-399). IEEE.
[20] PM, A. P. (2014, November). An inverse problem approach to modeling of circuit breaker arc voltage. In *2014 International Symposium on Fundamentals of Electrical Engineering (ISFEE)* (pp. 1-4). IEEE.
[21] Lozano Ocampo R. *Numerical analysis of heat dissipation in DC low-voltage circuit breakers* (Master's dissertation, University of Guanajuato), Mexico. 2021.
[22] Murty, P. S. R. (2017). *Electrical power systems*. Butterworth-Heinemann.
[23] IEEE Industry Applications Society. Industrial and Commercial Power Systems Committee. (1986). *IEEE Recommended Practice for Protection and Coordination of Industrial and Commercial Power Systems: Approved*

September 19, 1985, Reaffirmed June 27, 1991 IEEE Standards Board: Approved February 28, 1986, Reaffirmed December 9, 1991, American National Standards Institute. IEEE.
[24] Aio, A. I. (2013). *Modelization and analysis of the electric Arc in low voltage circuit breakers* (Doctoral dissertation, Universidad del País Vasco-Euskal Herriko Unibertsitatea).
[25] Nahata, D., Roy, J., & Ochani, D. M. (2015). *U.S. Patent No. 9,087,654*. Washington, DC: U.S. Patent and Trademark Office.
[26] Domejean, E. (2013). *U.S. Patent No. 8,519,292*. Washington, DC: U.S. Patent and Trademark Office.
[27] Fasano, M. A. (2004). *U.S. Patent No. 6,809,282*. Washington, DC: U.S. Patent and Trademark Office.
[28] Nahata, D., Roy, J., & Ochani, D. M. (2015). *U.S. Patent No. 9,087,654*. Washington, DC: U.S. Patent and Trademark Office.
[29] Frind, G., Korte, R., & Zlupko, J. (1973). *U.S. Patent No. 3,735,074*. Washington, DC: U.S. Patent and Trademark Office.
[30] Lindmayer M, Marzahn E, Mutzke A, Ruther T, Springstubbe M. The process of arc splitting between metal plates in low voltage arc chutes. IEEE Transactions on Components and Packaging Technologies. 2006 May 30;29(2):310-7.
[31] Iturregi A, Barbu B, Torres E, Berger F, Zamora I. Electric arc in low-voltage circuit breakers: experiments and simulation. IEEE Transactions on Plasma Science. 2016 Dec 9;45(1):113-20.
[32] Mutzke A, Ruther T, Kurrat M, Lindmayer M, Wilkening ED. Modeling the arc splitting process in low-voltage arc chutes. InElectrical Contacts-2007 Proceedings of the 53rd IEEE Holm Conference on Electrical Contacts 2007 Sep 16 (pp. 175-182). IEEE.
[33] Murphy AB. Transport coefficients of air, argon-air, nitrogen-air, and oxygen-air plasmas. Plasma chemistry and plasma processing. 1995 Jun 1;15(2):279-307.
[34] Yang F, Rong M, Sun Z, Wu Y, Wang W. A numerical study of arc-splitting processes with eddy-current effects. In2008 17th International Conference on Gas Discharges and Their Applications 2008 Sep 7 (pp. 197-200). IEEE.
[35] Breakers, M. C. C., Breakers, I. C. C., Breakers, A. C., & Headquarters, R. O. M. A. C. Right No w!.
[36] Low-Voltage, M. E. (2016). Power Circuit Breaker Switchgear.
[37] Vavra, C. (2022). Basics of low-voltage circuit breakers — Plant Engineering. Retrieved 18 October 2022, from `https://www.plantengineering.com/articles/`

low-voltage-circuit-breaker-basics/#:~:text=The\%20low-voltage\%20power\%20circuit,The\%20LVPCB\%20is\%20older\%20technology.

[38] Li, E., & McEwan, P. M. (1992). Analysis of a circuit breaker solenoid actuator system using the decoupled CAD-FE-integral technique. *IEEE Transactions on magnetics*, *28*(2), 1279-1282.

[39] Liu, H., Wang, Z., & Han, M. (2019, October). Reliability analysis of solenoid valve power supply based on time-varying fault rate. In *2019 4th International Conference on Mechanical, Control and Computer Engineering (ICMCCE)* (pp. 154-1543). IEEE.

[40] Peng, S., Li, J., Duan, W., Cao, Y., & Yu, L. (2022). Effect of Splitter Plates Material and Structure on Arc Characteristics Under the Action of Permanent Magnets. In *The proceedings of the 16th Annual Conference of China Electrotechnical Society* (pp. 475-482). Springer, Singapore.

[41] Lee, K. A., Cho, Y. M., & Lee, H. J. (2020). Circuit model and analysis of molded case circuit breaker interruption phenomenon. *Electronics*, *9*(12), 2047.

[42] Peng, J., & Wang, X. (2022). An Intelligent Control-Based Vacuum Circuit Breaker with Permanent Magnet and Dynamic Characteristic Analysis. *Mobile Information Systems*, *2022*.

[43] Chunlin, G., Chenliang, Z., Tao, L., Kejia, Z., & Huiyuan, M. (2020, July). Operation Delay Prediction of Permanent Magnet Circuit Breaker Based on Neural Network. In *2020 IEEE/IAS Industrial and Commercial Power System Asia (I&CPS Asia)* (pp. 1082-1086). IEEE.

[45] Kroepelin, H., Neumann, K. K., & Hoffmann, K. U. (2013). *Thermodynamic Diagrams for High Temperature Plasmas of Air, Air-Carbon, Carbon-Hydrogen Mixtures, and Argon*. Elsevier.

[46] Billoux, T., Cressault, Y., Teulet, P., & Gleizes, A. (2012, December). Calculation of the net emission coefficient of an air thermal plasma at very high pressure. In *Journal of Physics: Conference Series* (Vol. 406, No. 1, p. 012010). IOP Publishing.

[47] Aubrecht, V., Bartlova, M., & Coufal, O. (2010). Radiative emission from air thermal plasmas with vapour of Cu or W. *Journal of Physics D: Applied Physics*, *43*(43), 434007.

[48] Bogatyreva, N., Bartlova, M., & Aubrecht, V. (2011). Mean absorption coefficients of air plasmas. In *Journal of Physics: Conference Series* (Vol. 275, No. 1, p. 012009). IOP Publishing.

[49] Ghezzi, L., & Balestrero, A. (2010). Modeling and simulation of low voltage arcs.

[50] Maher I.. Boulos, Fauchais, P., & Pfender, E. (1994). *Thermal plasmas: fundamentals and applications*. Plenum Press.
[51] Pacheco Zetino, J. M. (2016). *Multi-physics modeling of cold plasma reformers* (Doctoral dissertation).
[52] Nguyen-Kuok, S. (2017). *Theory of low-temperature plasma physics*. Springer.
[53] Ardakani, E. S. (2016). *Numerical and Experimental Study of the Arc Fluctuations in a DC Plasma Torch* (Doctoral dissertation, University of Toronto (Canada)).
[54] Olmedo, B. G. (1986). Fundamentos de la Teoría del Campo Electromagnético Clásico. *Univ. de Granada*.
[55] Chávez Campos, D. A. (2018). Effect of electromagnetic fields in the process of arc extinction in molded case circuit breakers.
[56] Jeffery, P. A., Sykulski, J. K., & McBride, J. W. (1998). 3D finite element analysis modelling of the arc chamber of a current limiting miniature circuit breaker. *COMPEL-The international journal for computation and mathematics in electrical and electronic engineering*.
[57] Gleizes, A., Cressault, Y., & Teulet, P. (2010). Mixing rules for thermal plasma properties in mixtures of argon, air and metallic vapours. *Plasma Sources Science and Technology*, *19*(5), 055013.
[58] Perkins, G. O., & Emerick, G. J. (1964). *U.S. Patent No. 3,138,687*. Washington, DC: U.S. Patent and Trademark Office.